HIGH ENERGY HADRONIC REACTIONS AT LARGE TRANSVERSE MOMENTA AND THE CERN SPS EXPERIMENT WA7

Lars Bugge

Thesis submitted to the degree cand. real.
at the University of Oslo, Institute of Physics.

1979

PREFACE

This thesis is the result of my work since 1976 as a graduate student in the group for experimental elementary particle physics at the Institute of Physics, University of Oslo. My supervisor has been Dr. Torleiv Buran and the professor of responsibility Dr. Sven O. Sørensen. To both I am most grateful for their help and for the good cooperation we have had.

The work has been carried out partly in Oslo, and partly at CERN, Geneva. I had two stays in Geneva: from May to September 1976, and from October 1977 to August 1978.

I am grateful to CERN, and especially to Drs. Rudolf K. Böck and Arne Lundby, for making these stays possible. At CERN I received help from many people in the Lundby-group. In special I had a close cooperation with Drs. Rudolf K. Böck, Per Helgaker and Jan Myrheim, from whose wide knowledge I have benefited a lot.

The cooperation and companionship with the rest of the staff and the graduate students in the group in Oslo, have been of great value to me.

The thesis is divided into two main parts. The first one presents the necessary theoretical background. The second part describes the CERN SPS experiment WA7. My own work has primarily been connected to the evolution of the track-fitting programme (PROG2; chapter 5) and the Monte Carlo programme (chapter 6). These items are therefore described in more detail than other, equally important, aspects of the experiment. The last chapter presents the first data from the experiment. It should be stressed that these must be regarded preliminary.

Oslo, May 1979,

Lars Bugge.

CONTENTS

PART I THEORETICAL BACKGROUND

Introduction

The first part of this thesis is devoted to a short recapitulation of the relevant historical background in the field of high energy physics which has lead to the experiment WA7 at the CERN SPS. The remainder of the thesis deals with this experiment.

In chapter 1 symmetry properties among the elementary particles are discussed, and the quark model is introduced.

Chapters 2 and 3 are devoted to lepton-hadron and hadron-hadron scattering, respectively. The main purpose is to show how such experiments confirm the quark/parton picture of the elementary particles.

CHAPTER 1 SYMMETRIES AND ELEMENTARY PARTICLES

1.1 Introduction

This chapter is intended to give a short review of the symmetry considerations in elementary particle physics which lead to the quark model.

References [1] and [2] serve as general references throughout the chapter.

1.2 Elementary Particle Physics

One of the most important questions in physics has always been the structure of matter. In modern physics this means the structure of the elementary particles and their interactions.

Elementary particle physics is the experimental and theoretical study of this subject.

Much of the experimental work in this field of high energy physics has been devoted to the search for new elementary particles and to the observation of their masses and internal quantum numbers.

More and more particles have been found as higher and higher energy has become available in particle accelerators.

1.3 Classification of Particles and Interactions

Usually one assumes that there are four kinds of interactions in nature. These are, in order of decreasing strength: the strong, electromagnetic, weak and gravitational interaction.

Each particle has its own mass and other quantum numbers assigned to it, such as charge, hypercharge, spin, isospin, internal parity, lepton number, baryon number, strangeness, charm and others. These quantum numbers uniquely identify the particles.

The particles fall naturally in two main groups, the leptons, which do not feel the strong interaction, and the hadrons, which can interact strongly.

In addition there exist some particles which can not naturally be allocated to any of these groups, such as the photon (carrier of the electromagnetic field), the postulated W-bosons (carriers of the weak field) and the postulated gluons (carriers of the colour field of strong interactions).

Examples of leptons are the electron and muon, each with its own neutrino.

The hadrons are divided into mesons with integer spins and baryons with half-integer spins.

The first discovered meson was the π-meson, whereas the proton, p, and neutron, n, are the most familiar examples of baryons.

In this thesis the emphasis will be put on hadron physics.

1.4 Internal Symmetries

As the number of observed hadrons increased, it became tempting to try to explain the wide variaty of particles and their interactions from more basic principles.

The success of using isospin-symmetry in describing the charge independence of the nuclear forces (the strong interaction) made it probable that such a principle could be found as an internal symmetry principle.

In the same way as charge independence of the nuclear forces can be explained as invariance of the strong interaction Hamiltonian under rotations in isospin space, it was hoped that other symmetry transformations could be found which could give more insight into the behaviour of strongly interacting particles.

Let us now turn to a somewhat more formal description of such transformations.

Let $|\psi\rangle$ be a normalized state vector such that

$$\langle\psi|\psi\rangle = 1 \tag{1.1}$$

Let U be an operator which transforms the state $|\psi\rangle$ to another state $|\psi'\rangle$, i.e.

$$|\psi'\rangle = U|\psi\rangle \tag{1.2}$$

From conservation of probability it follows that if $|\psi'\rangle$ is going to be a physically realizable state, it also has to satisfy eq.(1.1), which gives the condition

$$U^{\dagger}U = 1 \tag{1.3}$$

where $U^{\dagger}$ denotes the Hermitian conjugate of U, and 1 is the unity operator. Operators which satisfy (1.3) are said to be unitary.

According to this, the interest focused on unitary symmetries, and, in analogy with isospin symmetry, especially on unitary symmetries where the symmetry operation can be described as a rotation by a unitary matrix with determinant equal to +1.

It is possible to show that a general unitary matrix with determinant +1 can be represented as

$$U = e^{-i \sum_{\ell=1}^{N} \alpha_\ell S_\ell} \tag{1.4}$$

where $\{\alpha_\ell\}$ is $N = n^2 - 1$ real parameters and $\{S_\ell\}$ is N Hermitian operators satisfying the Lie algebra

$$[S_k , S_\ell] = i \sum_m C_{k\ell m} S_m \tag{1.5}$$

for real structure constants $C_{k\ell m}$.

It can easily be shown that the set of all such U's for a given set

$\{S_\ell\}_{\ell=1}^{N}$, satisfying eq.(1.5), forms a group. The group is called SU(n) and $\{S_\ell\}_{\ell=1}^{N}$ is denoted the generators of the group. Any set of matrices $\{U\}$ where $\{S_\ell\}$ is substituted by matrices satisfying (1.5) is said to be a matrix representation of the group.

We will take as an axiom that if a particle spinor

$$|u\rangle = \begin{pmatrix} u_1 \\ u_2 \\ . \\ . \\ . \\ u_n \end{pmatrix}$$

transforms under U as in (1.4), the corresponding charge conjugated anti-particle spinor

$$|\bar{u}\rangle = \begin{pmatrix} \bar{u}^1 \\ \bar{u}^2 \\ . \\ . \\ . \\ \bar{u}^n \end{pmatrix}$$

transforms under the complex conjugated U^*. The set of all U^* is said to be the contragredient representation of SU(n). By complex conjugation of (1.4) we see that the generators of this representation of SU(n) are the members of the set $\{-S_\ell^*\}_{\ell=1}^{N}$.

We will now state two simple results which will be needed in the following sections.

Firstly the product $|u\rangle|\bar{u}\rangle = \sum_{\ell=1}^{n} u_\ell \bar{u}^\ell$ is invariant under U, that is

$$\sum_{\ell=1}^{n} u'_\ell \bar{u}^{\ell'} = \sum_{\ell=1}^{n} u_\ell \bar{u}^\ell \qquad (1.6)$$

where $u'_\ell = \sum_{k=1}^{n} U_{\ell k} u_k$ and $\bar{u}^{\ell'} = \sum_{k=1}^{n} U^*_{\ell k} \bar{u}^k$. This follows directly from (1.3).

Secondly a tensor with a given symmetry under the exchange of two indeces conserves this symmetry under a linear transformation, i.e.

$$T_{12 \ldots ij \ldots m} = \varepsilon\, T_{12 \ldots ji \ldots m} \Rightarrow T'_{12 \ldots ij \ldots m} = \varepsilon\, T'_{12 \ldots ji \ldots m} \tag{1.7}$$

where $T'_{12 \ldots m} = \sum_{\alpha\beta \ldots \omega} U_{1\alpha}\, U_{2\beta} \cdots U_{m\omega}\, T_{\alpha\beta \ldots \omega}$, and $\varepsilon = \pm 1$.

1.5 SU(2) and the Fermi-Yang Model

If we ignore the weak and electromagnetic interaction, the proton, p, and the neutron, n, can be regarded as two states of the same particle, the nucleon, only differing in the value of the third component of isospin. That is: p and n can freely be interchanged without any change in the nuclear force. This can be formulated as an invariance of the strong interaction Hamiltonian with respect to rotations of the isospin doublet $\begin{pmatrix} p \\ n \end{pmatrix}$ by an operator as in (1.4) with $n = 2$, i.e. an SU(2) transformation. If $\begin{pmatrix} p \\ n \end{pmatrix}$ transforms under U, the antinucleon doublet $\begin{pmatrix} \bar{p} \\ \bar{n} \end{pmatrix}$ transforms under U^*, as stated in the previous paragraph. Now it is possible to show that U and U^* are equivalent in SU(2), i.e. there exists an operator A such that

$$A\, U^*\, A^{-1} = U \tag{1.8}$$

It turns out that for the representation of SU(2) which has generators $\{\frac{1}{2}\sigma_k\}_{k=1}^{3}$ with $\{\sigma_k\}$ being the Pauli spin-matrices, A is given by

$$A = e^{-i\pi\frac{1}{2}\sigma_2} = \begin{pmatrix} 0 & 1 \\ -1 & 0 \end{pmatrix} \tag{1.9}$$

By operating on the equation

$$\begin{pmatrix} \bar{p} \\ \bar{n} \end{pmatrix}' = U^* \begin{pmatrix} \bar{p} \\ \bar{n} \end{pmatrix} \tag{1.10}$$

with A and use the fact that $A^{-1} A = 1$, we obtain

$$\begin{pmatrix} \bar{n} \\ -\bar{p} \end{pmatrix}' = U \begin{pmatrix} \bar{n} \\ -\bar{p} \end{pmatrix}$$

That is, the doublet $\begin{pmatrix} \bar{n} \\ -\bar{p} \end{pmatrix}$ transforms as $\begin{pmatrix} p \\ n \end{pmatrix}$. Then we can couple these doublets by using Clebsch Gordan theory, making the direct product

$$\begin{pmatrix} p \\ n \end{pmatrix} \otimes \begin{pmatrix} \bar{n} \\ -\bar{p} \end{pmatrix} = \begin{pmatrix} p\bar{n} \\ \frac{1}{\sqrt{2}}(n\bar{n} - p\bar{p}) \\ -n\bar{p} \\ -\frac{1}{\sqrt{2}}(p\bar{p} + n\bar{n}) \end{pmatrix} \tag{1.11}$$

According to Clebsch Gordan theory for coupling of SU(2) -multiplets, the three upper states represent an invariant triplet, whereas $-\frac{1}{\sqrt{2}}(p\bar{p} + n\bar{n})$ is a singlet. This follows also from eq.(1.6).

Identifying now the triplet $\begin{pmatrix} p\bar{n} \\ \frac{1}{\sqrt{2}}(n\bar{n} - p\bar{p}) \\ -n\bar{p} \end{pmatrix}$ with the π-meson triplet $|\pi> = \begin{pmatrix} -\pi^+ \\ \pi^0 \\ \pi^- \end{pmatrix}$ and the singlet with the η-meson, we have arrived at the Fermi-Yang model for mesons. This is obviously not a satisfactory model since it does not account for mesons with strangeness or charm, and since it does not give any obvious scheme for baryons apart from the nucleon doublet.

To recapitulate, we have made the direct product of two two-dimensional objects and broken the four-dimensional result into two invariant subspaces of dimensions 3 and 1, respectively. These invariant subspaces are then associated with particle multiplets.

Symbolically one writes

$$\{2\} \otimes \{2\} = \{1\} \oplus \{3\} \tag{1.12}$$

1.6 SU(3) and the Sakata Model

The natural extension of the Fermi-Yang model is to add a particle with strangeness to the proton and neutron and say that all particles can be constructed from a fundamental triplet. This was done by Sakata. He assumed that

$$\begin{pmatrix} p \\ n \\ \Lambda \end{pmatrix}$$

is a fundamental triplet which transforms under SU(3). It is usual to plot the fundamental particle multiplets in a hypercharge versus I_z diagram, as in fig. 1.1(a) and (b).

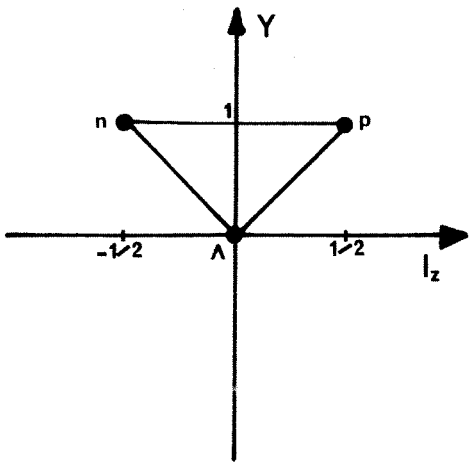

Fig. 1.1(a)
The fundamental Sakata triplet.

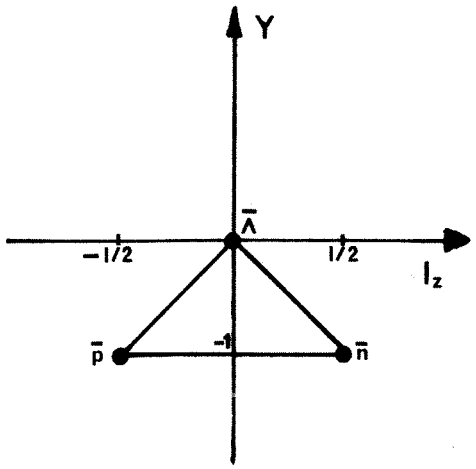

Fig. 1.1(b)
The fundamental Sakata antitriplet.

The Sakata model gives a good classification of the mesons. Once again higher representations of SU(3) can be achieved by taking direct products of the basic triplet with its antitriplet, and meson multiplets will again be

associated with invariant subspaces under SU(3) transformations. This will be demonstrated in the next paragraph.

The Sakata model failed, however, to give a correct description of the baryon spectrum.

1.7 SU(3) and the Quark Model

In 1964 Gell-Mann [3] and Zweig [4] seemed to find a way out. They proposed that the basic SU(3) triplets consist of the quarks u, d and s (or p, n and λ) and the antiquarks $\bar{u}$, $\bar{d}$ and $\bar{s}$ (or $\bar{p}$, $\bar{n}$ and $\bar{\lambda}$).

These quarks should be spin 1/2 particles and otherwise have the quantum numbers listed in table 1.1.

Remarkable are the non-integer charges and baryon numbers (and accordingly hypercharges, since $Y = B + S$).*

The u and d form an iso-doublet whereas s is a singlet.

Table 1.1 Quantum Numbers of Quarks and Antiquarks

	B	I	I_z	Y	S	Q
u	$\frac{1}{3}$	$\frac{1}{2}$	$\frac{1}{2}$	$\frac{1}{3}$	0	$\frac{2}{3}$
d	$\frac{1}{3}$	$\frac{1}{2}$	$-\frac{1}{2}$	$\frac{1}{3}$	0	$-\frac{1}{3}$
s	$\frac{1}{3}$	0	0	$-\frac{2}{3}$	- 1	$-\frac{1}{3}$
$\bar{u}$	$-\frac{1}{3}$	$\frac{1}{2}$	$-\frac{1}{2}$	$-\frac{1}{3}$	0	$-\frac{2}{3}$
$\bar{d}$	$-\frac{1}{3}$	$\frac{1}{2}$	$\frac{1}{2}$	$-\frac{1}{3}$	0	$\frac{1}{3}$
$\bar{s}$	$-\frac{1}{3}$	0	0	$\frac{2}{3}$	1	$\frac{1}{3}$

---

* It should be noted that schemes with integer quark charges also exist. See for example [7].

The quark and antiquark fundamental triplets are plotted in $Y-I_z$ diagrams in fig. 1.2.

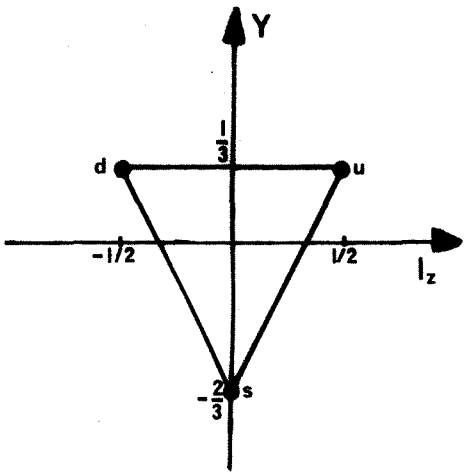

Fig. 1.2(a)
The quark triplet.

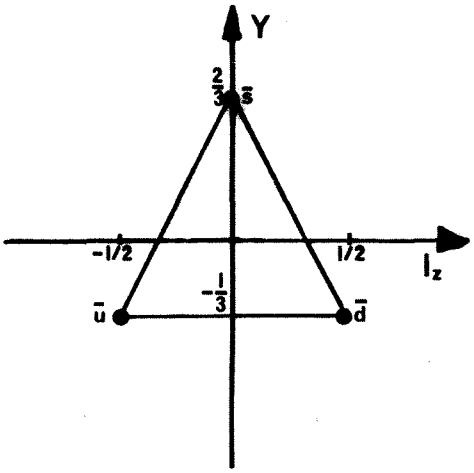

Fig. 1.2(b)
The antiquark triplet.

Gell-Mann and Zweig assumed that the only allowed combinations of quarks and antiquarks to form particles were: either one quark and one antiquark (mesons) or three quarks (baryons) or three antiquarks (antibaryons).

With this scheme it turned out to be possible to build up with correct quantum numbers all particles which were then known, and to get a natural grouping in multiplets of particles with the same spin and parity, and roughly the same mass. Some examples of this will be given below.

1.7.1 The $J^P = 0^-$ Meson Octet

As mentioned above, mesons are in the quark model regarded as composite systems of one quark and one antiquark. The simplest way to construct such states, is to take the direct product between the fundamental quark and anti-

quark triplets:

$$\begin{pmatrix} u \\ d \\ s \end{pmatrix} \otimes \begin{pmatrix} \bar{u} \\ \bar{d} \\ \bar{s} \end{pmatrix} = \begin{pmatrix} u\bar{u} & u\bar{d} & u\bar{s} \\ d\bar{u} & d\bar{d} & d\bar{s} \\ s\bar{u} & s\bar{d} & s\bar{s} \end{pmatrix} \tag{1.13}$$

The lowest-lying octet o^- is obtained by coupling the quarks with relative angular momentum $\ell = o$ and total spin $s = o$.

In analogy with the Fermi-Yang model, we identify $u\bar{d}$ with the π^+ and $d\bar{u}$ with the π^-. Moreover, one can verify that $s\bar{u}$ and $s\bar{d}$ can be identified with the K^- and $\bar{K}^o$, respectively.

The diagonal terms in (1.13), $u\bar{u}$, $d\bar{d}$ and $s\bar{s}$, do not directly correspond to particles, but out of these terms it is possible to construct three other independent linear combinations. We know from the Fermi-Yang case that $\frac{1}{\sqrt{2}}(u\bar{u} - d\bar{d})$ can be identified with the π^o. We also know from eq.(1.6) that the trace $\frac{1}{\sqrt{3}}(u\bar{u} + d\bar{d} + s\bar{s})$ is invariant and thus forms an SU(3) singlet, which we will call $|\eta_1\rangle$. Thus we see that the nine product states have been broken up into one singlet and one octet, or in analogy with (1.12):

$$\{3\} \otimes \{\bar{3}\} = \{1\} \oplus \{8\} \tag{1.14}$$

The last member of the octet is uniquely determined by the following: it is a normalized linear combination of the diagonal elements in (1.13), orthogonal to $|\pi^o\rangle$ and $|\eta_1\rangle$. We call it $|\eta_8\rangle$ and find:

$$|\eta_8\rangle = \sqrt{\frac{1}{6}}(u\bar{u} + d\bar{d} - 2s\bar{s}) \tag{1.15}$$

The o^- meson octet is drawn in a $Y\text{-}I_z$ diagram i fig. 1.3.

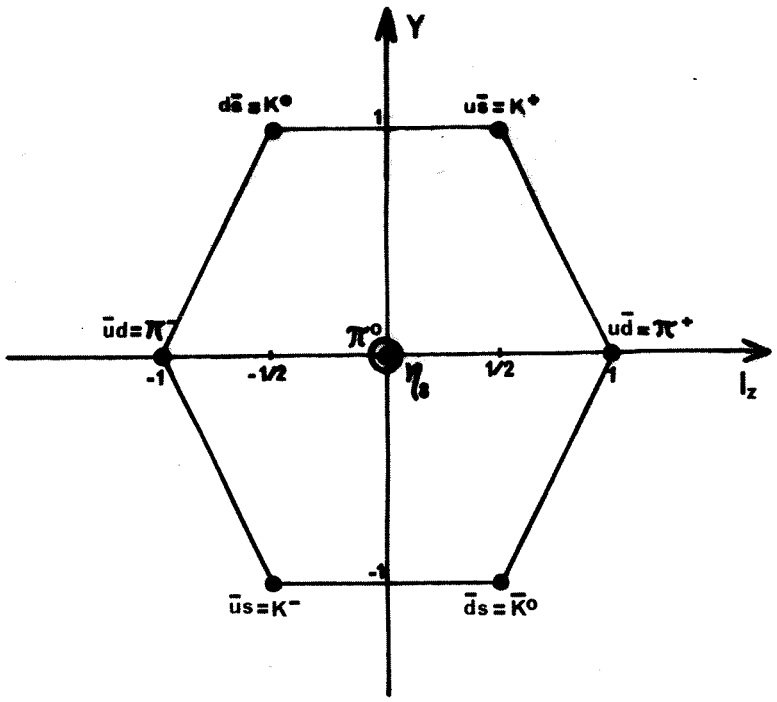

Fig. 1.3
The $J^P = 0^-$ Meson Octet.

1.7.2 Baryon Octet and Decuplet

As stated earlier, baryons are built up from three quarks and antibaryons from three antiquarks. Let us denote our basic triplet

$$t = \begin{pmatrix} q_1 \\ q_2 \\ q_3 \end{pmatrix} = \begin{pmatrix} u \\ d \\ s \end{pmatrix} \tag{1.16}$$

and a state built up as some linear combination of triplet products involving the quarks q_i, q_j, q_k as T_{ijk}.

Now it follows from (1.7) that the subset of all $\{T_{ijk}\}$ with a given symmetry under the exchange of two indeces forms an invariant subspace under SU(3). Such invariant subspaces may again be associated with particle multiplets. By observing that choosing 3 indeces out of n possible ones in an

exchange-symmetric way corresponds to placing 3 identical spheres in n identical boxes, it is easily shown that this can be done in

$$\frac{(n+2)(n+1)n}{3!}$$

different ways. In our case, with n equal to 3, we accordingly have 10 fully symmetric combinations of the three quark indeces.

The 10 lowest-lying such states are found to be the <u>decuplet</u> of $J^P = \frac{3^+}{2}$. By observing the isospin of the 10 different quark combinations we see that the decuplet falls into one $I = 3/2$ isoquartet (the Δ of 1236 MeV), one $I = 1$ isotriplet (the Σ^* of 1385 MeV), one $I = 1/2$ isodoublet (the Ξ^* of 1530 MeV) and one isosinglet (the Ω^- of 1672 MeV).

We have now seen that the 27 states in the product $t \otimes t \otimes t$ fall into $\{10\} \oplus \{17\}$. It is possible to show that the $\{17\}$ can be divided into one singlet, the fully antisymmetric combination

$$T_{123}^{\text{antisym}} = \sum_{i,j,k=1}^{3} \varepsilon_{ijk}\, q_i\, q_j\, q_k \quad ,$$

and two octets with mixed symmetry properties, i.e.

$$\{3\} \otimes \{3\} \otimes \{3\} = \{1\} \oplus \{8\} \oplus \{8\} \oplus \{10\} \qquad (1.17)$$

The observed $J^P = \frac{1^+}{2}$ baryon octet is actually found to be a linear combination of the two octets in (1.17). It consists of the p, n doublet of 938 MeV, the Σ triplet of 1190 MeV, the Ξ doublet of 1320 MeV and the Λ of 1116 MeV. By coupling the quarks with different values of the relative angular momentum, multiplets with different J^P can be constructed, and in this way all known hadrons which consist of the quarks u, d, s (see the next paragraph) can be correctly constructed and classified.
The $\frac{1^+}{2}$ baryon octet and the $\frac{3^+}{2}$ baryon decuplet are shown in figs. 1.4 and 1.5, respectively. Note that when for example the quark structure of

Δ^+ is given as uud, what is really meant is the fully symmetric combination

$$T^{sym}_{112} = \frac{1}{\sqrt{3}} (q_1\, q_1\, q_2 + q_1\, q_2\, q_1 + q_2\, q_1\, q_1) = \frac{1}{\sqrt{3}} (uud + udu + duu).$$

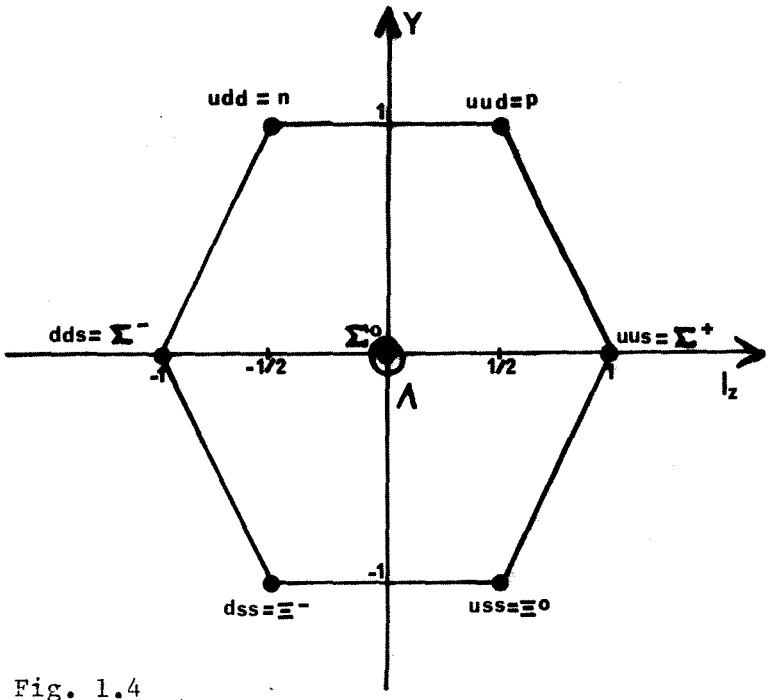

Fig. 1.4
The $J^P = \frac{1}{2}^+$ baryon octet. Only quark content is indicated

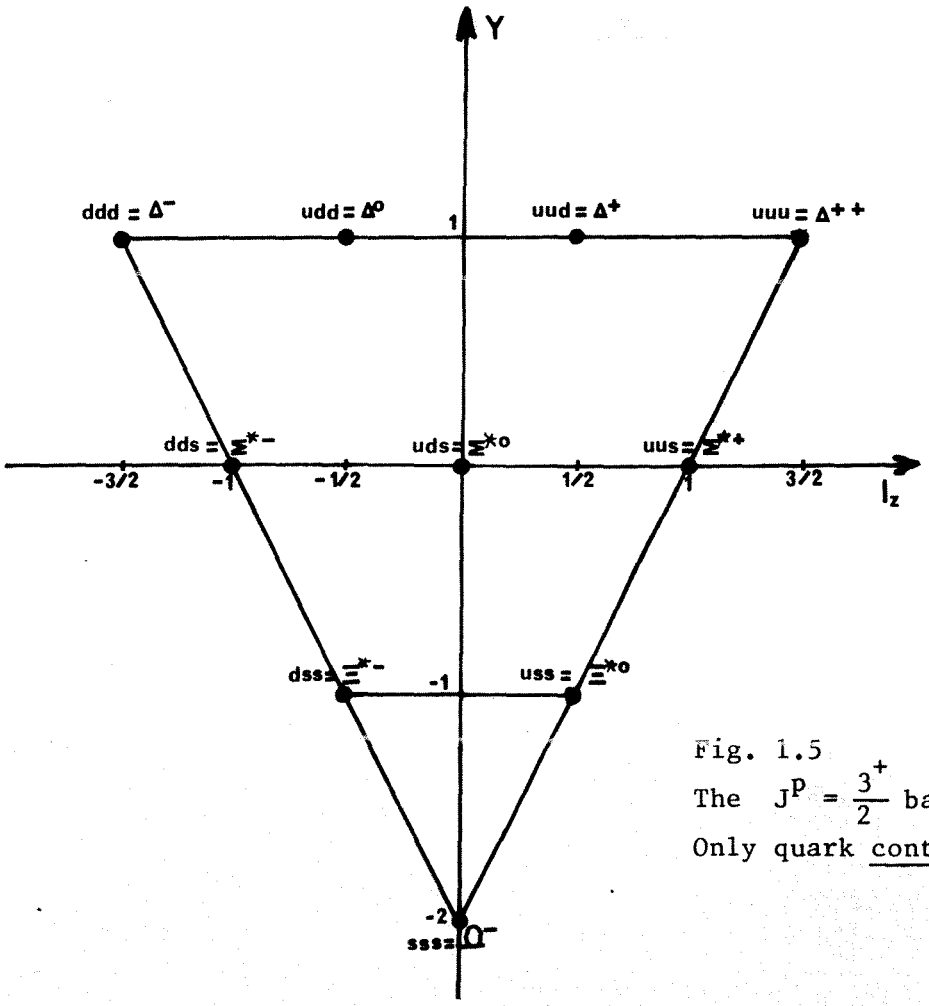

Fig. 1.5
The $J^P = \frac{3}{2}^+$ baryon decuplet.
Only quark content is indicated.

1.8 New Quarks - SU(4) and SU(5)

The observation of the J/ψ family of particles has made it necessary to introduce still another quark, the c-quark which carries one unit of the quantum number charm [5]. This gives us a fundamental quartet instead of a triplet, and the symmetry-operations in question are transformations under SU(4) instead of SU(3).

After the observation of the upsilon particle Υ, still a new quark seems to be introduced, the bottom-quark b [6]. Then the appropriate symmetry group is SU(5). Particle multiplets can also in these cases be constructed following the same lines as in the SU(3) case, and these multiplets will contain the SU(3) multiplets as subsets.

CHAPTER 2 HADRON CONSTITUENTS - THE ELECTROMAGNETIC AND WEAK INTERACTION

2.1 Introduction

In this chapter we will briefly consider which evidence one has from lepton-nucleon scattering experiments that nucleons are built up from more basic constituents. We will also look at the arguments for these constituents being identical to the quarks described in the previous chapter.

We give a short review of deep inelastic electron-nucleon scattering which leads to the parton model, and very briefly mention charged current neutrino-nucleon scattering.

The notation and some definitions of kinematical variables are given in Appendix I.

2.2 Elastic Electron-Proton Scattering and Electromagnetic Form Factors

Let us consider the scattering of an electron against a nucleon as in fig. 2.1. The nucleon is at rest in the laboratory system and has mass M.

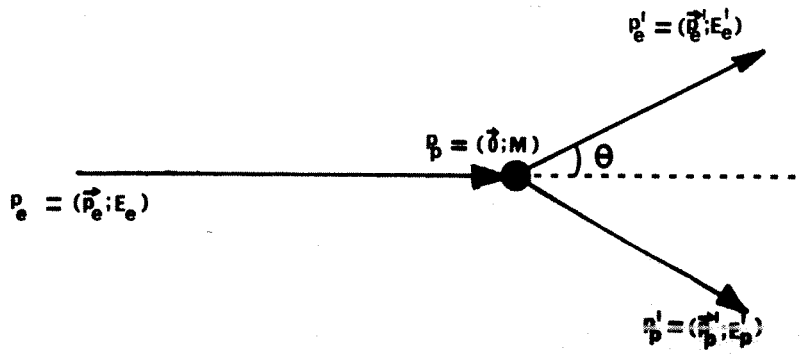

Fig. 2.1
Electron-proton scattering in the lab.-system.

We define the four-momentum transfer as

$$q = (\vec{q},\nu) = (p_e - p_e') = ((\vec{p}_e - \vec{p}_e'),\ (E_e - E_e')) \qquad (2.1)$$

We observe that the squared four-momentum transfer equals the negative of the familiar Mandelstam variable t,

$$q^2 = -t = (p_e - p_e')^2 \qquad (2.2)$$

If we now consider the scattering process of fig. 2.1 with the electron relativistic such that its mass can be neglected, and the recoiling proton non-relativistic, first order Born approximation gives when all spins are neglected [8]:

$$\frac{d\sigma}{d\Omega} = \left(\frac{d\sigma}{d\Omega}\right)_{\text{Rutherford}} \cdot [F(q^2)]^2 \qquad (2.3)$$

where $\left(\frac{d\sigma}{d\Omega}\right)_{\text{Rutherford}}$ is the well known

$$\left(\frac{d\sigma}{d\Omega}\right)_{\text{Rutherford}} = \frac{e^4}{4\vec{p}_e^{\,2}\sin^4\frac{\theta}{2}}$$

$F(q^2)$ is the proton form factor, defined as the 3-dimensional Fourier transform of the proton's spatial charge distribution.

The next step is to consider high energy elastic scattering where the proton can no longer be taken to recoil nonrelativistically. We also include the electron's spin by applying Dirac theory. When the proton is considered spinless and pointlike, we arrive at [8] the Mott cross section:

$$\left(\frac{d\sigma}{d\Omega}\right)_{\text{Mott}} = \frac{e^4 \cos^2\frac{\theta}{2}}{4\vec{p}_e^{\,2}\sin^4\frac{\theta}{2}\left\{1 + \frac{2|\vec{p}_e|}{M}\sin^2\frac{\theta}{2}\right\}} \qquad (2.4)$$

Now comes the problem of introducing the proton's spin and structure. The spin presents no fundamental difficulty and can be accounted for in the Dirac theory of spin 1/2-particles. This gives an additional term to

the Mott cross section taking care of the magnetic scattering which is introduced by the proton magnetic moment.

However, the proton structure gives rise to a more serious problem. Not only has the proton a charge distribution in space, but it also has an anomalous magnetic moment - that is, the value of the proton magnetic moment differs from that predicted by ordinary Dirac theory.

It can be argued [9] that this necessarily leads to a description where two independent form factors enter, the electric, $G_E(q^2)$, and the magnetic, $G_M(q^2)$, which are functions of the squared four-momentum transfer.

It can be shown that the cross section for elastic scattering of relativistic spin 1/2 electrons against spin 1/2 protons in terms of the electric and magnetic form factors are given by the following formula, known as the Rosenbluth cross section [8]:

$$\left(\frac{d\sigma}{d\Omega}\right)_{\text{Rosenbluth}} = \left(\frac{d\sigma}{d\Omega}\right)_{\text{Mott}} \left[\frac{G_E^2(q^2) + \frac{q^2}{4M^2} G_M^2(q^2)}{1 + \frac{q^2}{4M^2}} + \frac{q^2}{4M^2} 2G_M^2(q^2) \operatorname{tg}^2\frac{\theta}{2}\right] \tag{2.5a}$$

This can shortly be written:

$$\left(\frac{d\sigma}{d\Omega}\right)_{\text{Rosenbluth}} = \left(\frac{d\sigma}{d\Omega}\right)_{\text{Mott}} \left[A(q^2) + B(q^2) \operatorname{tg}^2 \frac{\theta}{2}\right] \tag{2.5b}$$

2.3 Inclusive Electron-Nucleon Scattering

Let us now turn to inclusive electron scattering,

$$e\ p \rightarrow e + \text{anything}$$

where only the electron in the final state is observed, and see how the formulae (2.5) can be generalized to this generally inelastic case.

We will assume that the reaction takes place as an exchange of one single photon. This is a common assumption, and ref. [10] argues that corrections

from higher order photon exchange processes can be expected to be less than a few percent. Then the Feynman diagram for the process is as in fig. 2.2.

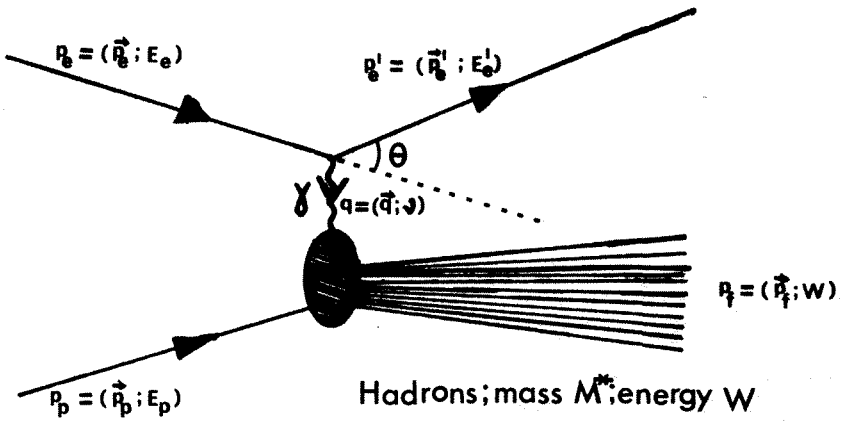

Fig. 2.2
Inelastic ep interaction by single virtual photon exchange.

The four-momentum transfer q is carried by the photon. A real photon has $q^2 = 0$, and as this is generally not the case for a scattering process, the exchanged photon is virtual (off mass-shell).

q^2 can easily be computed in the lab. system where the proton is at rest before the scattering:

$$q^2 = (p_p - p_f)^2 = M^2 - M^{*2} + 2M\nu \qquad (2.6)$$

where M is the proton mass, M* is the mass of the final state hadrons and ν is transferred energy.

Except for the constraint represented by eq.(2.6), q^2 and ν are independent kinematical variables in the process of fig. 2.2 since the mass of the final state hadrons, M^*, is not fixed. This is in contrast to the situation in elastic scattering where

$$q^2_{elastic} = 2M\nu \tag{2.7}$$

Hence the inclusive scattering process is described by a double differential cross-section $\frac{d^2\sigma}{dq^2 d\nu}$. Analogous to the Rosenbluth formula of eqs.(2.5) this double differential cross-section is described in terms of two structure functions $W_1(q^2,\nu)$ and $W_2(q^2,\nu)$ [8, 10]:

$$\frac{d^2\sigma}{dq^2 d\nu} = \frac{E'_e}{E_e} \frac{4\pi\alpha^2}{q^4} \left[W_2(q^2,\nu) \cos^2 \frac{\theta}{2} + 2W_1(q^2,\nu) \sin^2 \frac{\theta}{2} \right] \tag{2.8}$$

where the energies and angles refer to the lab.system. The structure functions $W_1(q^2,\nu)$ and $W_2(q^2,\nu)$ are generalisations to inelastic scattering of the elastic form factors $G_E(q^2)$ and $G_M(q^2)$ described in section 2.2.

Since the exchanged photon is virtual, it can be longitudinally polarized (helicity zero) as well as transversely (helicity ±1). It can be shown [11] that the structure functions W_1 and W_2 are closely related to the total cross-sections for (virtual) γ nucleon → hadrons. In fact, if σ_T, σ_L denotes these cross sections for transverse, longitudinal photons, we have:

$$\begin{aligned} W_1(q^2,\nu) &\propto \sigma_T(q^2,\nu) \\ W_2(q^2,\nu) &\propto (\sigma_T(q^2,\nu) + \sigma_L(q^2,\nu)) \end{aligned} \tag{2.9}$$

Fig. 2.3 shows some curves for fixed θ in the $q^2 - \nu$ plane. From eq.(2.8) we see that W_1 and W_2 can be separated if $\frac{d^2\sigma}{dq^2 d\nu}$ is measured along two (or more) lines for fixed θ. In the cross-point between two such lines q^2 and ν are the same, and the cross sections for the two different values of θ in this point give the wanted separation. From

(2.9) it is evident that a separation between W_1 and W_2 at the same time is a separation between σ_T and σ_L. We shall see later on that knowledge of σ_T and σ_L gives information on the spin of the hadron constituents.

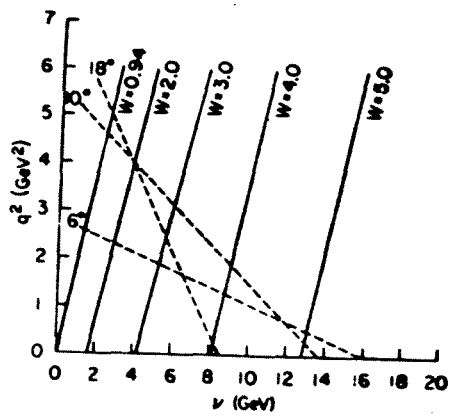

Fig. 2.3
Lines of fixed θ in the q^2-ν plane. (W in this figure denotes the final state hadron mass, i.e. what we call M^*), (from [11]).

An important experimental observation from such measurements is that the dependence of W_1 and W_2 on q^2 and ν which in principle could be quite complicated, seems to be strikingly simple. It turns namely out that the structure functions for large q^2 and ν to a very good approximation can be regarded as functions of only one variable, ω, defined by

$$\omega = \frac{2M\nu}{q^2} \tag{2.10}$$

That is, for q^2 and ν large:

$$\begin{aligned} MW_1(q^2,\nu) &= F_1(\omega) \\ \nu W_2(q^2,\nu) &= F_2(\omega) \end{aligned} \tag{2.11}$$

This phenomenon, called Bjorken scaling, is illustrated in figs. 2.4 and 2.5.

In fig. 2.4 νW_2 is plotted at different values of q^2 with $M^* > 2$ GeV and such that ω is constantly equal to 4. It is a clear demonstration of the fact that νW_2 for fixed ω is independent of q^2.

Fig. 2.5 a and b show $2MW_1$ and νW_2, respectively, as functions of ω. The points with nearly same ω have different values of q^2, and the fact that they fall on a single curve is again a clear demonstration of Bjorken scaling. The constant behaviour of νW_2 for $\omega \gtrsim 4$ is another simplicity of high energy electron-proton scattering, but has nothing to do with Bjorken scaling. W in the figures is the hadronic mass which we have called M^*.

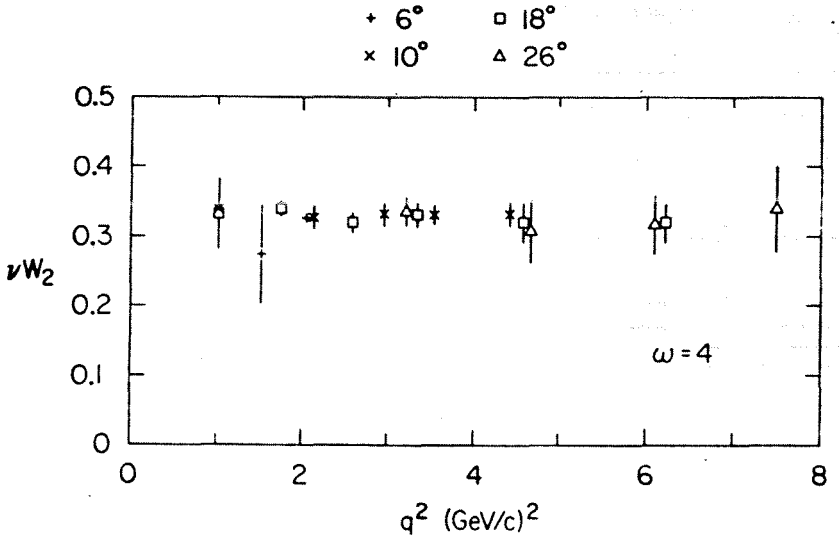

Fig. 2.4
νW_2 as a function of q^2 for constant ω, with $M^* > 2$ GeV (from [12]).

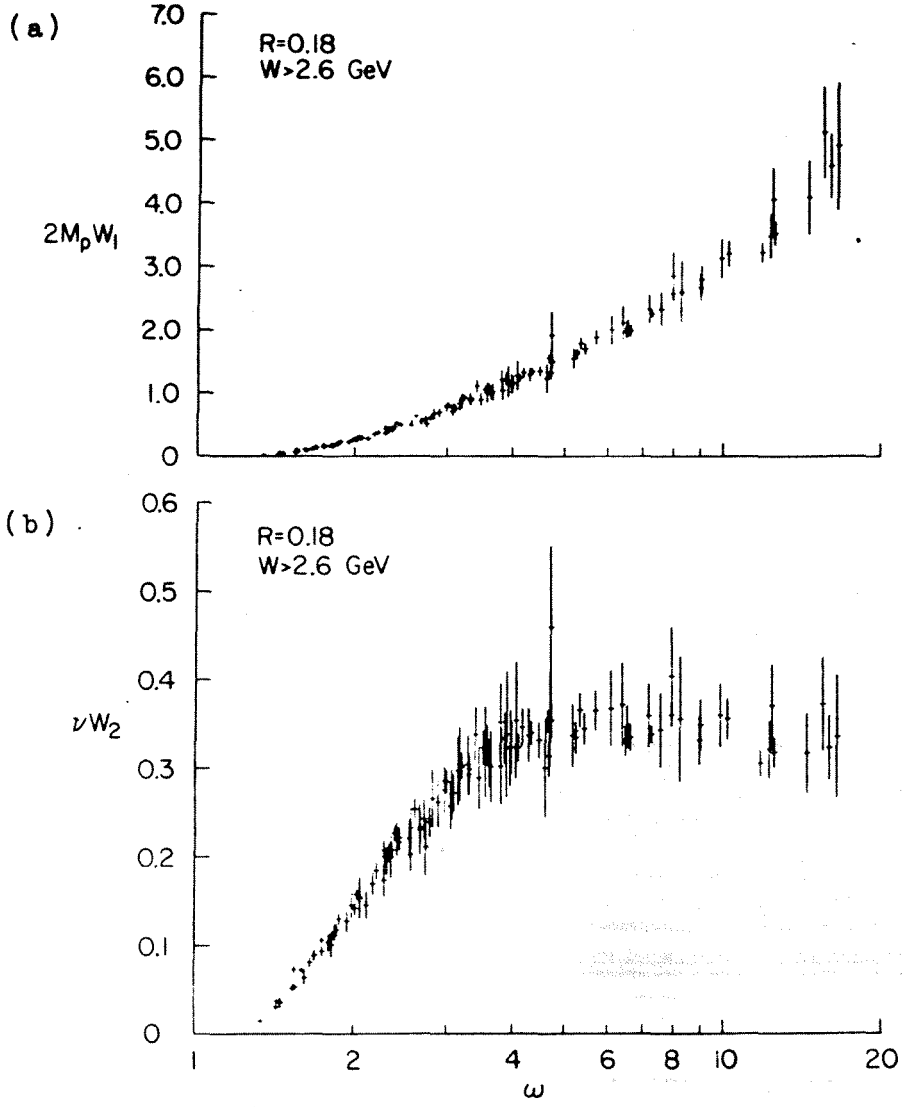

Fig. 2.5

$2\,MW_1$ and νW_2 as functions of ω. Nearly overlapping values of ω correspond to different values of q^2. See the text (from [13]).

The phenomenon of Bjorken scaling can be understood if one assumes that the nucleons consist of a number of pointlike constituents. This will be explained in the following section.

2.4 The Parton Model

In the parton model the nucleon is assumed to consist of a number N of pointlike, i.e. structureless, constituents called partons. One further assumes that these partons can be treated as free particles when q^2 and ν become large. In this limit the dominating process in electron-nucleon scattering is assumed to be a single electron-parton interaction mediated by a single virtual photon. Since the partons are pointlike, this interaction has to be purely elastic. But then we have from eq.(2.7) that

$$q^2 = 2m\nu ,$$

m being the effective parton mass. Thus we immediately see that the picture of pointlike constituents leads to an intimate relation between q^2 and ν.

The number N of partons is not fixed, but may vary according to a probability distribution P_N normalized such that

$$\sum_{N=1}^{\infty} P_N = 1 \qquad (2.12)$$

In the very high momentum frame where parton transverse momentum can be neglected, each parton n carries a fraction x_n of the total nucleon three-momentum $\vec{P}$:

$$\vec{p}_n = x_n \vec{P} \qquad (2.13)$$

In this frame it is also approximately true that the energy of the parton is the same fraction of the nucleon energy, so we may write

$$p_n \approx x_n P \qquad (2.14)$$

In a configuration with N partons, the momentum fractions x_n vary according to the simultanious probability distribution

$$f^N(x_1, x_2, \ldots , x_N)$$

such that

$$\int dx_1\, dx_2 \ldots dx_N\, f^N(x_1, x_2, \ldots, x_N)\, \delta\Big(\sum_{n=1}^{N} x_n - 1\Big) = 1 \qquad (2.15)$$

where the δ-function just conserves momentum.

The probability that one parton (the first, say) shall have momentum fraction x_1 is simply found by integrating over all other partons :

$$f_1^N(x_1) = \int dx_2 \ldots dx_N\, f^N(x_1, x_2, \ldots, x_N)\, \delta\Big(\sum_{n=1}^{N} x_n - 1\Big) \qquad (2.16)$$

It follows that

$$\int_0^1 f_n^N(x_n)\, dx_n = 1 \qquad (2.17)$$

Let us now consider an elastic electron-parton collision. If the parton has four-momentum xP before the collision, it has four-momentum $(xP + q)$ afterwards. P is again the nucleon four-momentum. Since the parton mass doesn't change, we have

$$(xP)^2 = (xP + q)^2$$

which gives

$$x = \frac{q^2}{2M\nu} = \frac{1}{\omega} \qquad (2.18)$$

Thus we see how the parton momentum fraction x is related to the Bjorken scaling variable ω.

We will now see what experiments can tell us about the spin of the partons.

From measurements of σ_T and σ_L (eq. (2.9)) it can be argued that the partons are not mostly spin zero particles. Measurements [13] clearly indicate a fairly low value of the ratio

$$R = \frac{\sigma_L}{\sigma_T} \qquad (2.19)$$

Ref. [13] uses an overall value of R of

$$R \simeq 0.18 \qquad (2.20)$$

in their calculations. This means that transverse photon exchange is dominating. Going to the Breit-frame where photon and parton directions are colinear, it is easy to see that a spinless parton can not absorb a transverse (helicity ±1) photon. Therefore R should approach infinity for spin zero partons. According to (2.20) we can then conclude that the partons are not spinless objects [14]. Further arguments can be given, which favour spin 1/2 partons [12].

By adding up contributions to the structure functions from elastic electron-parton collisions, we get for spin 1/2 partons [16,17] :

$$F_2(x) = xF_1(x) = \sum_{N=1}^{\infty} P_N \sum_{n=1}^{N} f_n^N(x) Q_n^2 \qquad (2.21)$$

with x as in (2.18) and Q_n being the charge of the n'th parton (in units of e). Thus a theoretical basis for the observed Bjorken scaling is established.

2.5 The Quark Parton Model

We have seen that the observed behaviour of the inclusive electron-nucleon scattering cross-section can be accounted for in a model where the nucleon is assumed to consist of a number of pointlike consituents. As we have reason to believe that these partons have spin 1/2, it is tempting to identify them with the quarks introduced in chapter 1. This is what is done in the quark parton model. We will now introduce a new set of distribution functions $D_j(x)$ and rewrite eq.(2.21) in a more convenient form, following ref. [16]. We define

$$D_j(x) = \sum_N P_N N_j f_j^N(x) \qquad (2.22)$$

where N_j is the number of constituent quarks of type j ; $j = u, \bar{u}, d, \bar{d}, s, \bar{s}, c, \bar{c}, \ldots$, in a configuration with N quarks in total.

From the normalization condition (2.17) it follows that

$$\int_0^1 D_j(x)dx = \sum_{N=1}^{\infty} P_N N_j = < N_j > \qquad (2.23)$$

That is: the integral over x of $D_j(x)$ is the mean number of quarks of type j.

We can easily express (2.21) in terms of the D's :

$$F_2(x) = xF_1(x) = \sum_j D_j(x) Q_j^2 \qquad (2.24)$$

Let us now consider only the u,d and s quarks and their antiquarks. We write

$$D_u(x) \equiv u(x)$$
$$D_{\bar{u}}(x) \equiv \bar{u}(x)$$
$$\vdots$$

and so on. By explicitly inserting the quark charges from table 1.1 we can write (2.24) as

$$F_2^{\gamma p}(x) = xF_1^{\gamma p}(x) = \frac{4}{9}(u^p(x) + \bar{u}^p(x)) + \frac{1}{9}(d^p(x) + \bar{d}^p(x)) + \frac{1}{9}(s^p(x) + \bar{s}^p(x)) \qquad (2.25)$$

The γ indicates that the structure functions in question are the electromagnetic ones, and the p stands as usual for proton. Thus $u^p(x)$ for example, is the u-quark distribution function in the proton.

In the quark model described in chapter 1, the proton consists of three quarks and no antiquarks. The three quarks are uud, so the proton should not contain any s-quarks. A fully, relativistic description of the proton, however, contains a sea of quark-antiquark pairs. Therefore we must include distribution functions also for the s-quark and the antiquarks. But we would expect that the contribution to the structurefunctions from these is small. By separately measuring cross sections for electron-proton and electron-deutron scattering, one can extract information on the neutron electromagnetic structurefunctions. For these we can write similarly to eq.(2.25) :

$$F_2^{\gamma n}(x) = xF_1^{\gamma n}(x) = \frac{4}{9}(u^n(x) + \bar{u}^n(x)) + \frac{1}{9}(d^n(x) + \bar{d}^n(x)) + \frac{1}{9}(s^n(x) + \bar{s}^n(x)) \tag{2.26}$$

The neutron is obtained by rotating the proton an angle π in iso-spin space. Setting $u^p(x) = u(x)$ and so on, we therefore have

$$\begin{aligned} u^n(x) &= d^p(x) = d(x) \\ d^n(x) &= u^p(x) = u(x) \\ s^n(x) &= s^p(x) = s(x) \end{aligned} \tag{2.27}$$

and similarly for the antiquark distributions. Then we can write eqs.(2.25) and (2.26) as

$$\begin{aligned} F_2^{\gamma p}(x) = xF_1^{\gamma p}(x) &= \frac{4}{9}(u(x) + \bar{u}(x)) + \frac{1}{9}(d(x) + \bar{d}(x)) + \frac{1}{9}(s(x) + \bar{s}(x)) \\ F_2^{\gamma n}(x) = xF_1^{\gamma n}(x) &= \frac{4}{9}(d(x) + \bar{d}(x)) + \frac{1}{9}(u(x) + \bar{u}(x)) + \frac{1}{9}(s(x) + \bar{s}(x)) \end{aligned} \tag{2.28}$$

Also the weak neutrino-nucleon interactions can be described by structure functions in a similar manner as in electron-nucleon interactions.
It turns out that the distinction between right and left-handed currents in the theories of the weak interaction makes it necessary to use <u>three</u> weak structure functions as opposed to two in the electromagnetic case [10].

It also turns out that the parton model predicts Bjorken scaling in these weak structure functions. The weak structure functions can be expressed in terms of the quark distributions analogously to eqs. (2.28). Armed with these expressions it is possible to make predictions on connections between measurable electromagnetic and weak structure functions. One such prediction is the famous

$$\left[\frac{F_2^{\gamma n} + F_2^{\gamma p}}{F_2^{\nu n} + F_2^{\nu p}} \right](x) = \frac{\frac{5}{9}(u + \bar{u} + d + \bar{d}) + \frac{2}{9}(s + \bar{s})}{2(u + \bar{u} + d + \bar{d})} \geq \frac{5}{18} \tag{2.29}$$

In this expression the s-quark contribution to the weak structure functions is neglected because it is expected to be only of order 1/20 of the u,d contribution.

The number $\frac{5}{18}$ is just the mean squared valence quark charge of proton + neutron, altogether three u and three d quarks :

$$\frac{5}{18} = \frac{1}{6}\left(3 \cdot \left(\frac{2}{3}\right)^2 + 3 \cdot \left(\frac{1}{3}\right)^2\right) \qquad (2.30)$$

In fig. 2.6 the neutrino-nucleon weak structure function $F_2^{\nu N}$ (averaged over proton and neutron) is compared to $\frac{18}{5}$ (=3.6) times the electromagnetic $F_2^{\gamma N}$. We see that for large values of x the ratio of (2.29) is very near 5/18. This means that there is little contribution to the electron-nucleon scattering from s and $\bar{s}$ at large x as expected from a naive quark parton model. The x' in the figure is the alternative Bloom-Gilman variable which has the same asymptotical properties as the Bjorken variable [18].

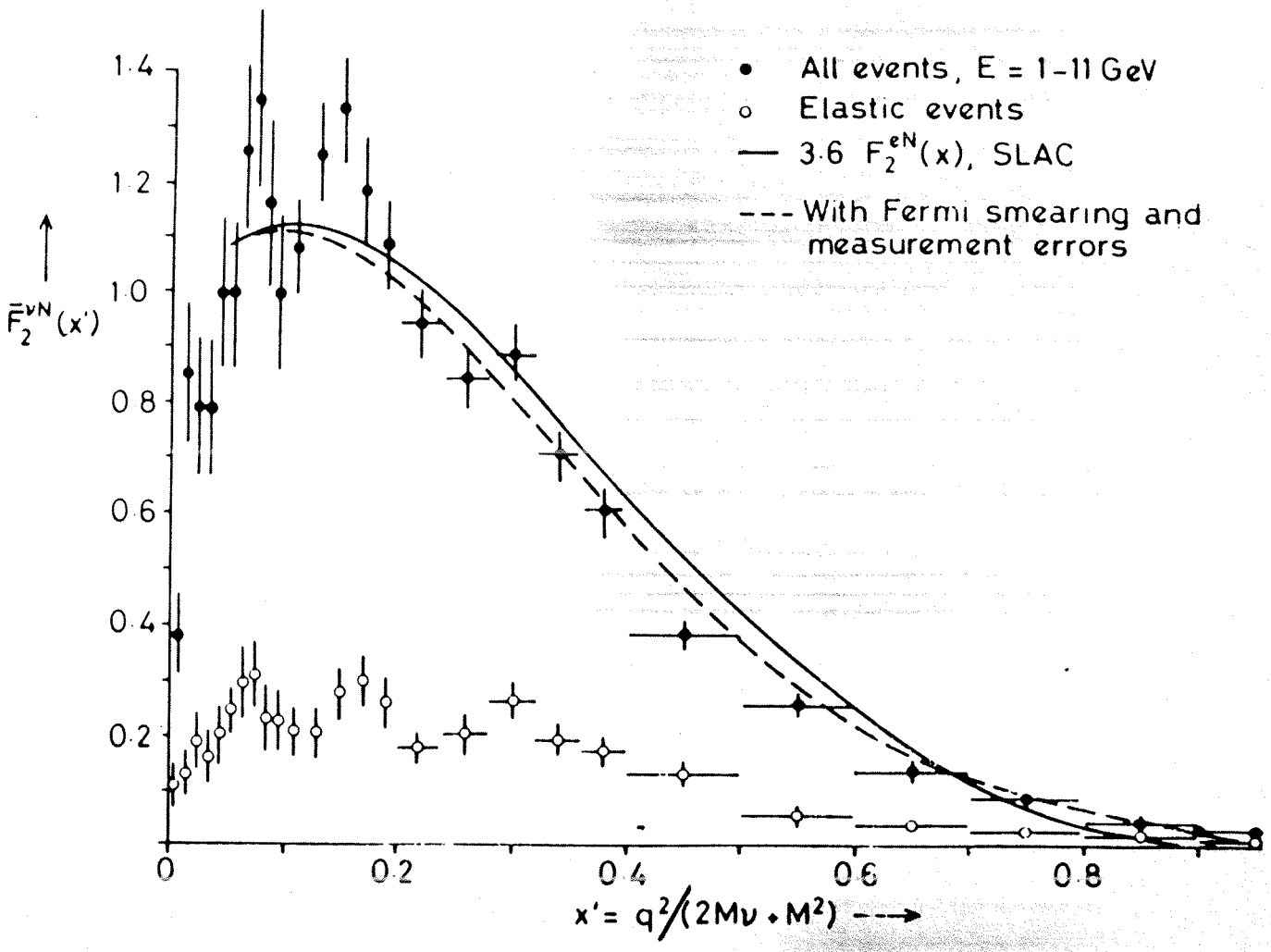

Fig. 2.6
$F_2^{\nu N}$ compared to $\frac{18}{5} \times F_2^{\gamma N}$ (solid line). See the text (from [19]).

Because of (2.30) this result is a good indication that the main contribution to the scattering is from quarks with squared charges $\frac{4}{9}$ and $\frac{1}{9}$. In fact it can be argued that [19] the experimental result of fig. 2.6 unambiguously leads to the result that the partons have fractional charges.

The quark parton model also predicts a number of other sum rules, which all seem to be consistent with experiment [15,18].

CHAPTER 3 HADRON CONSTITUENTS - THE STRONG INTERACTION

3.1 Introduction

In the previous chapter we saw how scattering of leptons on nucleons could give information on the internal structure of the nucleons. The leptons are structureless particles without strong interaction and thus the experimental results can in a relatively simple way be interpreted in terms of nucleon internal structure.

When one turns to collisions between hadrons, the situation becomes more complicated. Now both the interacting particles are composite systems with strong interaction. In order to have a complete picture of the hadrons, however, such experiments have to be performed even though their interpretation is difficult.

In the same way as electrons and neutrinos probe the nucleon structure by means of the electromagnetic and weak interaction, respectively, hadron-hadron reactions can be said to constitute a way of studying the hadronic structure by means of the strong interaction.

We will first describe inclusive reactions with emphasis on inclusive production of a single hadron. Some different theoretical approaches based upon the quark/parton picture will be mentioned.

Then we turn to exclusive reactions, paying most attention to the case of elastic scattering.

In all the cases we will concentrate on scattering with large momentum transfer. This is because such events are generally believed to be the result of some sort of hard collision where the colliding particles have penetrated deeply into each other, thus (hopefully) revealing the properties of the hadronic constituents. One hopes that the results from hadron-hadron scattering shall be consistent with what has been learned from deep inelastic lepton-nucleon scattering.

3.2 Inclusive Large p_T Hadron-Hadron Scattering

In inclusive scattering experiments one detects only a subset of the produced particles, neglecting all the others. Often is only one particle in the final state identified, i.e. the reaction is

$$A + B \longrightarrow C + X \tag{3.1}$$

where A,B,C are identified hadrons and X can be anything. A typical example is

$$p + p \longrightarrow \pi^o + X \tag{3.2}$$

An advantage with inclusive processes from an experimental point of view, is that the cross sections are generally much larger than for exclusive reactions (for example elastic scattering).

Since $\frac{d^3p}{E}$ is a relativistic invariant quantity, it is usual to describe the process of eq. (3.1) in terms of the differential cross section $E\frac{d\sigma}{d^3p}$ where E and $\vec{p}$ are the energy and three-momentum of hadron C. This Lorentz invariant cross section is generally a function of three variables [20], often taken as the momentum component of C perpendicular to the beam, p_T, the ratio x_T of p_T to the maximum possible, $x_T = \frac{p_T}{p_T^{max}} = \frac{p_T}{p_{CM}^{max}} \approx \frac{2p_T}{\sqrt{s}}$, and the CM scattering angle θ_{CM}.

See fig. 3.1. Also other choices of the three variables are possible [21].

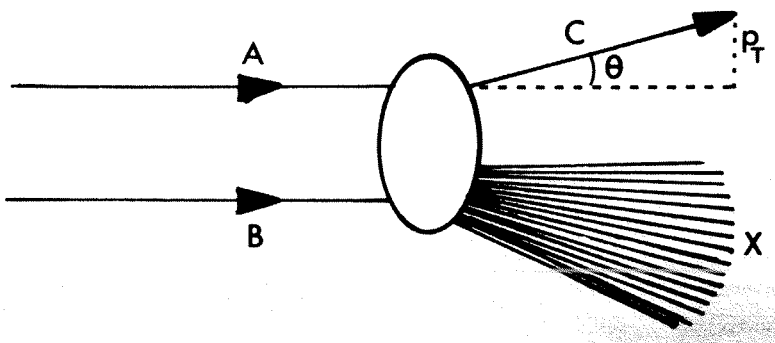

Fig. 3.1 Inclusive reaction, A + B → C + X .

For p_T below 2 GeV/c it turned out [22] that the cross section

$$E \frac{d\sigma}{d^3p} (pp \to \pi X)$$

could be well fitted with an exponential p_T -behaviour and that it was roughly energy independent. In the whole range 23 GeV $< \sqrt{s} <$ 53 GeV ref.[22] fitted both π^+ and π^- production as

$$E \frac{d\sigma}{d^3p} = a\, e^{-b\, p_T} \qquad (3.3)$$

with a value of b close to 6.

However, it turned out that at larger values of p_T the cross section started to decrease less drastically. This is illustrated in fig. 3.2. We see that at p_T around 4 GeV/c the yield is already 3 orders of magnitude larger than expected from an extrapolation of low p_T data. A natural explanation of this fact is that the low and high p_T reactions are dominated by different mechanisms.

As mentioned earlier it is now generally accepted that the high energy,

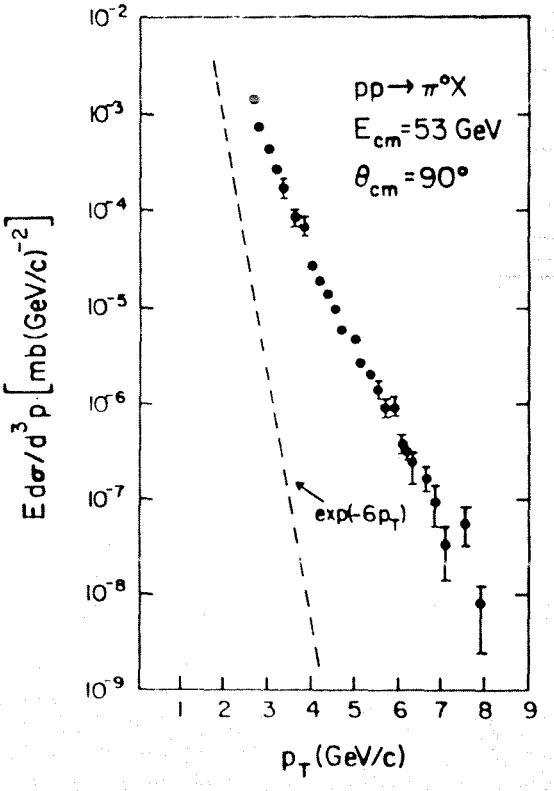

Fig. 3.2
Large p_T inclusive π^o-production (from [20]).

large p_T events are results of some kind of hard collision between constituents of the colliding hadrons, although other explanations are also possible [21].

3.2.1 Hard Scattering and Power Law Scaling

Common to most of the hard scattering models is that they lead to complicated calculations. We will only state the characteristics of the models and the most important results, without going into any calculational details. The models make use of quark distribution functions as in the electron-nucleon case. In addition some functions are needed which describe the probabilities that certain quarks fragment into certain hadrons. These are called quark fragmentation functions.

If the quark distribution and fragmentation functions are dependent on momentum fractions only, and not otherwise on energy, they are said to scale, or to be scale invariant.

Under the general assumptions of scale invariant distribution functions and dimensionless coupling constants, it can be shown [23,24] that over a large x_T -range

$$E \frac{d\sigma}{d^3p} \quad (AB \to CX)_{90^o} = \frac{1}{(p_T^2)^N} f(x_T) \tag{3.4}$$

In [24] it is argued that the above expression is valid for $x_T > 0.15$. This form of the invariant cross section is called power law scaling. N is given by

$$N = n_i + n_f - 2 \tag{3.5}$$

where n_i (n_f) is the number of elementary fields in the initial (final) state of the subprocess which actively participates in the reaction.

Thus N is model dependent. Fig. 3.3(a) and (b) show two possible subprocesses. In (a) the underlying subprocess is quark-quark scattering by gluon exchange giving $n_i = n_f = 2$ or $N = 2$. In (b) the basic process is quark interchange giving rise to quark-meson vertices. In this $qM \to qM$ process $n_i = n_f = 3$ which gives $N = 4$.

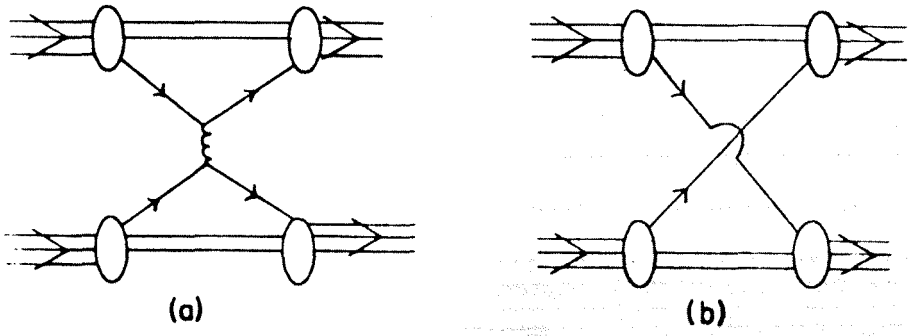

Fig. 3.3 (a) $qq \to qq$ subprocess by gluon exchange.
(b) $qM \to qM$ subprocess by quark interchange (from [20]).

Some different subprocesses with corresponding p_T -behaviour are summarized in table 3.1. q stands for quark, g for gluon, M for meson and B for baryon.

Table 3.1 Basic subprocesses in hadron reactions. See the text.

Subprocess	n_i	n_f	p_T behaviour
$qq \to qq$ $qg \to qg$ $gg \to gg$	2	2	p_T^{-4}
$qg \to Mq$	2	3	p_T^{-6}
$qM \to qM$	3	3	p_T^{-8}
$q\bar{q} \to M\bar{M}$	2	4	
$qB \to qB$	4	4	p_T^{-12}
$q(2q) \to MB$	3	5	

For energies in the range 30 GeV < $\sqrt{s}$ < 63 GeV experiments [25] show that the inclusive π^0-production in pp collisions is not p_T^{-4}-dominated. It is found [25] that in the range 3.5 GeV/c < p_T < 7 GeV/c the p_T - dependence is close to p_T^{-8}, whereas for 7.5 GeV/c < p_T < 14.0 GeV/c the value of the exponent becomes close to 5.

Let us now very briefly mention some approaches which have been made to explain the observed behaviour of the cross sections.

3.2.2 The Constituent Interchange Model (CIM)

The constituent interchange model [21,24,26,27] was developed by Blankenbecler, Brodsky and Gunion. They assume perfect scaling distribution functions and no complications to coupling constants from asymptotic freedom mechanisms. They then sum up contributions from subprocesses as in table 3.1 (subprocess expansion).

If subprocesses of the p_T^{-4} type exist, it is only a question of normalization at which p_T these processes start to dominate the cross section [24]. In $pp \to \pi X$ they find that at p_T below ~ 10 GeV/c $qM \to qM$ is the dominating subprocess, giving p_T^{-8}-behaviour in agreement with data [24,27]. They claim that the reason that this "second order" process dominates the primary $qq \to qq$ process in this p_T-domain, is because the latter process involves a fragmentation of a quark into the observed π, whereas in the former process the π is produced promptly. This fragmentation is said [24] to lead to a numerical suppression of the cross section by a factor 100 - 1000.

It is argued [24] that the p_T^{-8} quark fusion process $q\bar{q} \to M\bar{M}$ is small compared to the $qM \to qM$ process, also for meson-baryon scattering.

Further on they find that the p_T^{-6} subprocesses are made insignificant by

a cancellation which is a result of gauge invariance [24].

According to this view, the cross section for process (3.2) can be expressed to first order as a sum of p_T^{-8} and p_T^{-4} terms. In [27] this is given as

$$E\frac{d\sigma}{d^3p}(pp \to \pi X) \propto \left[\left(\frac{10}{p_T}\right)^8 + \left(\frac{\alpha_s}{0.15}\right)^2\left(\frac{10}{p_T}\right)^4\right] \qquad (3.6)$$

α_s is the strong coupling constant. With a commonly used value of $\alpha_s \approx 0.2$, we see that the contribution from the basic QCD twobody processes with p_T^{-4} behaviour equals the CIM $qM \to qM$ p_T^{-8} subprocesses contribution at $p_T \approx 9$ GeV/c.

The possibility that it is signs of this we see in the above mentioned data [25] seems interesting.

3.2.3 Modified Quark Scattering Models and QCD

In "modified quark scattering models" it is assumed that the dominant process is qq scattering. The absence of p_T^{-4} dominance is explained in different ways. For instance Feynman, Field and Fox [28,29] assumed that the quark-quark elastic cross section is more complicated than originally thought. They chose a phenomenological qq cross section

$$\frac{d\hat{\sigma}}{d\hat{t}} = \frac{2300\ \text{mb}}{\hat{s}\cdot\hat{t}^3} \qquad (3.7)$$

and got impressive fits to data, especially when they took parton transverse momenta into account. "^" denotes physical variables on parton level. They have, however, run into serious problems with this model concerning their predictions on correlations in two-particle inclusive production [30,40] and on elastic scattering [24,27].

Another way of phenomenologically fixing the elementary cross section is by multiplying the one-gluon-exchange quark scattering amplitude by a factor

$$F^2(\hat{t}) = 1/(1 - \frac{\hat{t}}{B})^2$$

With a value of $B \simeq 18(\text{GeV})^2$ good fits are obtained to a variety of inclusive, single particle production data [31].

Still another approach is to assume one-gluon-exchange qq scattering to be dominating, but to incorporate in the theory strong scale-breaking in distribution and fragmentation functions and to let the strong coupling constant be $\hat{t}$-dependent as supposed in asymptotic freedom theories [32]. Calculations then show [32] that the one-gluon-exchange p_T^{-4} qq-process should start to contribute significantly to π -production at $p_T \approx 9$ GeV/c. Although achieved in a rather different way, this result is in remarkable agreement with the Blankenbecler-Brodsky-Gunion prediction.

In [30,33] systematic surveys are given of how QCD-calculations of the $qq \to qq$ subprocess in the range $p_T \leq 6$ GeV/c can change from the purely scaling p_T^{-4} -behaviour to p_T^{-8} by successively taking into account asymptotic freedom initiated $\hat{t}$ -dependence of the strong coupling constant, $\hat{t}$ -dependence of the quark distribution functions, $\hat{t}$ -dependence of the quark fragmentation functions, quark transverse momentum, and gluon contributions.

3.3 Exclusive Two-Body Scattering

We will now turn to exclusive two-body reactions of the type

$$A + B \to C + D \tag{3.8}$$

where all the four hadrons are identified. Special attention will be given to elastic scattering, where the two particles in the final state are identical to the two incoming ones.

The small cross sections involved have the implication that relatively

small amounts of high energy, wide angle elastic scattering data exist.

We start with a short presentation of relevant experimental results.

3.3.1 Elastic Scattering Data

Fig. 3.4 shows the t-dependence of the differential cross section $\frac{d\sigma}{dt}$ for elastic p, $\bar{p}$, π^+, π^-, K^+, K^- scattering on protons at 5 GeV/c lab. momentum.

The curves show the well known behaviour of a forward peak with a cross section at $t = 0$ of several tens of millibarns/$(GeV)^2$ and rapidly falling with increasing $-t$. We also observe less pronounced backward peaks (except for pp since backward scattering is trivially identical to forward scattering for identical particles). The t-domain between the forward and backward peaks is the large angle domain on which we will concentrate.

We see that the cross sections in this area have dropped by two to six orders of magnitude from $t = 0$.

The π^+ and π^- cross sections show signs of structures in the large angle domain, whereas the others seem to be more smooth.

It is interesting to note the similarity between the $\bar{p}$ and K^- cross sections.

An important observation is that at $-t$ around $6(GeV/c)^2$ these two cross sections are more than one order of magnitude lower than the others.

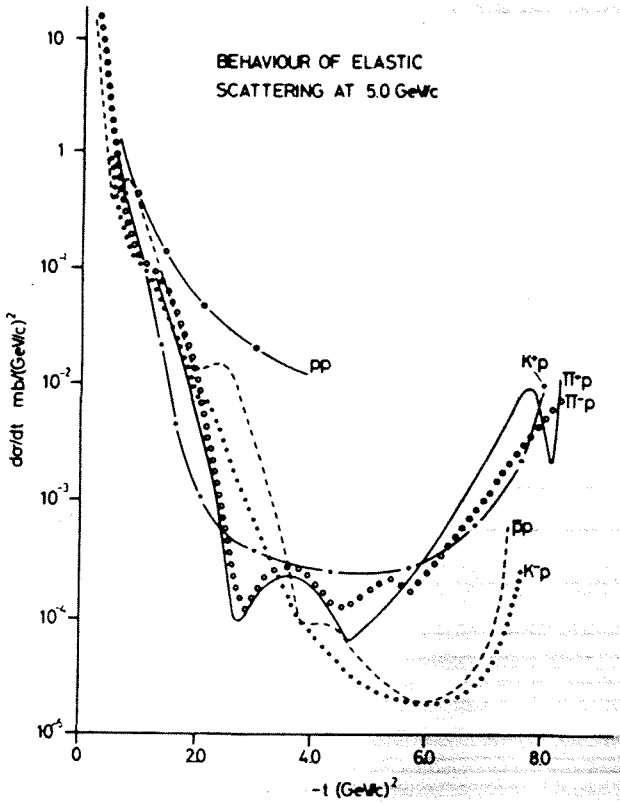

Fig. 3.4
The general behaviour of elastic cross sections at 5 GeV/c (from [34]).

Fig. 3.5 shows the $\pi^{\pm}$ and K^{+} elastic cross sections at 10 GeV/c lab. momentum. We see that the structures in the large angle domain seem to be less pronounced at this energy. We also note a fall-off of the large angle cross sections by more than two orders of magnitude from the 5 GeV/c case of fig. 3.4.

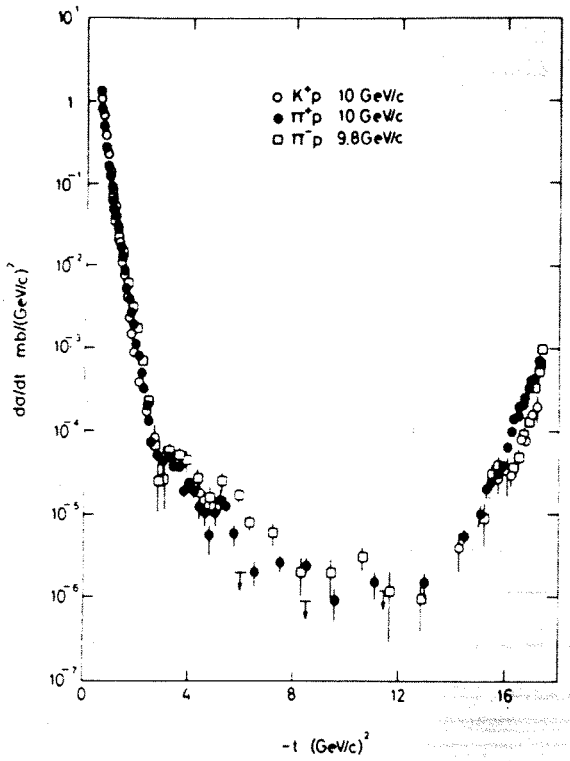

Fig. 3.5
Elastic $\pi^{\pm}$ and K^{+} cross sections around 10 GeV/c (from [36]).

Fig. 3.6 presents a compilation of pp elastic scattering differential cross sections at different lab-momenta from 3 to 1500 GeV/c. We see the gradual evolution of the famous dip with a second maximum around $-t \approx 2(\mathrm{GeV/c})^2$. In the large angle region outside the second maximum all the data seem to be consistent with a structureless behaviour.

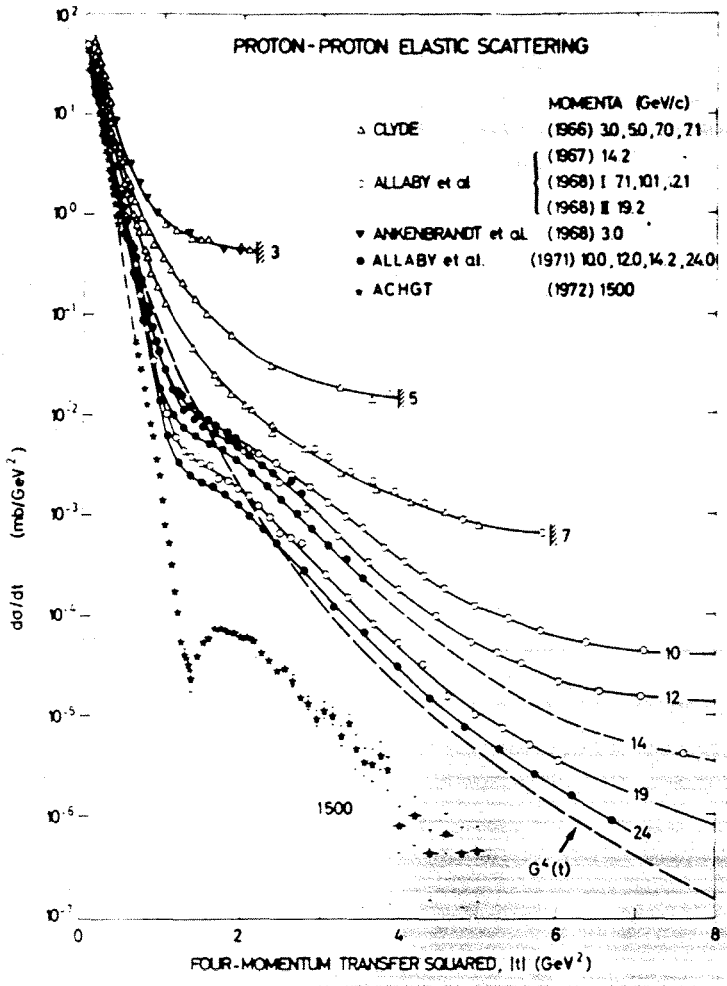

Fig. 3.6 pp elastic scattering data at different energies (from [34]).

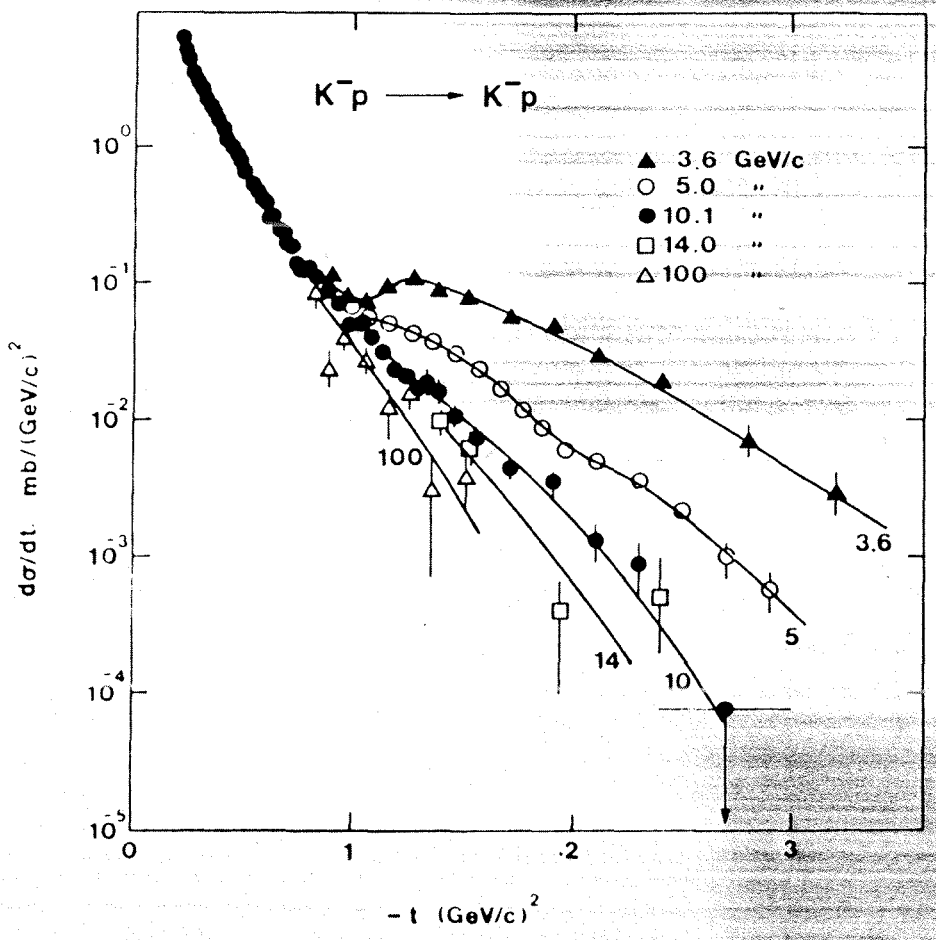

Fig. 3.7 K⁻p elastic scattering data at different energies (from [35]).

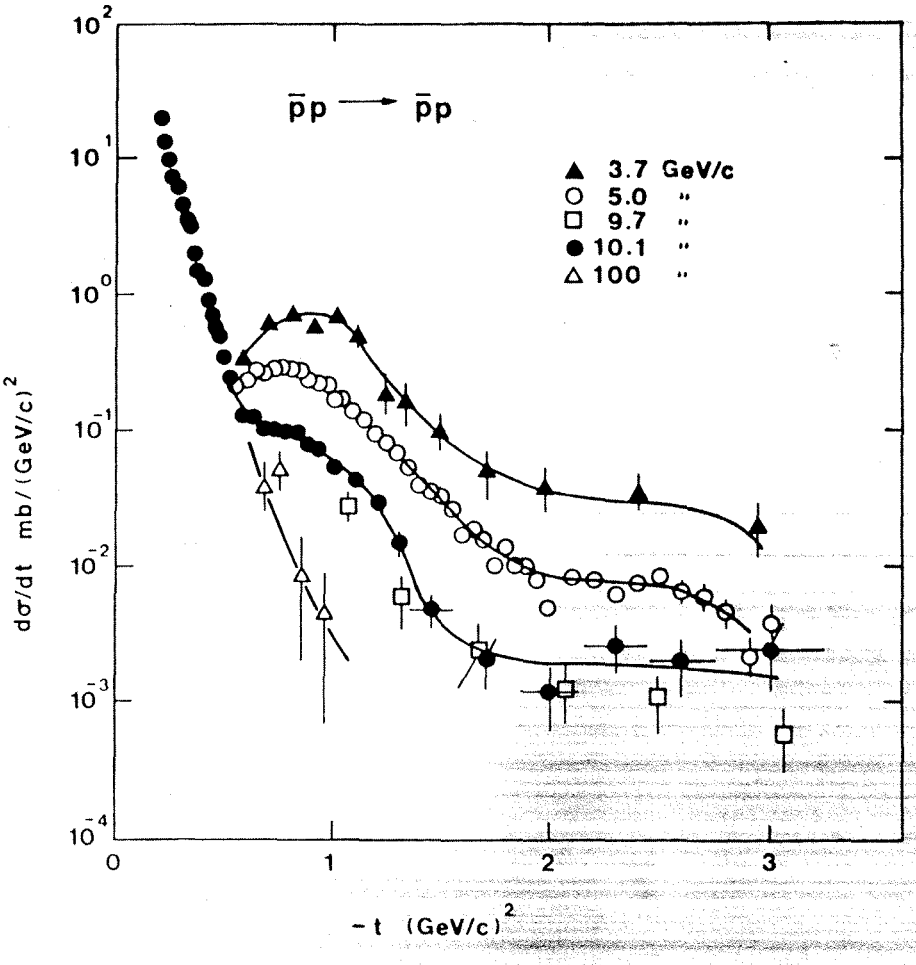

Fig. 3.8 $\bar{p}p$ elastic scattering data at different energies (from [35]).

Little high energy, large angle elastic K^-p and $\bar{p}p$ scattering data exist. Figs. 3.7 and 3.8 show K^-p and $\bar{p}p$ elastic cross sections at lab.momenta varying from 3.6 to 100 GeV/c in the near forward direction, $-t \lesssim 3$ (GeV/c)^2.

Fig. 3.9 shows recent data on $\bar{p}p$ elastic scattering at 12 GeV/c for larger -t-values.

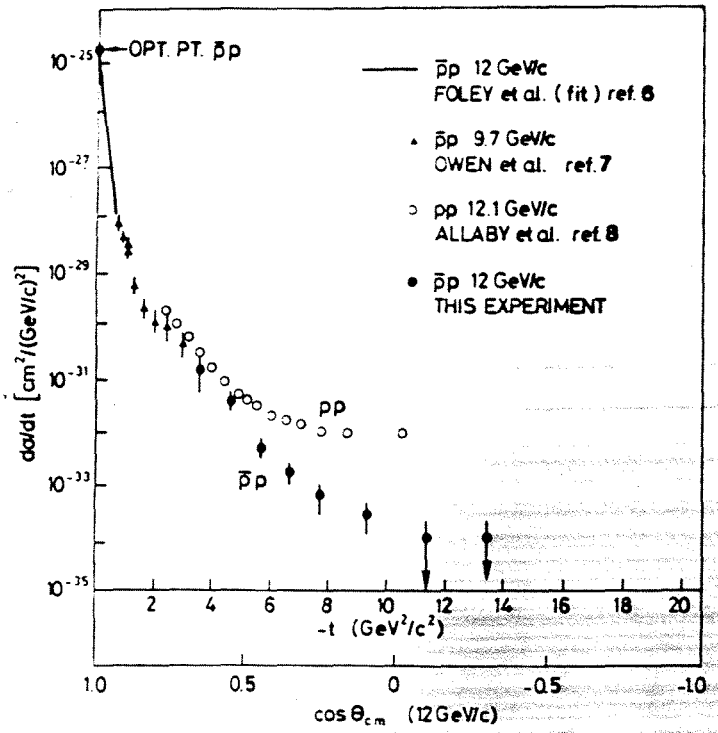

Fig. 3.9
$\bar{p}p$ elastic scattering (from [37]).

3.3.2 Theoretical Approaches to Elastic Large-Angle Scattering

We will restrict this discussion to the following two points :

(i) The idea of dimensional counting which under quite general assumptions predicts the fixed-angle energy dependence of the differential cross sections.

(ii) The constituent interchange model (CIM) which gives predictions both on fixed-angle energy dependence and the angular dependence of the differential cross sections.

(i) Dimensional Counting

The probability for transition from an initial state $|i\rangle$ to a final state $|f\rangle$ in terms of the invariant matrix element M_{if} is given by

$$P_{if} = \frac{|M_{if}|^2}{\prod_k (2E_k V)} (2\pi)^4 |\delta^4(\sum_i P_i - \sum_f P_f)|^2 \qquad (3.9)$$

in standard S-matrix theory [1]. The product extends over all elementary fields participating in the reaction. Being a probability, P_{if} is dimensionless.

V is a normalization volume and has dimension $(\text{length})^3$ or $(\text{energy})^{-3}$. Therefore the denominator of eq.(3.9) has dimension $(\text{energy})^{-2N}$ when N is the total number of elementary fields participating in the reaction. The δ-function contributes with dimension $(\text{energy})^{-8}$. Since P_{if} is dimensionless, we can conclude that M^2 has dimension $(\text{energy})^{8-2N}$.

From the formula

$$\frac{d\sigma}{dt} \propto \frac{1}{s^2} |M_{if}|^2 \qquad (3.10)$$

it follows that $\frac{d\sigma}{dt}$ has dimension $(\text{energy})^{4-2N}$. Now, if quark masses do not enter the formula for large angles and if the quarks have zero transverse momenta and we look at fixed angle exclusive scattering (i.e. t/s fixed), the process is essentially described by only one variable of dimension (energy), namely $\sqrt{s}$.

We can then write [23,40] :

$$\left(\frac{d\sigma}{dt}\right)_{\text{fixed angle}} \propto (\sqrt{s})^{4-2N} = s^{2-N} \qquad (3.11)$$

In the high energy limit we assume that the number N of elementary fields participating in the reaction is the sum of the numbers of valence quarks before and after the collision.

The dimensional counting rule predictions are summarized in table 3.2.

Table 3.2 Dimensional Counting Rule Predictions (see the text).

Reaction	N	Fixed angle energy behaviour
$pp \to pp$ $\bar{p}p \to \bar{p}p$	12	s^{-10}
$\pi^- p \to \pi^- p$ $\pi^+ p \to \pi^+ p$ $K^- p \to K^- p$ $K^+ p \to K^+ p$	10	s^{-8}

Fig. 3.10 shows the 90°CM pp elastic cross section as a function of energy. The agreement with the s^{-10}-prediction seems rather good.

One should note, however, that the datapoints seem to oscillate around the s^{-10}-line in a rather regular fashion. This has lead to suggestions that we still at these energies observe effects from the finite hadronic size [38].

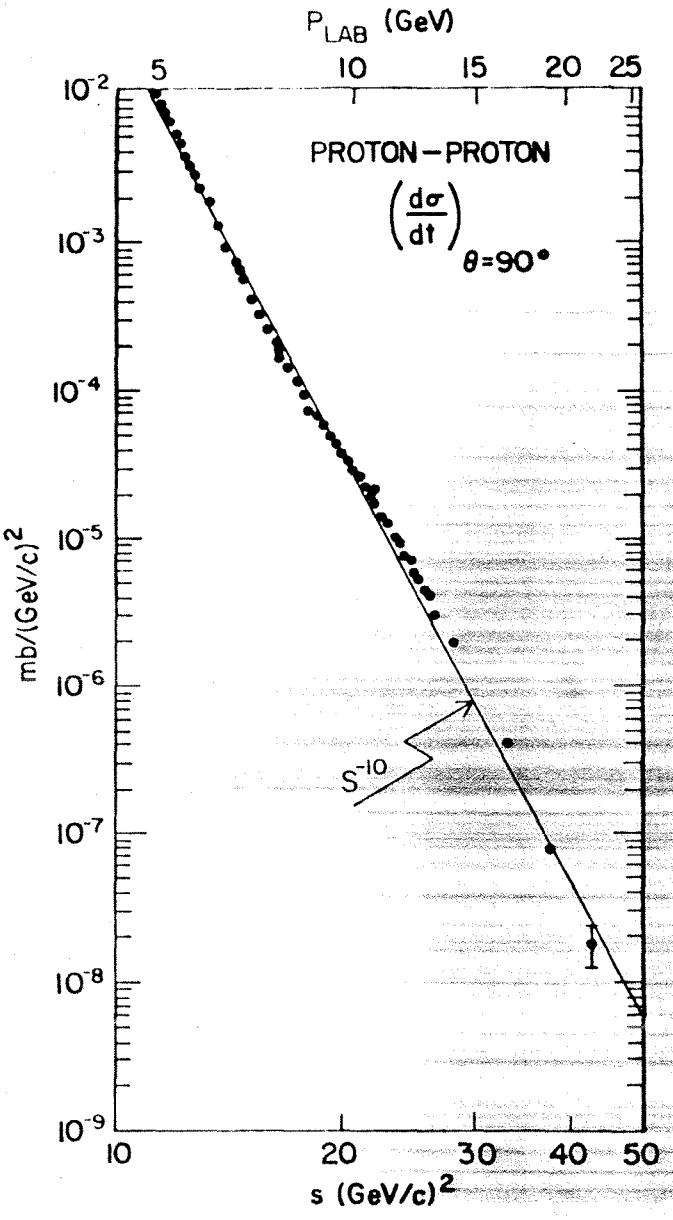

Fig. 3.10

Energy-dependence of 90^{o} elastic pp cross section (from [20]).

Figs. 3.11 (a) and (b) show the fixed angle energy dependence of $\pi^- p$ and $\pi^+ p$ elastic scattering. The π^--data tend to agree with s^{-8} at the higher energies, whereas the situation for π^+ seems to be more unclear.

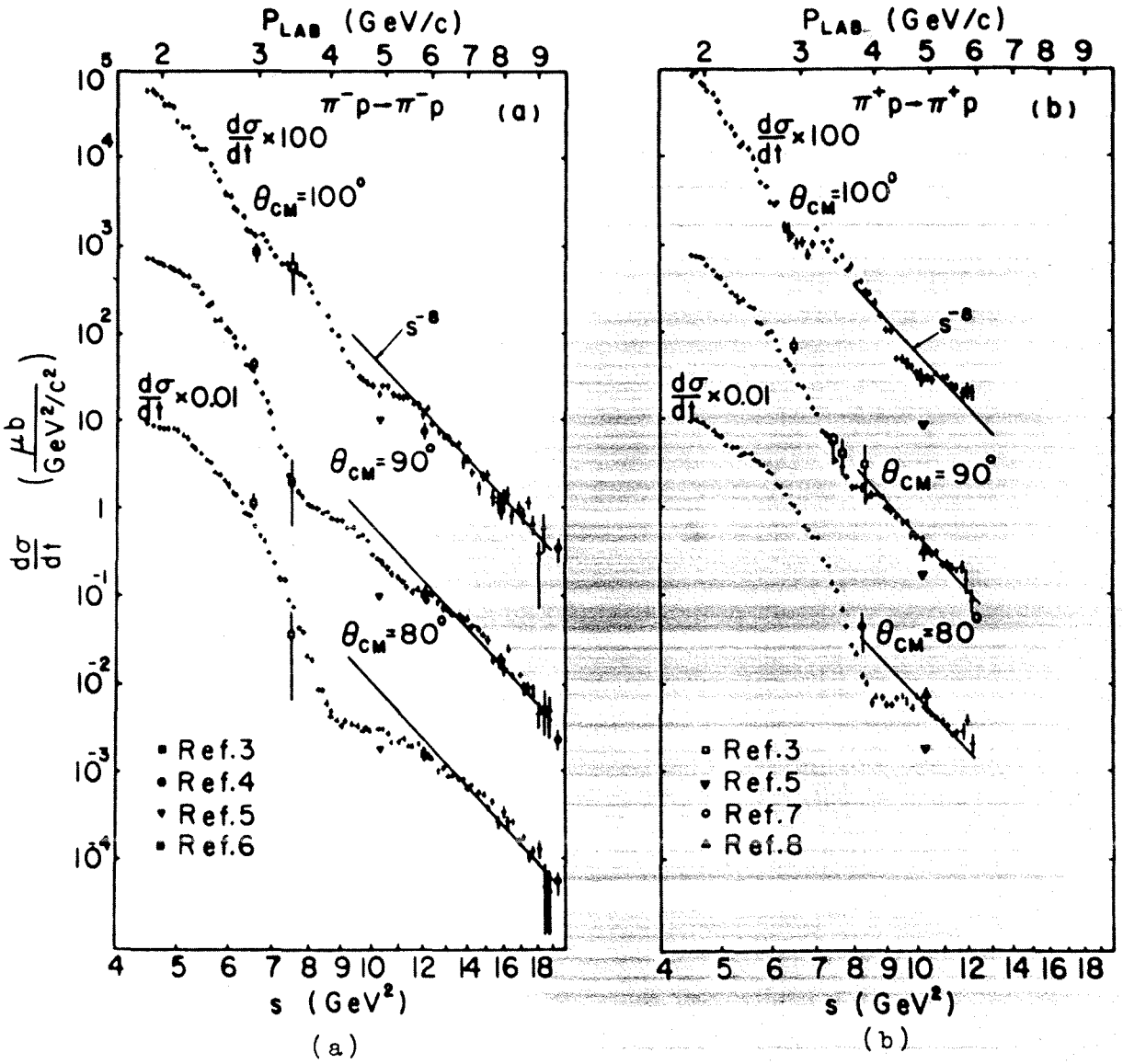

Fig. 3.11 (from [39])

(a) Fixed-angle energy dependence in $\pi^- p$ elastic scattering.

(b) Fixed-angle energy dependence in $\pi^+ p$ elastic scattering.

(ii) The Constituent Interchange Model

The idea of constituent interchange (fig. 3.3(b)) being the dominating subprocess in violent hadron-hadron collisions as discussed in section 3.2.2 was originally applied to exclusive two-body reactions [26]. This model gives predictions on angular dependence and ratios between cross sections which qualitatively seem reasonable. Also fixed-angle energy dependences are predicted.

The simplest version of the theory assumes the constituents to be the valence quarks and that the interaction time only allows for one single quark interchange during a collision. Thus it is expected to give good results only in the asymptotic region $s, |t|, |u|$ large.

The hadrons are assumed to act like bound systems of a quark (antiquark) plus a core. The core is identified with an antiquark (quark) in mesons, and a di-quark (di-antiquark) in baryons (antibaryons). Depending on the quark content, the model predicts quite different angular distributions for different beam particles.

For the meson-proton elastic cross sections, the CIM model predicts [21,26]

$$\frac{d\sigma}{dt}(Mp \to Mp) \propto s^{-8} \frac{(1+z)}{(1-z)^4} R^2(z) \qquad (3.12)$$

where $z = \cos\theta_{CM}$. $R(z)$ for some reactions are given in table 3.3. It should be noted that the predicted energy behaviour agrees with dimensional counting.

Table 3.3 CIM angular functions (see the text)

Reaction	R(z)
$\pi^+ p \to \pi^+ p$	$4\alpha(1+z)^{-2} + \beta$
$\pi^- p \to \pi^- p$	$4\beta(1+z)^{-2} + \alpha$
$K^+ p \to K^+ p$	$4\alpha(1+z)^{-2}$
$K^- p \to K^- p$	α

Simple quark counting suggests values of $\alpha = 2, \beta = 1$ [21,26].

For pp scattering the prediction is [26]

$$\frac{d\sigma}{dt}(pp \to pp) \propto s^{-12}(1-z^2)^{-5.2} \qquad (3.13)$$

One should note that this contradicts the dimensional counting rule prediction of an s^{-10} energy dependence. It is argued [40,41] that this difference arises because the CIM model treats the nucleon as a quark plus a core, whereas the dimensional counting result assumes a three-quark structure of the proton.

The CIM model also predicts the ratio between pp and $\bar{p}p$ elastic differential cross sections [26] :

$$\frac{d\sigma}{dt}(pp \to pp) \Big/ \frac{d\sigma}{dt}(\bar{p}p \to \bar{p}p) \propto \left(\frac{2}{1+z}\right)^{5.6} \qquad (3.14)$$

In fig. 3.12 the CIM angular predictions for π^+ and K^+ are compared to data at 5 and 10 GeV/c lab. momentum.

Fig. 3.13 shows the CIM prediction on the ratio $\frac{d\sigma}{dt} \Big/ \left(\frac{d\sigma}{dt}\right)_{90^\circ}$ for $\pi^- p$ elastic scattering at three different lab. momenta.

Both fig. 3.12 and 3.13 show a qualitative agreement with data, but more high precision data at high energies are required before any safe conclusions may be drawn.

Finally fig. 3.14 shows data on the ratio of eq.(3.14) at 90^{o} in CM. The highest energy data points might be signs of agreement with the CIM prediction, but more data is desirable.

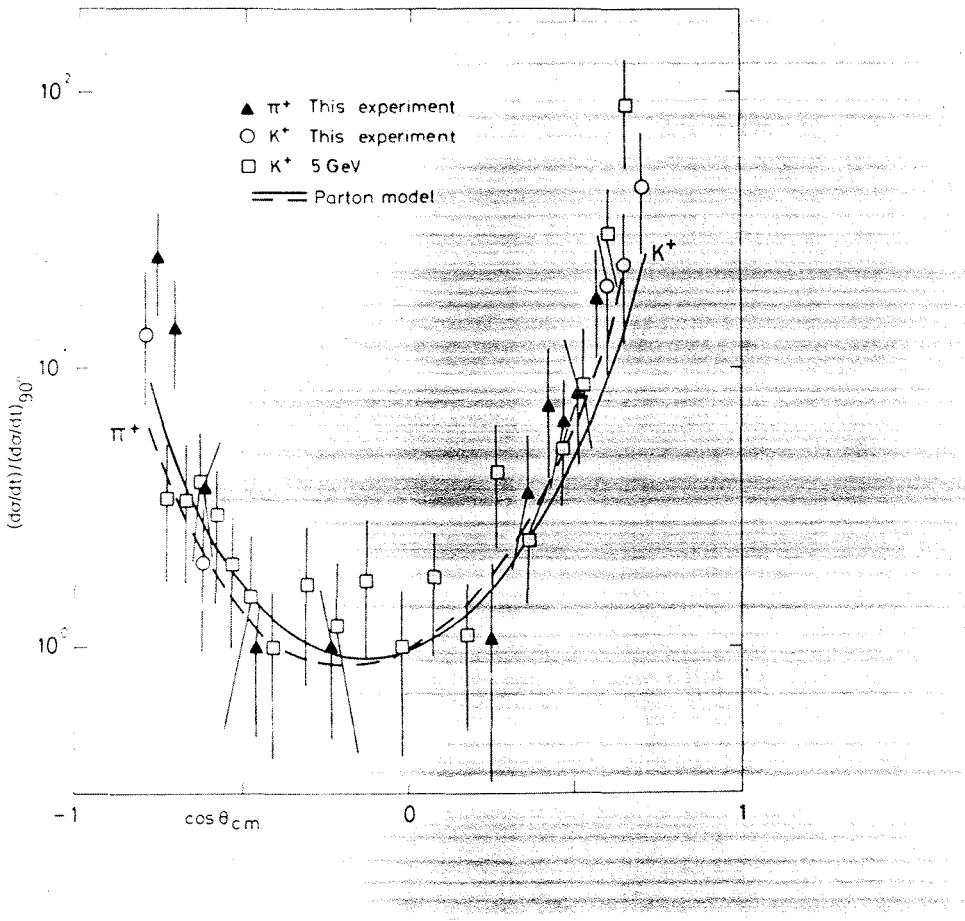

Fig. 3.12
CIM predictions for $\pi^{+}p$ and $K^{+}p$ elastic scattering compared to data. "This experiment" refers to 10 GeV/c lab momentum (from [42]).

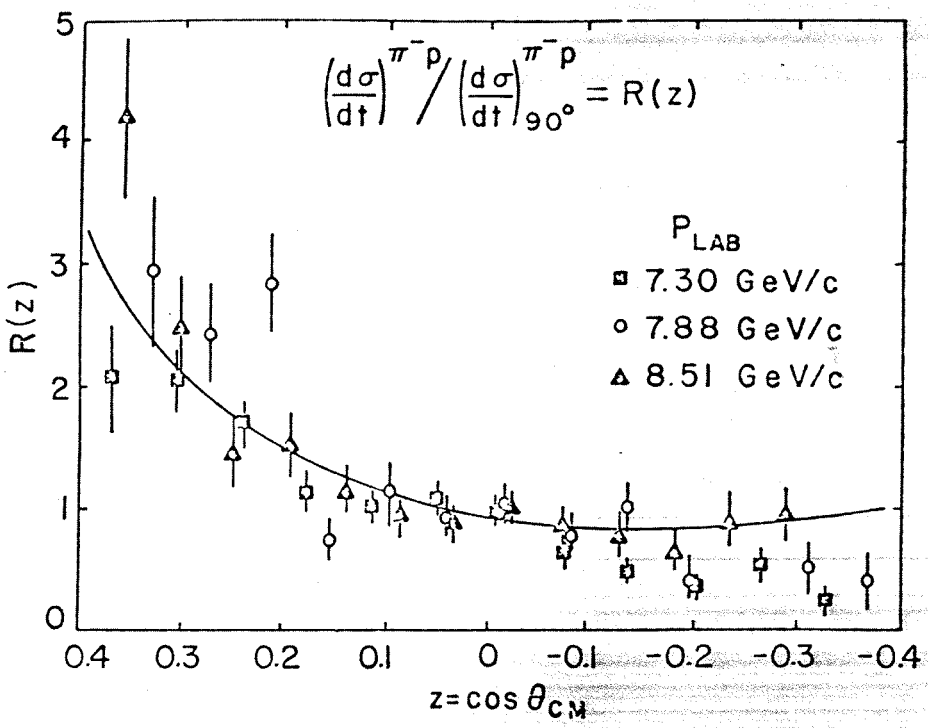

Fig. 3.13

CIM prediction compared to $\pi^- p$ elastic scattering data (from [39]).

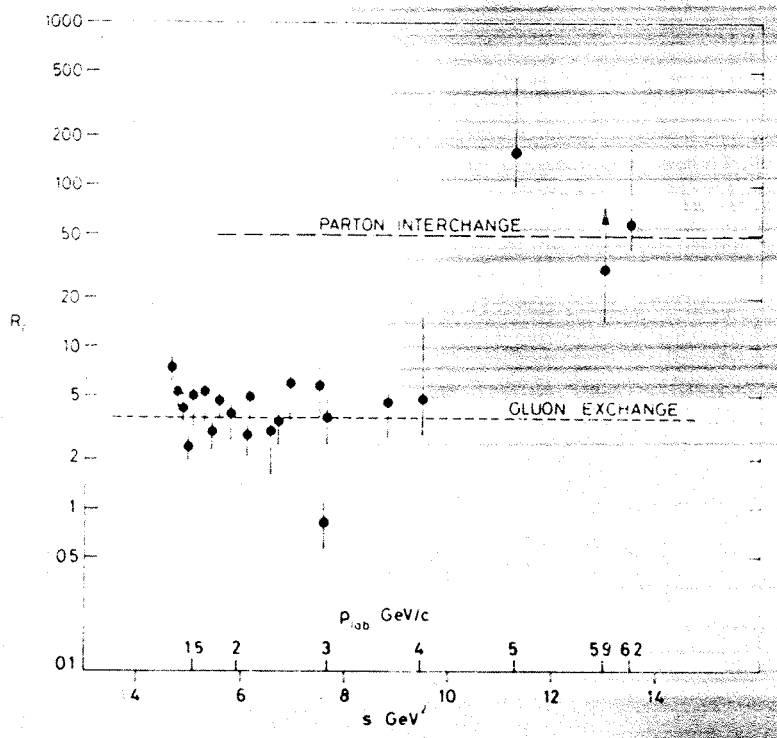

Fig. 3.14

The ratio $\left(\frac{d\sigma}{dt}(pp \to pp) \Big/ \frac{d\sigma}{dt}(\bar{p}p \to \bar{p}p)\right)_{90^\circ}$ compared to CIM (parton interchange) and gluon exchange predictions (from [43]).

3.3.3 Final Remarks

We have seen that theoretical ideas exist which qualitatively reproduce the main features of high energy, wide angle scattering data.

Large angle, high energy elastic scattering is, however, a difficult process to measure and the experimental situation is at present characterized by a relatively small amount of data. More data is required before any final conclusions with respect to the different models can be drawn.

The remainder of this thesis is devoted to the description of an experiment which, hopefully, will be a new step towards this goal, the CERN SPS- experiment WA7.

Some preliminary results from this experiment will be presented in the last chapter.

PART II THE SPS-EXPERIMENT WA7

Introduction

The second part of this thesis is devoted to the description of the SPS-experiment WA7.

In chapter 4 the lay-out and apparatus is described and discussed.

Chapter 5 deals with the chain of off-line analysis programs, and chapter 6 describes the Monte Carlo program together with some of its applications.

Finally some details from the analysis and some preliminary results are presented in chapter 7.

CHAPTER 4 THE WA7 EXPERIMENT - APPARATUS AND DATA-TAKING

4.1 Introduction

We now turn to the description of the experiment WA7 at the CERN SPS [45].

This experiment is performed by a collaboration of groups from LAPP (Annecy), CERN, NBI (Copenhagen), Genova, UCL (London), and Oslo. Its aim is primarily to study the following high energy, wide angle exclusive scattering processes at laboratory momenta from 20 to 100 GeV/c:

(1) $\pi^{\pm} p \rightarrow \pi^{\pm} p$

(2) $K^{\pm} p \rightarrow K^{\pm} p$

(3) $pp \rightarrow pp$

(4) $\bar{p}p \rightarrow \bar{p}p$

(5) $\bar{p}p \rightarrow \pi^{+}\pi^{-}$

(6) $\bar{p}p \rightarrow K^{+}K^{-}$

In addition there exist several possibilities to extend the experimental programme. One can extend the angular range for the processes (1) - (6) towards smaller angles, and one can regard other reactions. Examples of alternative processes which are well suited for observation with the already existing equipment, are production of heavy mesons which decay into two muons, and inclusive production of two large p_T hadrons.

Because of the low cross sections for the reactions (1) - (6), the experiment is designed for a high intensity beam of $\sim 10^8$ particles per burst.

4.2 Layout and Coordinate System

The horizontal projection of the general experimental layout is shown in fig. 4.1. The code will be explained in the subsequent sections.
The WA7 coordinate system has its positive z-axis along the central beam line. The y-axis points vertically upwards. The x-axis is accordingly horizontal and points to the left when viewed downstream (se fig. 4.1).

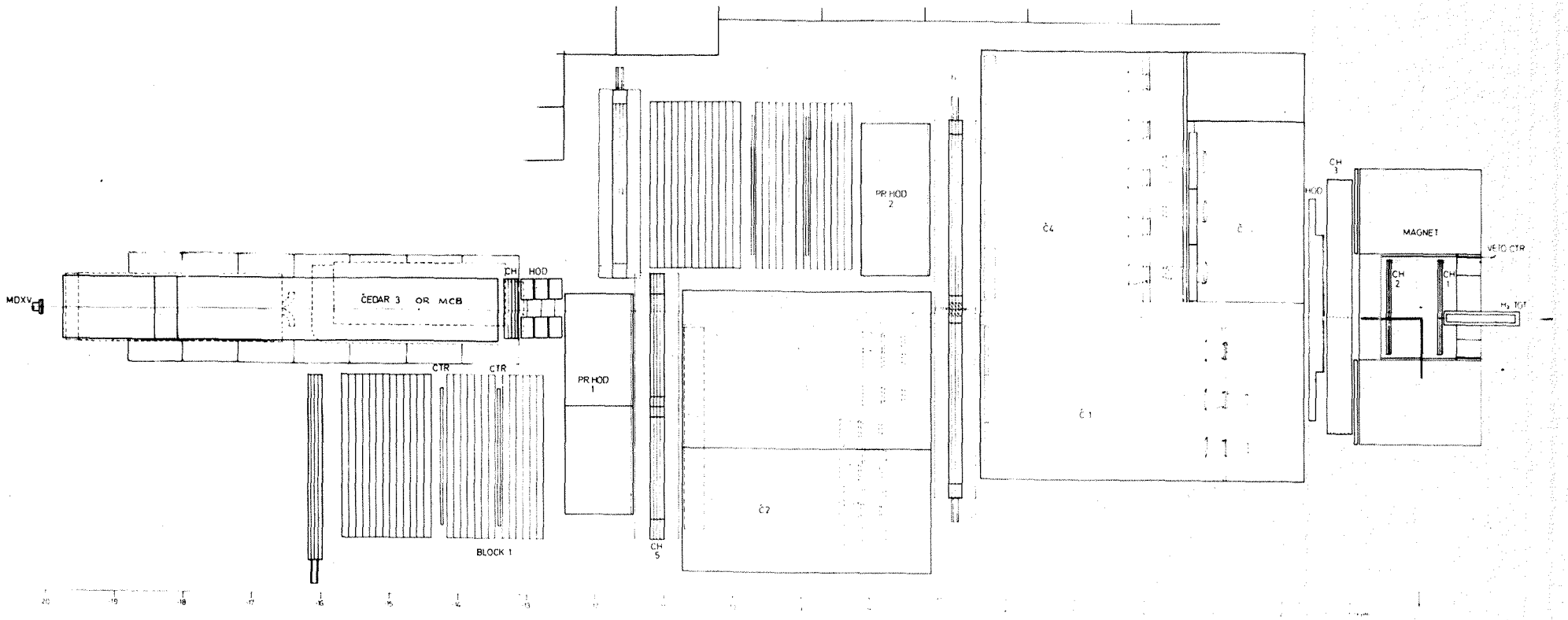

Fig. 4.1
The horizontal projection of the experiment. The code is explained in the text.

4.3 The Beam

The experiment is situated in the SPS West Experimental Area as shown in fig 4.2. Target T3 is struck by $\sim$ 240 GeV/c protons from the SPS. The secondary beam thus produced follows a beam line which is later on split into the E1A/H1A beam line to WA4 and Omega, and the E1B/H1B beam line to WA7 and WA3. It is not possible to have beams in the E1A/H1A and E1B/H1B lines simultaneously.

The angular acceptance for the secondary beam is ± 1.2 mrad in x and $\pm$ 2.8 mrad in y. The momentum acceptance is $\Delta p/p \sim 2\%$ [46]. Maximum momentum is 100 GeV/c.

The beam optics is shown in fig. 4.3. It consists of a system of dipole bending magnets (BEND, TR), quadropole magnets for beam focusing (Q), and collimators (CH, CV *) for spatial definition of the beam.

Beam monitoring devices are four multiwire proportional chamber planes (dotted lines in fig. 4.3), scintillation counters, an ionization chamber, and three differential Cerenkov counters (CEDARs) - two upstream of the experiment and one downstream. The CEDARs and the ionization chamber are shortly described in the following sections.

Four of the scintillation counters are mounted around the beam upstream of the target. They constitute the beam veto counter which counts the halo.

Important variables such as magnet currents and polarities, collimator slit widths, and CEDAR apertures and pressures, are computer controlled from the WA7 control room.

---

* H means horizontal and V means vertical.

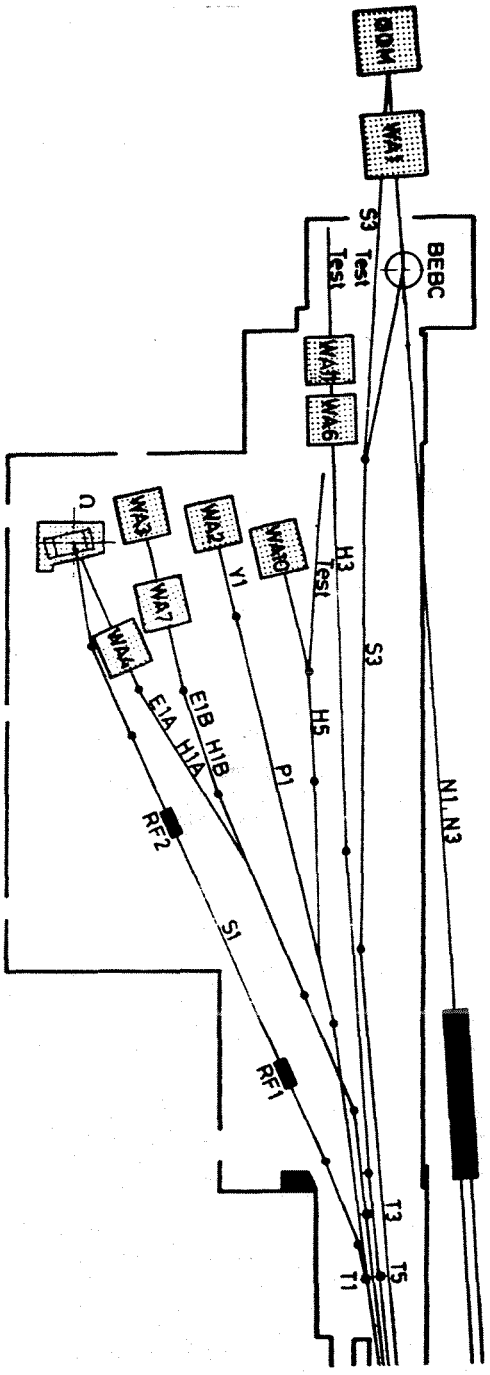

Fig. 4.2

Location of the experiment in the West Area (from [46]).

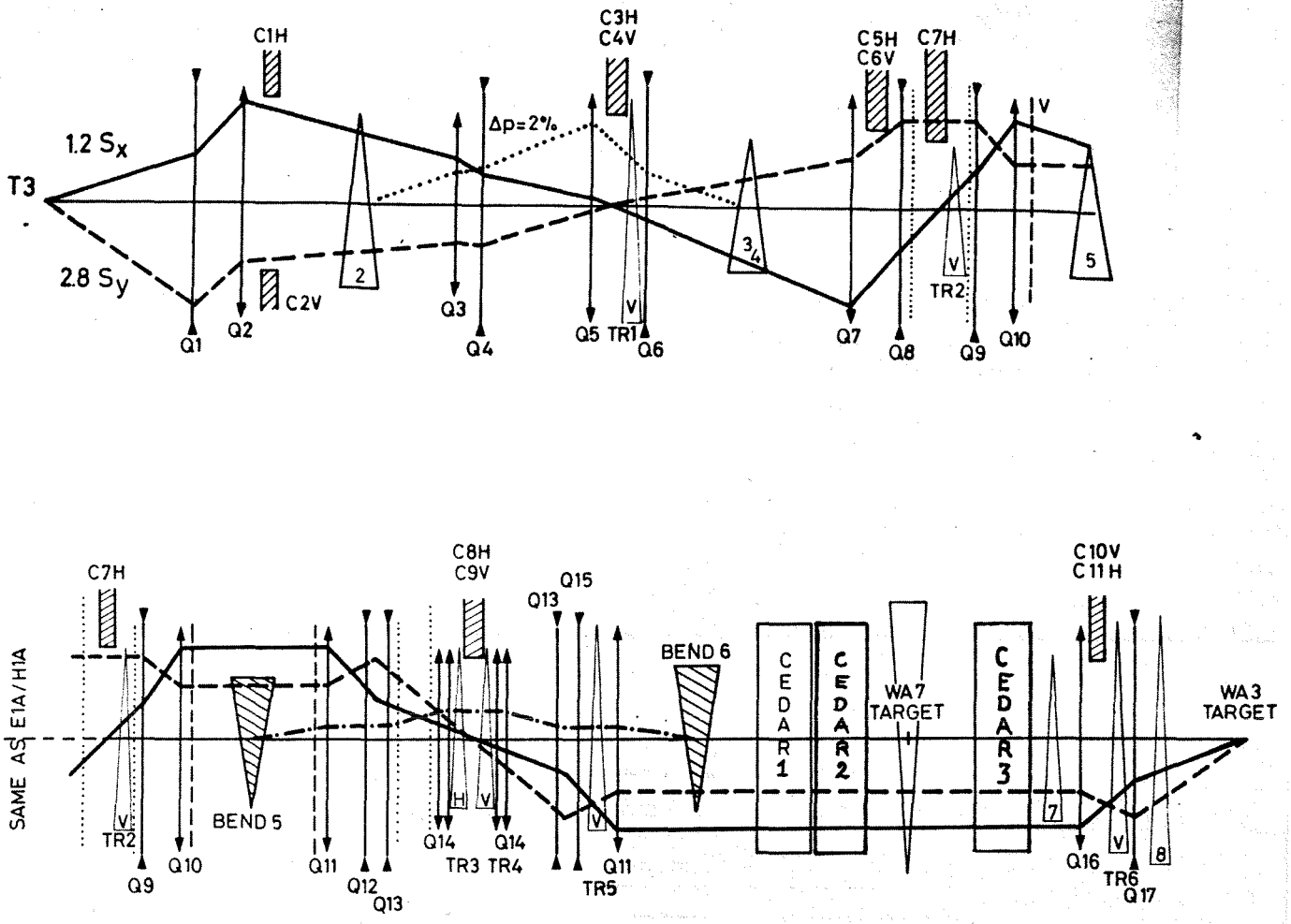

Fig. 4.3

The E1B/H1B beam line (from [46], but slightly updated).

$1.2\,S_x$ ($2.8\,S_y$) corresponds to the deviation in x (y) from the central beam line of a particle which was produced at central beam line with an angle in x (y) of 1.2 (2.8) mrad. These are the maximum angles accepted.

4.3.1 The CEDARs

The CEDARs (Cerenkov Differential counter with Acromatic Ring focus) [47] are used for beam particle identification. They are 6 m long differential Cerenkov counters filled with N_2 at pressures from 1.6 to 8 atmospheres [47]. The ring of reflected Cerenkov light passes through a circular slit, the light diaphragm, of radius 10 cm, and is detected by 8 photomultipliers. One may demand 8, 7 or 6 photomultipliers in coincidence to accept a CEDAR signal. The light diaphragm opening can be varied from 0.1 to 20 mm. Pions, kaons, protons, electrons and muons can be distinguished in the whole momentum range in question [47].

Fig. 4.4 shows the working pressure for the CEDARs as a function of momentum for π, K and $\bar{p}$.

During elastic data-taking the three CEDARs are set to count p, K and K, respectively. The reason for using the third counter downstream of the experiment, is the following.

At high momentum the threshold Cerenkov counters of the experiment (see section 4.6) have difficulties in distinguishing π from K. At high intensity there is a possibility of a π and a K arriving inside the counter dead time. If the π scatters and the K does not, the event could be misidentified as a K -scattering. This possibility of misidentification is ruled out when a third CEDAR downstream of the experiment is set to count K-mesons.

4.3.2 The Ionization Chamber

The ionization chamber is used for beam intensity measurements. It consists of two earth connected collector plates sandwiched between three high voltage plates. The plates are circular and built into a 25 cm long cylindrical frame made from 1 cm thick stainless steel. The beam enters and leaves the chamber through two mylar windows of diameter 12 cm. The chamber is filled with argon gas at atmospheric pressure.

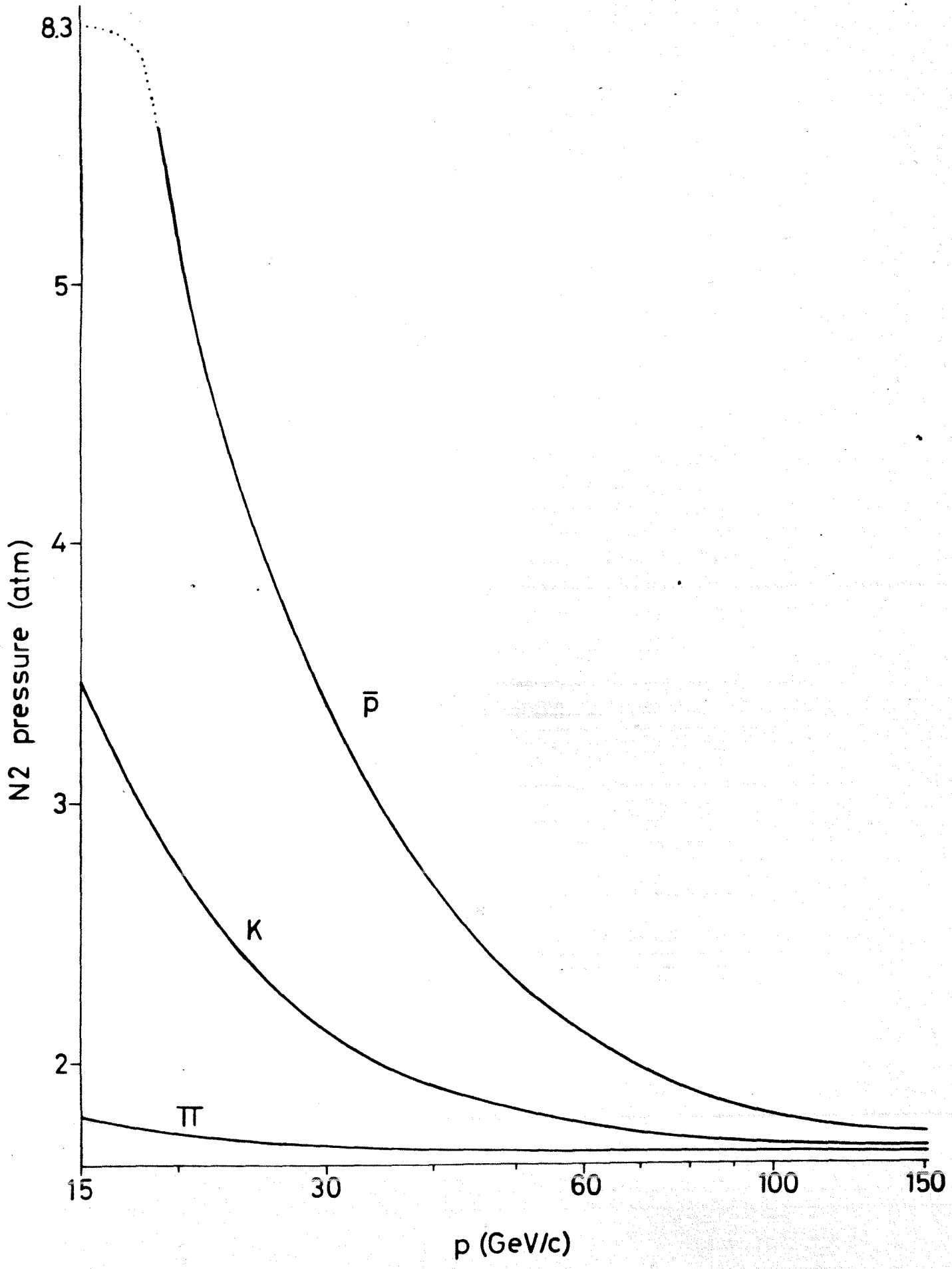

Fig. 4.4
CEDAR working pressures (from [47]).

Each collector plate is split into two parts. One is split horizontally and the other one vertically. Thus the ionization, which is proportional to the beam intensity, is measured separately in the upper, downer, left and right halves of the beam.

The signals from each of the four halfplanes go via an amplifier and an integrator to a scaler.

The ionization chamber is placed upstream of the quadropole Q13 of fig. 4.3.

4.3.3 The Beam Hodoscopes

In order to locate the trigger particle inside the beam, the experiment is equipped with two beam hodoscopes [48].

One is placed immediately in front of the target, and the other one is situated between CEDAR1 and CEDAR2.

Each hodoscope consists of three planes. The planes consist of two rows of 20 scintillators each, arranged as shown in fig. 4.5. The cross section of each scintillator is 2.2×5.0 mm^2, and the length is 10 cm. Each scintillator is viewed through a light guide by a photo multiplier.

The three planes of one hodoscope are mounted with the scintillators vertically and at $\pm$ 45 degrees, respectively.

Since the distance between the hodoscopes is roughly 7 m, they give an angular resolution of about 0.6 mrad on the straight line part of the beam tracks, whereas the spatial resolution is about 2 mm.

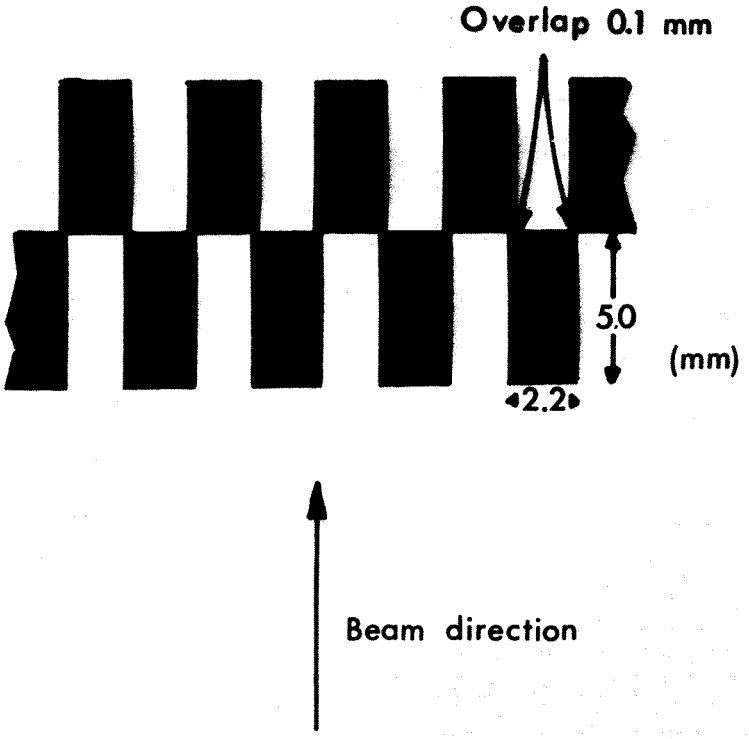

Fig. 4.5
Arrangement of scintillators in a beam-hodoscope plane.

4.3.4 The Beam Composition

Fig. 4.6 shows the calculated particle intensities normalized to 10^{12} interacting protons in target T3, as functions of beam momentum. The hadron intensities correspond to particles within $\frac{\Delta p}{p} \sim \pm 1\%$ whereas the electron intensity corresponds to $\frac{\Delta p}{p} \sim \pm 2\%$.

Target T3 has a thickness in interaction lengths that corresponds to 0.42 reactions per incoming proton [49]. Therefore the expected intensities per 10^{12} incoming protons on T3, are obtained by multiplying the intensities of fig. 4.6 by this factor. I.e., roughly 4.2×10^7 π^- is expected at 20 GeV/c per 10^{12} incoming protons.

However, measured was $\sim 8 \cdot 10^6\ \pi^-/10^{12}$ incoming protons, so the calculations leading to fig. 4.6 are high by a factor more than 5 [49].

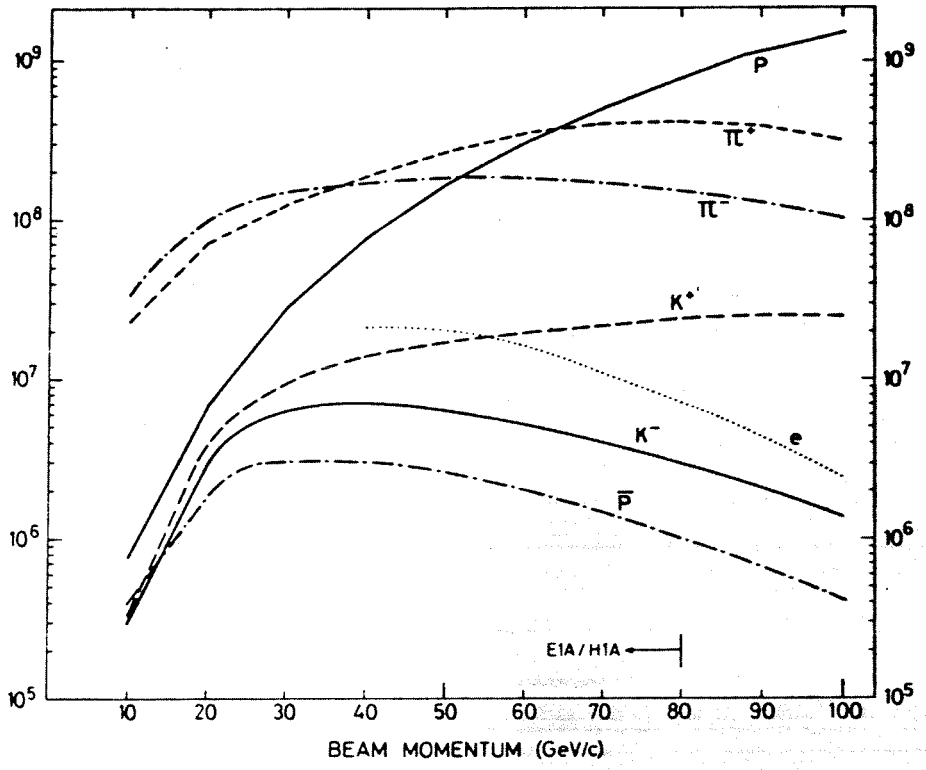

Fig. 4.6
E1/H1 beam calculated intensities per 10^{12} interacting protons (from [46]).

On the other hand, the electron content turned out to be much higher than expected. As seen from fig. 4.7 the e/π ratio in the negative 20 GeV/c beam was as high as ~ 0.8.

Therefore it was decided to put into the beam an electron killer, simply a piece of lead. From fig. 4.7 we can read out the ratios e/π of table 4.1 for different thicknesses of lead.

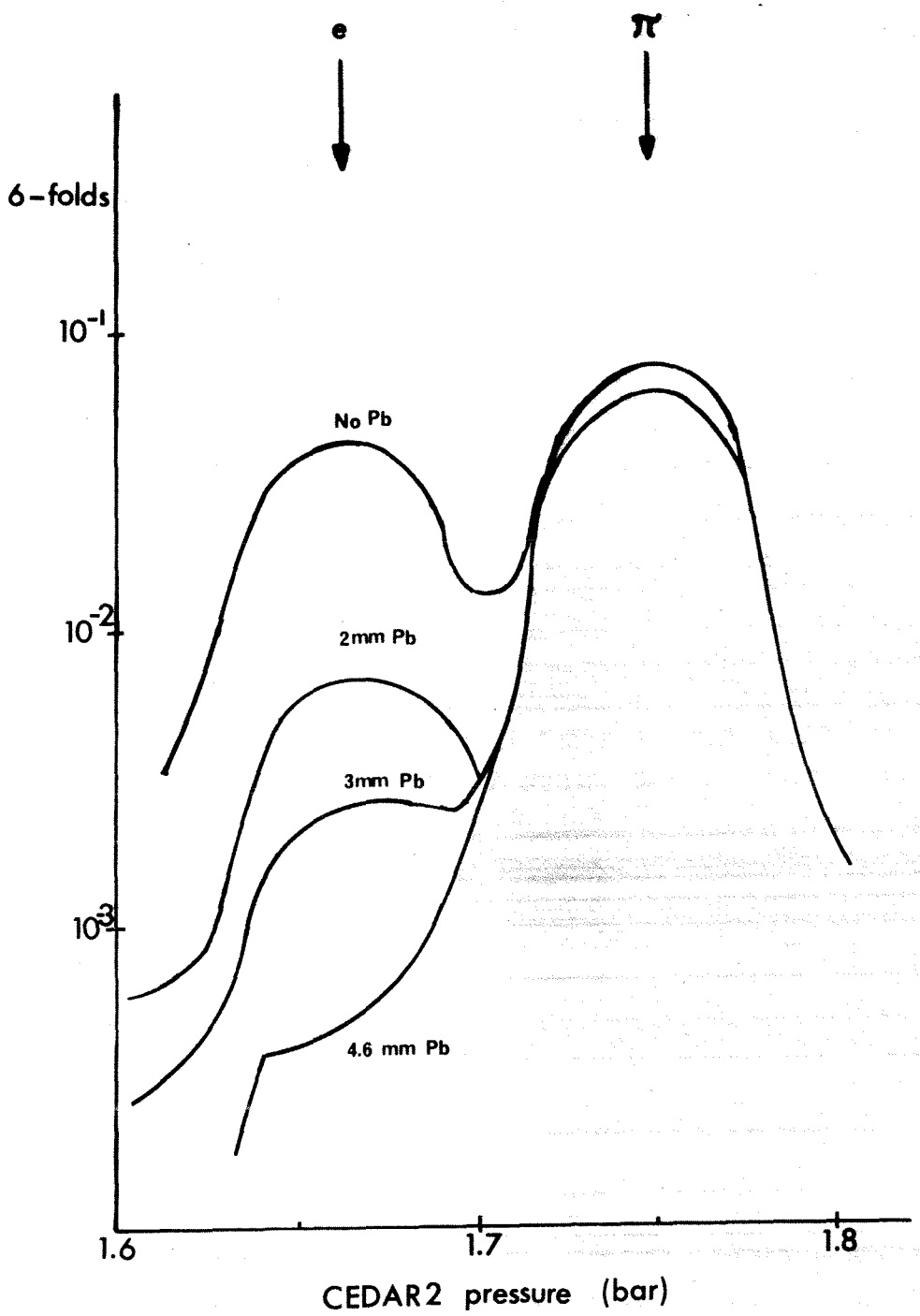

Fig. 4.7
CEDAR2 scanned. Electron content at different thicknesses of lead.

Table 4.1 e/π Ratio at different Thicknesses of Lead.

Pb (mm)	e/π (%)
0	~80
2	~13
3	~ 5
4.6	~ 0

It should be noted, however, that these numbers are uncertain by a factor ~ 2 due to a misalignment of the CEDAR used [50].

Assuming a pure π-beam of 20 GeV/c, 4.6 mm lead reduces the hadron intensity by ~ 3%.

With 4.6 mm lead in the beam, CEDAR scans showed that the ratios between the particle types at 20 GeV/c negative beam were [49]:

$$\pi^-/K^-/\bar{p} = 0.900/0.030/0.028 \qquad (4.1)$$

This is illustrated in fig. 4.8.

Because of the angular spread and resolution problems, it is difficult to measure very accurately the muon content of the beam with the CEDARs. Monte Carlo calculations (D. Plane, see [51]), suggest, however, a μ/π ratio of ~ 6%.

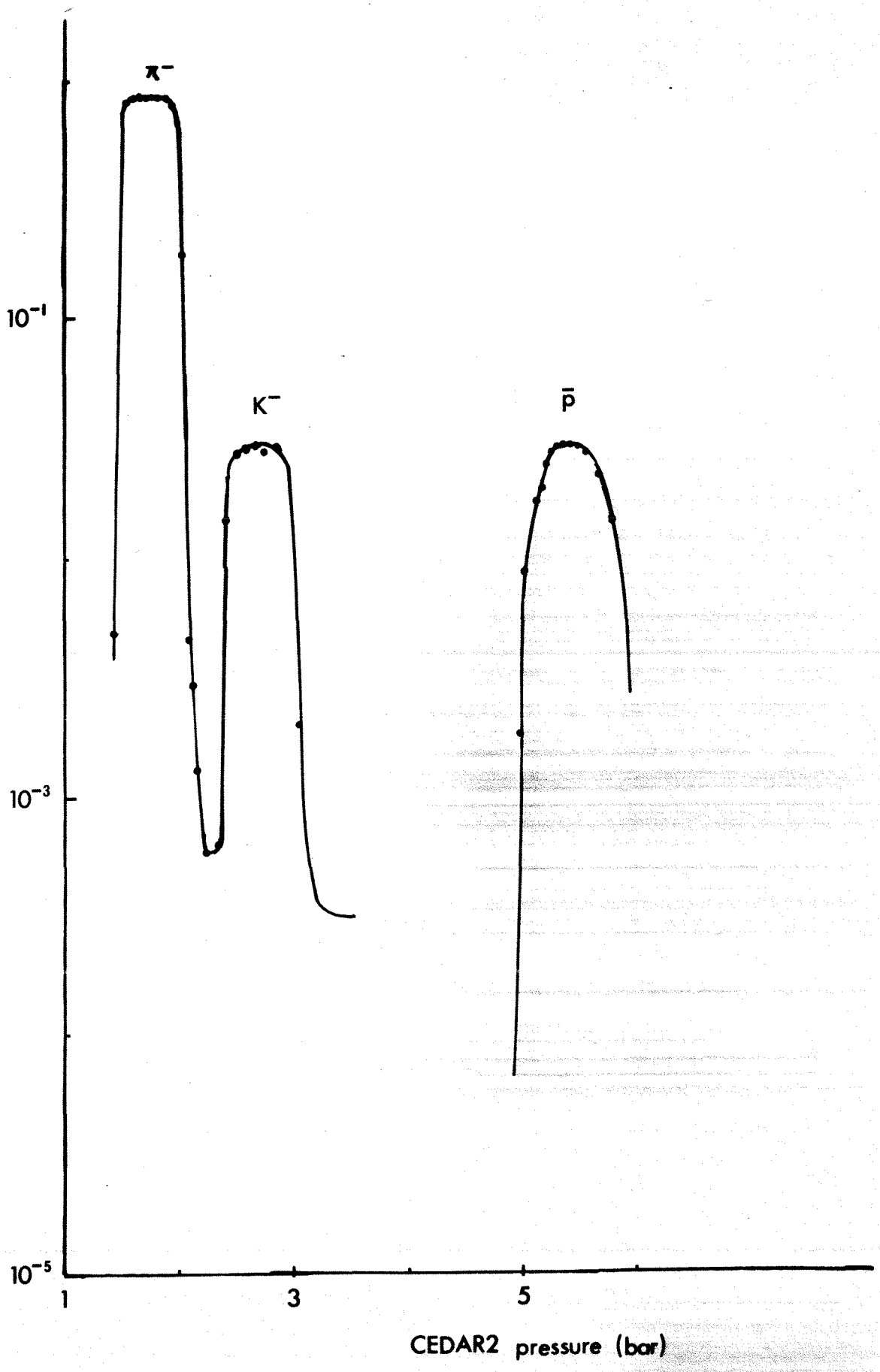

Fig. 4.8
Scan of CEDAR2 (with 4.6 mm Pb in the beam).

4.4 Target and Spectrometer Magnet

The 1 m long liquid hydrogen target is mounted at the magnet entrance and extends partly inside the magnet volume.

The liquid hydrogen is contained in a mylar cylinder of radius 4 cm. The cylinder is mounted between two horizontal frames connected by six stainless steel bars of radius 1 cm.

The spectrometer magnet is an Oerlikon W75. Besides momentum analyzing the tracks, it effectively sweeps away low-momentum background.

The magnet volume is about $2.5 \times 1.9 \times 0.5\ m^3$. At maximum current of 7500 A, the vertical main component of the magnetic field reaches ~ 16 kG. The field integral

$$F = \int B_y dz \qquad (4.2)$$

is about 23 kGm at 7500 A.

In WA7 coordinates the magnetic centre is at $(x, y, z) \approx (-15., 0., -24.)$. The non-symmetric position of the magnet with respect to the beam is chosen for acceptance reasons.

The magnetic field prophile at 7500 A along a line parallel to the beam through the magnet centre, is shown in fig. 4.9.

The vertical inner walls of the magnet are covered by one scintillation counter each, marked VETO CTR. in fig. 4.1. A signal from one of those indicates that one or more particles have hit the magnetic walls.

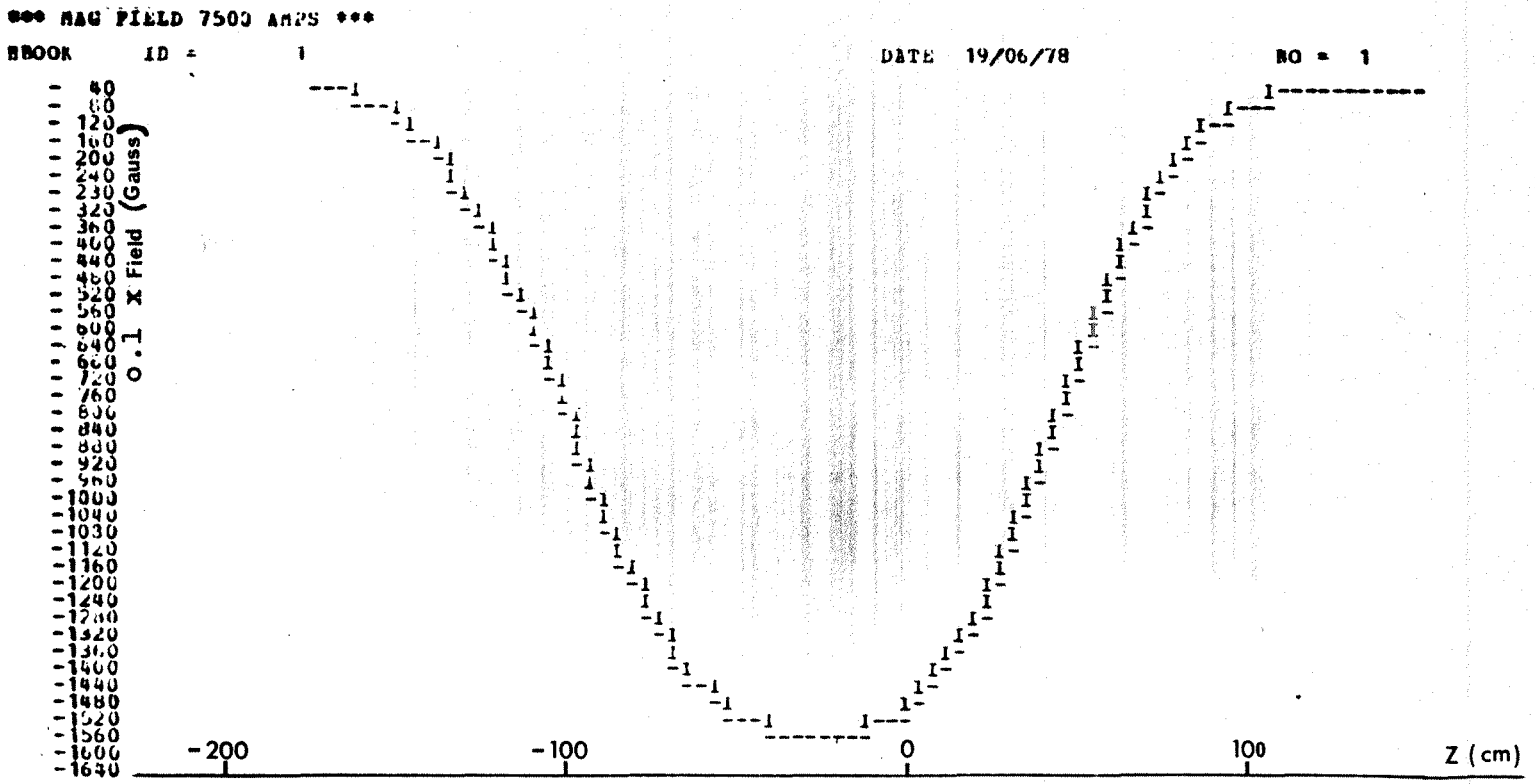

Fig. 4.9

The y-component of the magnetic field at 7500 A along a line parallel to the beam through the magnetic centre.

4.5 The Multi Wire Proportional Chambers (MWPCs)

The experiment is equipped with six assembleys of multiwire proportional chamber planes, called CH1-CH6 in fig. 4.1. They contain altogether 26 wire planes. The MWPCs perform position measurements of the outgoing tracks with an accuracy which is in principle given by the wire spacing. The wire spacings for the different wire planes are given in table 4.2.

The wires measure coordinates in four different projections according to their orientation. These projections are called x, y, u and v, and are defined as shown in fig. 4.10.

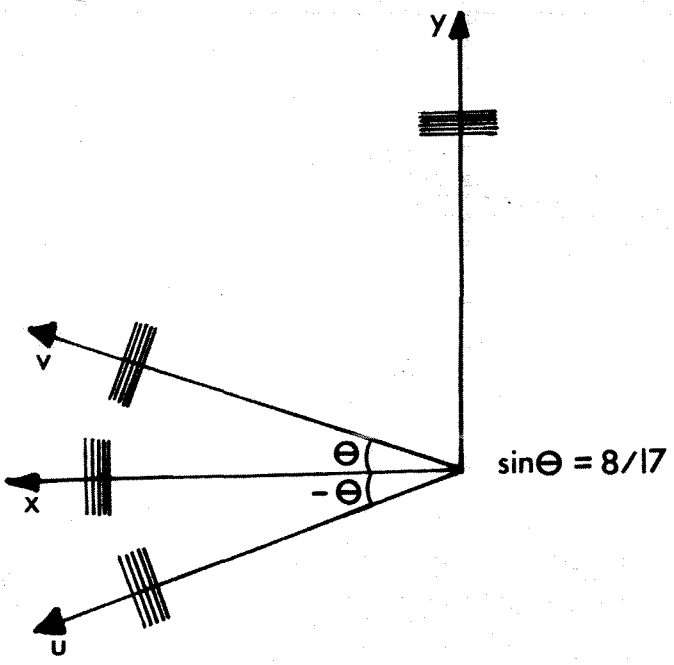

Fig. 4.10
Definition of x,y,u and v. The beam moves in positive z-direction. The wire orientation is indicated. CH5 has its own coordinate system because the whole chamber is rotated 45^{o} for acceptance reasons.

The chambers CH1 and CH2 are located inside the magnet.

The anode wires are made from tungsten and have a diameter of 20 μm. The cathode planes are mylar planes with a thin layer of graphite damped on. The graphite layers are only a few μm thick.

A chamber consists of alternating wire- and high voltage cathode-planes and is filled with a gas mixture. It is closed by a mylar window in each end.

It should be noted that CH3 is organized as six separate units which can be moved independently, each with its own gas supply.

CH1-CH3 are filled with the following gas mixture:

Gas	Ar	Isobutan^{+}	Freon 13B1*	Methylalcohol†
Percentage	81.4%	15.0%	0.6%	3.0%

+ Chemical formula C_4H_{10}

* Chemical formula CF_3Br

† Chemical formula $CH_2(OCH_3)_2$

CH4-CH6 are filled roughly as follows:

Gas	Ar	CO_2	Freon 13B1*
Percentage	~75%	~24.5%	~0.5%

As an example, fig. 4.11 sketches the composition of CH1.

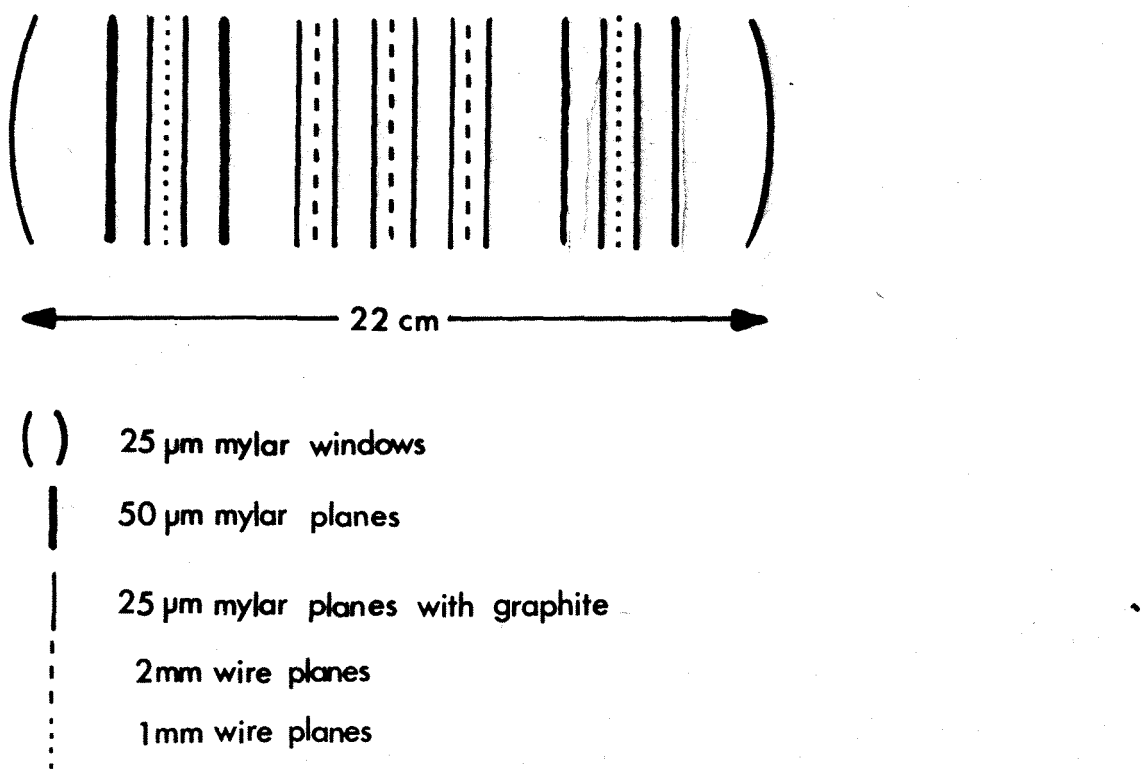

Fig. 4.11
The Composition of Chamber CH1.

In table 4.2 are also given the approximate z-position of the chambers, and their approximate wired area. It should be noted, however, that some of the u- and v-planes have dead areas in the corners because of the wiring, as indicated in fig. 4.12.

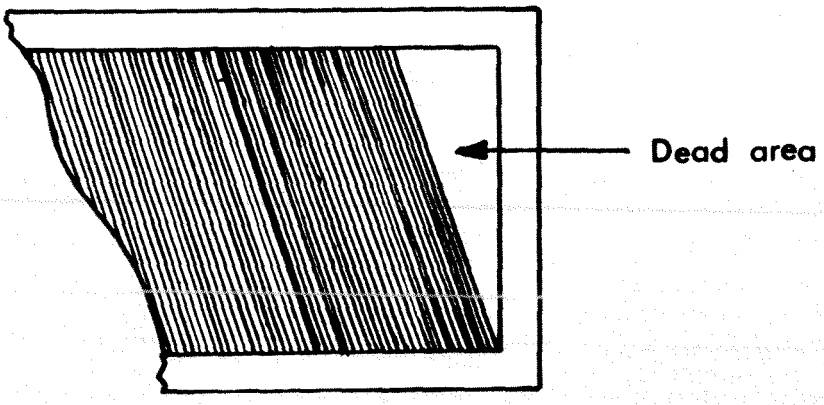

Fig. 4.12
MWPC-plane with dead area.

The total number of wires in the six chambers is approximately 20 000. All the wires are read out for each trigger.

Table 4.2 Properties of MWPCs (see the text).

Chamber	Plane	Projection	Spacing (mm)	Approximate Area (m^2)	Approximate z(cm)
CH1	1	x	1	0.96×0.26	-35.
	2	u	2		
	3	y	2		
	4	v	2		
	5	x	1		
CH2	6	x	1	1.09×0.30	0.
	7	v	2		
	8	u	2		
CH3	9	x	2	2.05×0.58	115.
	10	u	2		
	11	v	2		
	12	y	2		
	13	x	2		
	14	x	2		
CH4	15	u	2	2.35×2.35	695.
	16	y	2 †		
	17	v	2		
	18	x	2		
CH5	19	x	2	2.35×2.35	1135.
	20	u *	2 †		
	21	y	2		
	22	v	2		
CH6	23	x	2	2.35×2.35	695.
	24	u	2 †		
	25	y	2		
	26	v	2		

* The local coordinate system of CH5 is rotated -45^{o} with respect to the lab system.

† It should be noted that in some of the planes of CH4-6, the wires are read out two by two because of lack of read-out electronics. This corresponds to a wire-spacing of 4 mm.

Often more than one wire fires when a charged particle crosses a wire plane. Instead of using one word for each fired wire when writing such events onto tape, groups of adjacent fired wires are treated together. Only the so-called cluster centre (in units of half wires) and cluster size (number of fired wires) are written onto tape.

The transformation from single wire digitisings to cluster position and cluster size is performed on line by a device called the cluster and renormalization box. The box is indicated in fig. 4.18 of section 4.9.

4.6 The Threshold Cerenkov Counters

In order to identify the outgoing particles, the experiment uses four threshold Cerenkov counters [52, 53], denoted C1-C4 in fig. 4.1.

They are large boxes filled with gas at atmospheric pressure and equipped with mirrors and photo multipliers to detect the Cerenkov light.

The threshold velocity for light emission is given by the refractive index, n, of the gas as

$$\beta_c = \frac{1}{n} \tag{4.3}$$

corresponding to a threshold value of the relativistic mass increase factor, γ, of

$$\gamma_c = \sqrt{\frac{n^2}{n^2 - 1}} \tag{4.4}$$

Since for a given momentum the particle velocity is given by its mass, this means that by using different gases in the threshold Cerenkov counters, one may identify the final state particles of an elastic scattering process.

The mean number, m , of photo-electrons caused by a particle with relativistic mass increase factor γ arriving at the first dynode of a photo multiplier in a Cerenkov counter, is given by [54]

$$m = L\, N_o \frac{\frac{1}{\gamma_c^2} - \frac{1}{\gamma^2}}{1 - \frac{1}{\gamma^2}} \tag{4.5}$$

Here L is the length of the radiator and N_o is a constant characterizing the optical system and the photo multiplier.

The actual number of photo-electrons hitting the first dynode is Poisson

distributed with mean m, i.e. the probability of x photo-electrons arriving at the first dynode is

$$P(x) = \frac{e^{-m} m^x}{x!} \tag{4.6}$$

Thus the probabilities of 0 or 1 electron are

$$\begin{aligned} P(0) &= e^{-m} \\ P(1) &= m\, e^{-m} \end{aligned} \tag{4.7}$$

Let us now assume that the probablity of not counting a single photo-electron is η and that a particle with ≥ 2 photo-electrons is counted with 100% efficiency. Then the overall counting efficiency of the counter is given by

$$\varepsilon = 1 - P(0) - \eta\, P(1) = 1 - e^{-m}(1 + \eta m) \tag{4.8}$$

This formula gives rise to the curves of fig. 4.13 which show the efficiency ε as a function of γ for different values of γ_c.

To obtain these curves, values of $L = 300$ cm, $N_o = 82.8$ and $\eta = 0.1$ are used, and $1/\gamma^2$ is assumed $\ll 1$ [54].

One should note the slow rise of the efficiency for the higher values of γ_c.

Table 4.3 Properties of the Cerenkov Counters [52, 53]

Fillings at 20 GeV/c

		Volume (m^3)	Length along z (m)	Gas	Refr.ind. $(n-1)\cdot 10^6$	Rad.length (m)	Thresholds (GeV/c) π	K	p
Fast arm	C1	39	4.6	N_2	269	304	6.0	21.1	40.5
	C2	45	3.6	Freon 12*	1013	48	3.1	10.9	20.9
Slow arm	C3	17	1.6	Freon 12*	1013	48	3.1	10.9	20.9
	C4	31	2.5	CO_2	405	202	4.9	17.2	33.0

* Chemical formula is CCl_2F_2

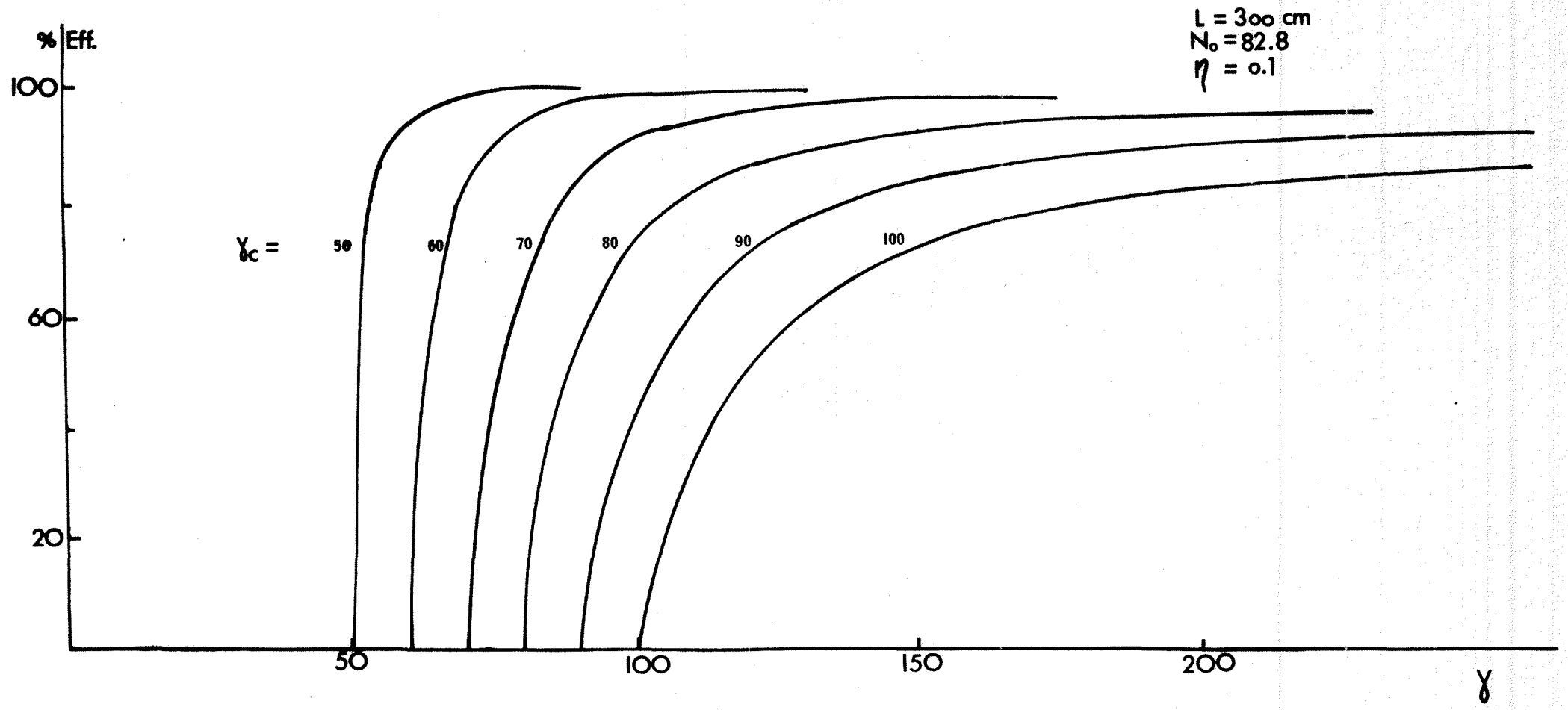

Fig. 4.13

Cerenkov counter efficiencies for different values of γ_c as functions of γ (from [54]).

Table 4.4 shows the momentum ranges in the two arms which are accepted in 20 GeV/c elastic scattering.

Table 4.4 Accepted Momentum Ranges (GeV/c) in 20 GeV/c elastic Scattering.

(from [52])

Momentum Ranges, GeV/c	
Left Arm (C1-C2)	Right Arm (C3-C4)
9 - 17	3 - 11

From the threshold momenta of table 4.3 and the momentum ranges of table 4.4, we can immediately write down table 4.5. In this table "1" means Cerenkov has fired and "0" means no signal.

Table 4.5 Particle Identification at 20 GeV/c (See the text).

Fast Arm	Slow Arm	Meson Momentum (GeV/c)	C1	C2	C3	C4
p	p		0	0	0	0
π	p	$p_\pi \geq 6.0$	1	1	0	0
K	p	$p_K \leq 10.9$	0	0	0	0
K	p	$p_K \geq 10.9$	0	1	0	0
p	π	$3.1 \leq p_\pi \leq 4.9$	0	0	1	0
p	π	$p_\pi \geq 4.9$	0	0	1	1
p	K	$p_K \leq 10.9$	0	0	0	0
p	K	$p_K \geq 10.9$	0	0	1	0

It should be noted that under elastic data-taking at 20 GeV/c the matrices (see section 4.8) are set to accept meson-proton events only if the meson goes into the fast (left) arm. Thus the only possibility of misidentification

is to mix a K event (with $p_K \leq 10.9$ GeV/c) with a p event. This ambiguity will, however, be solved when CEDAR information is taken into account. At higher incoming momenta other fillings are used.

In these cases the particle identification will not always be as simple as at 20 GeV/c. Generally it will not suffice to see which counters have given signals - in addition the pulse heights have to be studied in order to distinguish π from K.

4.7 The Downstream Hodoscopes

The experiment uses three hodoscopes for triggering purposes. One is placed immediately downstream of chamber CH3 (called HOD in fig. 4.1). The two others are situated just behind chambers CH5 and CH6, respectively. They are called PR.HOD1 and PR.HOD2 in fig. 4.1.

A hodoscope is a collection of scintillation counters, eventually with light guides, and equipped with photo multipliers.

4.7.1 The H1H2 Hodoscope

We will refer to the hodoscope immediately downstream of CH3 as H1H2.
H1 is the part of the hodoscope to the left of the beam when viewed downstream, and H2 is the right part. Both consist of two planes of plastic scintillators 1 cm thick. From each scintillator the light is mediated to a photo multiplier by a light guide.

The scintillators in the upstream planes are ringshaped, whereas the downstream elements are wedgeshaped. The elements of both planes are drawn in fig. 4.14.

This arrangement makes it simple to achieve information on coplanarity (wedge-wedge correlations) and opening angle (ring-ring correlations) at the trigger level (see section 4.8 for more details).

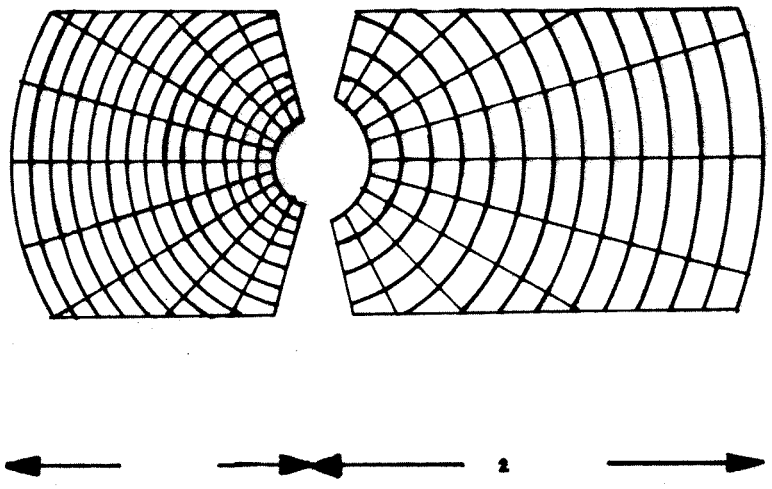

Fig. 4.14
Arrangement of scintillators in H1H2.

4.7.2 The Prompt Hodoscopes

The prompt hodoscopes are collections of rectangular scintillators. The elements occur in three different sizes: 30×30 cm^2, 30×15 cm^2 and 15×15 cm^2. They are arranged in "rings" with the smallest elements closest to the beam as shown in fig. 4.15.

Each scintillator is equipped with a photo multiplier which is mounted immediately behind the element and sees the light directly without use of solid light guides.

This fact combined with the small dimensions of the elements minimizes the time jitter of the signals, thus making accurate time of flight measurements possible. With a 30×30 cm^2 element and the photo multiplier 30 cm behind the middle of the element, an accuracy of the time of flight measurements of 520 ps is achieved [55].

Thus the prompt hodoscopes are well fitted to participate in the trigger mechanism of a high intensity beam experiment as WA7.

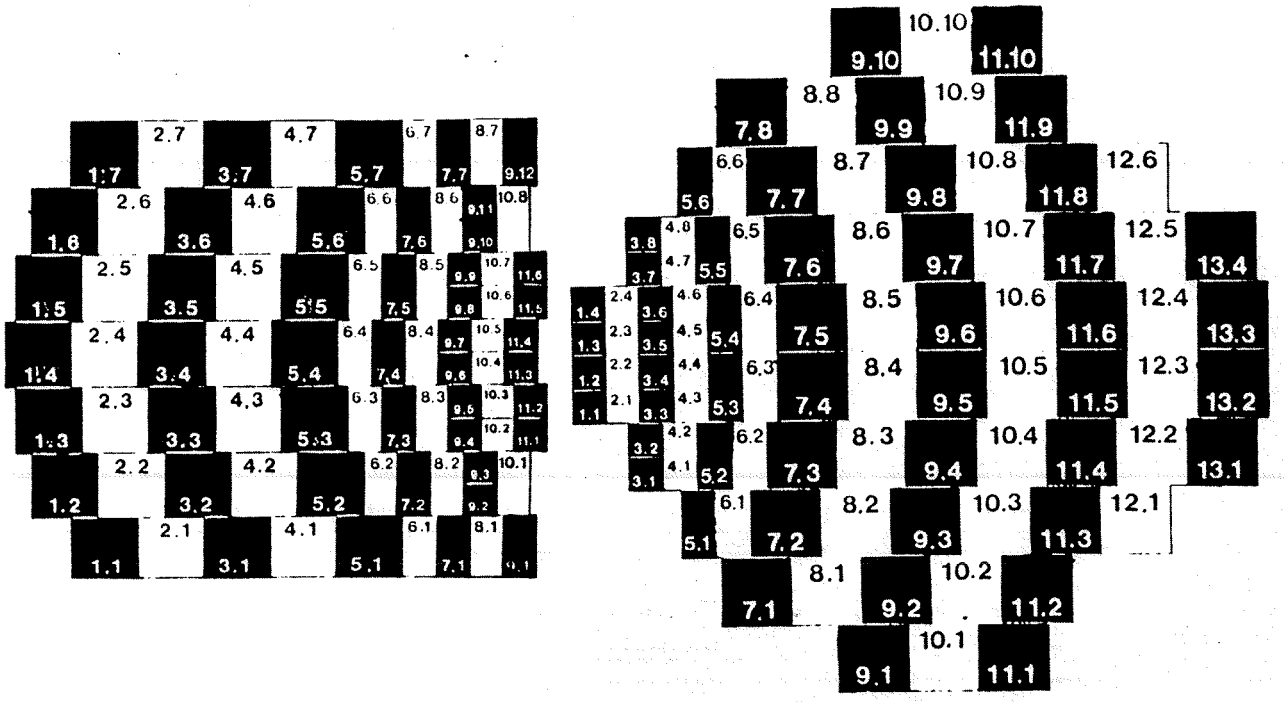

Fig. 4.15

The Prompt Hodoscopes viewed upstream.

The figure does not correctly reproduce the distance between the two hodoscopes.

4.8 The Trigger Logic

The fast logic and the data acquisition system are based on standard CAMAC.

The data have to satisfy a number of constraints before they are accepted as possible elastic event candidates. The requirements are:

(1) The reaction should be due to a beam particle, and there should be no particles going into the magnet walls.

(2) There should be less than a maximum number of particles in each arm.

(3) The straight line part of the tracks should point back towards the target region.

(4) The event should be coplanar within limits defined by Monte Carlo studies.

(5) The opening angle should be within limits defined by Monte Carlo studies.

(6) One of the outgoing particles should be a proton, the other one a pion, kaon or proton.

The necessary tests to see whether the above requirements are fulfilled, are carried out by the fast electronics. The trigger logic is schematically drawn in fig. 4.16. The logic may naturally be divided into two levels. In the second level the constraints are calculated more accurate than in the first one.

In the first level point (1) is taken care of by requiring no hits in the beam veto counter and no hits in the veto counters inside the magnet. Also crude tests on the conditions (3), (4) and (5) are performed at the first level of the trigger logic.

Two fast programmable or's (OR1-OR2 in fig. 4.16) make opening angle tests by comparing the upper (downer) half rings of PR1 to downer (upper) half rings of PR2.

Two of the four fast matrices (FM1-FM4 in fig. 4.16) perform tests on the

straight lines by comparing the rings of PR1 (PR2) to the rings of H1R (H2R). The third fast matrix makes an opening angle test by comparing the rings of H1R to those of H2R. The fourth fast matrix compares the wedges of H1W and H2W giving a rough test of coplanarity.

If all these tests are fulfilled, a fast strobe is generated which opens the registers and enables the RMH-modules for storing of MWPC-data. Thereafter more refined tests on the conditions (4) and (5) are performed by the second level trigger logic, which also checks if conditions (2) and (6) are fulfilled.

Point (2) is taken care of by the majority logic. It only accepts the trigger as a possible event candidate if the number of hits in H1, H2, PR1 and PR2, respectively, are less than given maximum numbers.

Because of the background, it is a finite probability of observing more particle tracks than those from the elastic-like event. Therefore one generally uses higher maximum numbers than one. Typical maximum numbers used for elastic scattering at 20 GeV/c, are

$$\leq 2 \text{ in H1}, \leq 2 \text{ in H2}, \leq 2 \text{ in PR1} \quad \text{and} \quad \leq 1 \text{ in PR2} \qquad (4.9)$$

Condition (6) is taken care of by putting Cerenkov and CEDAR signals into the trigger as indicated in fig. 4.16.

More refined tests on the event geometry are performed by two slow 48×48 matrices (called SM1-SM2 in fig. 4.16). They compare the upper (downer) part of PR1 to the downer (upper) part of PR2 on an element to element basis.

While these second level tests are performed (a few hundred nano-seconds) the formation of a new fast strobe is inhibited by the strobe inhibit flip-flop.

If the event is accepted also by the second level logic, an event signal is formed. This signal opens the gates for the ADC's and, in case of no fast processor (see section 4.10), sends an interrupt to the on-line computer which

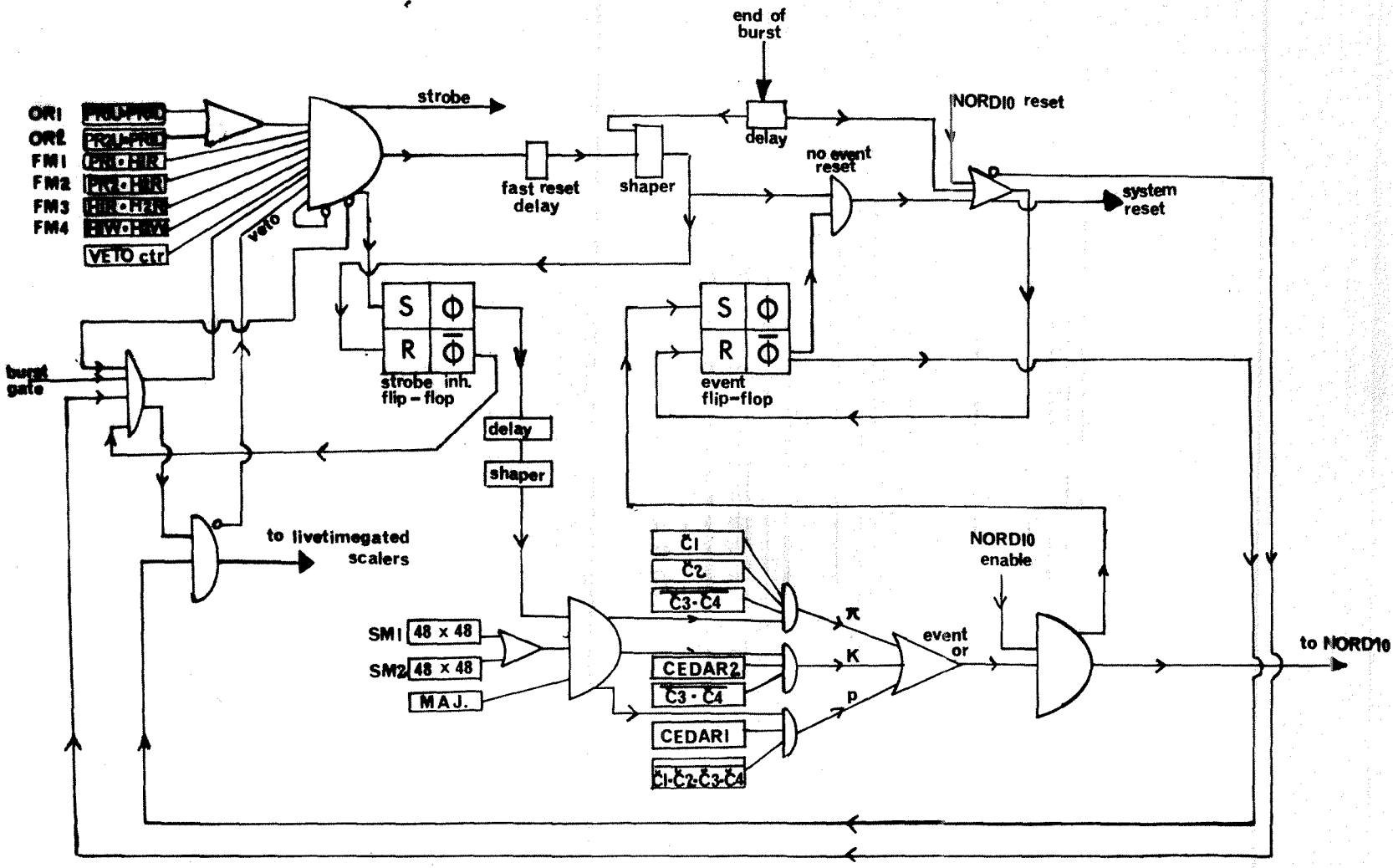

Fig. 4.16

The fast trigger logic (see the text).

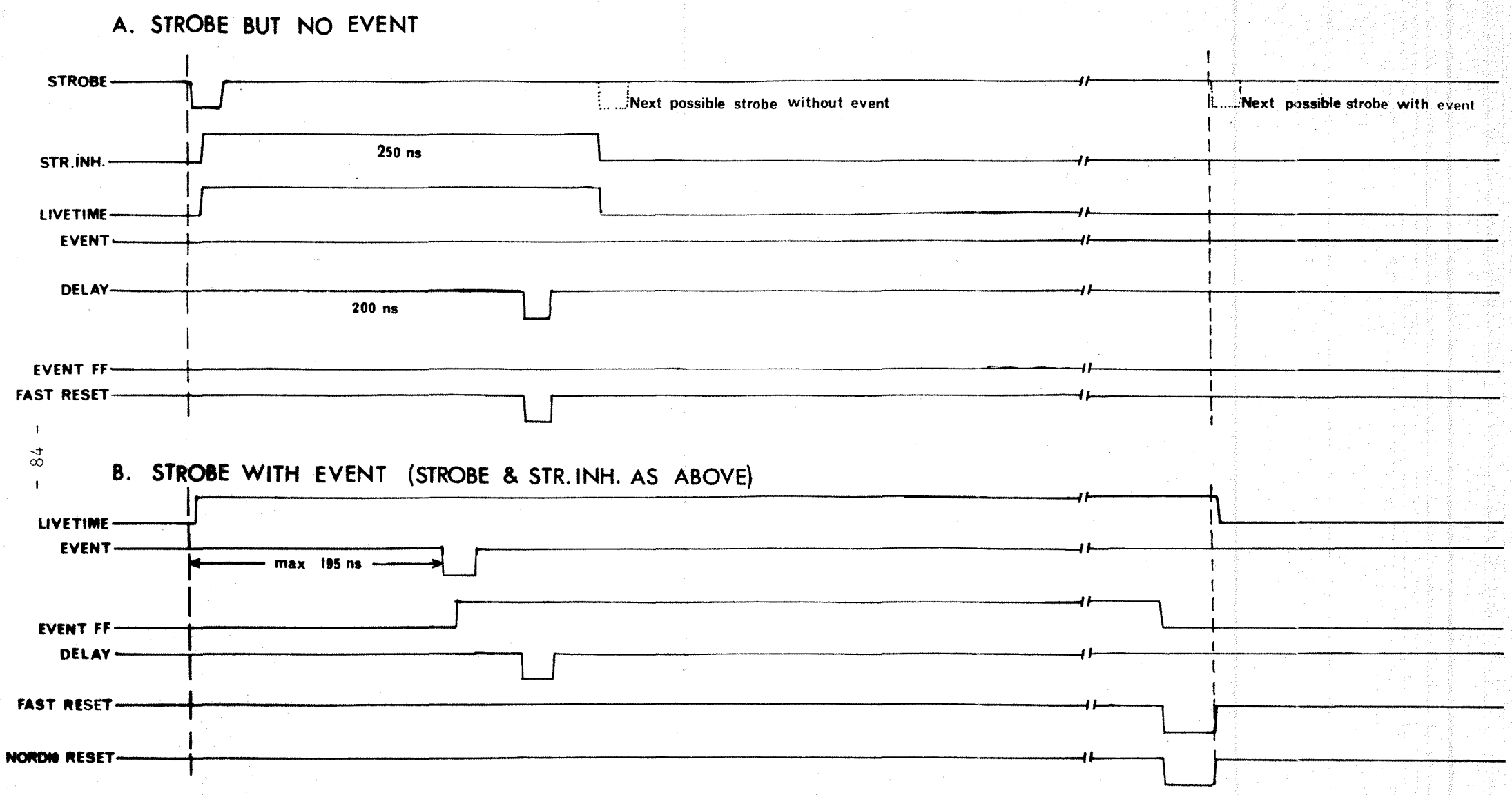

Fig. 4.17

Timing diagram of the fast logic.

reads the event and writes it onto magnetic tape.

During this time (a few milli-seconds) the formation of a new strobe is inhibited by the event flip-flop.

In fig. 4.16 is also indicated the life time logic which measures the real time of data-taking, i.e. the time when the formation of a strobe is not inhibited.

Fig. 4.17 gives the time diagram for the logic.

4.9 Data-Acquisition and Monitoring

As mentioned earlier, when an event candidate is accepted by the fast logic, the registers and RMH-modules are read out via CAMAC by a NORD10 minicomputer and the event is written onto magnetic tape. Peripheral equipment of the NORD10 includes a disc-unit, two magnetic tape units, one writing terminal and two TV-screen terminals.

The program which controls the data-taking is called DAS (Data Acquistion System).

Through DAS the user can interfere with the data-taking. Besides starting and stopping runs, he can set the slow and fast matrices and choose different operational modes of the microprocessors (see the next section), and different modes of monitoring.

The data-acquisition logic is schematically shown in fig. 4.18.

The computer reads about 250 CAMAC words per accepted trigger from ADCs, registers and scalers. In addition comes one word for each cluster. Typically $\sim$ 100 clusters are recorded per event.

A typical time for the recording of one event is 2 ms. With about 150 events per second this gives 30% as a rough estimate of the dead-time.

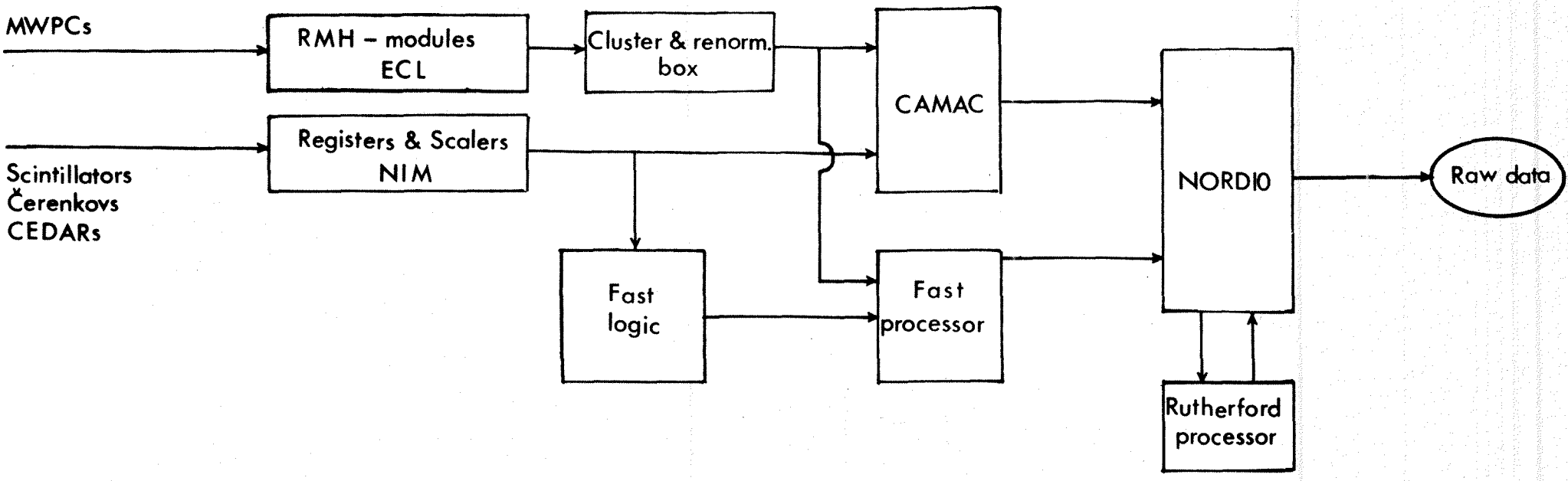

Fig. 4.18

The Data-Taking Logic.

In addition to controlling the data acquisition, DAS also serves as a monitoring device. That is, DAS can provide the user with information on the status of the apparatus during a run, such as how the chamber read-out system works and what the detector efficiencies are like.

Much information can be obtained in the form of displays on a TV-screen terminal. Examples of such displays are histograms over fired wires in the MWPC-planes, and "event pattern" pictures, i.e. single trigger displays of fired elements of the four hodoscopes, fired wires in the MWPC-planes and fired mirrors in the Cerenkovs. Two examples of such event pattern displays are given in fig. 4.19 (a) and (b)*. They refer to the same elastic π-event.

---

* The displays shown in fig. 4.19 are produced off-line, but the displays achieved on-line by DAS look quite similar.

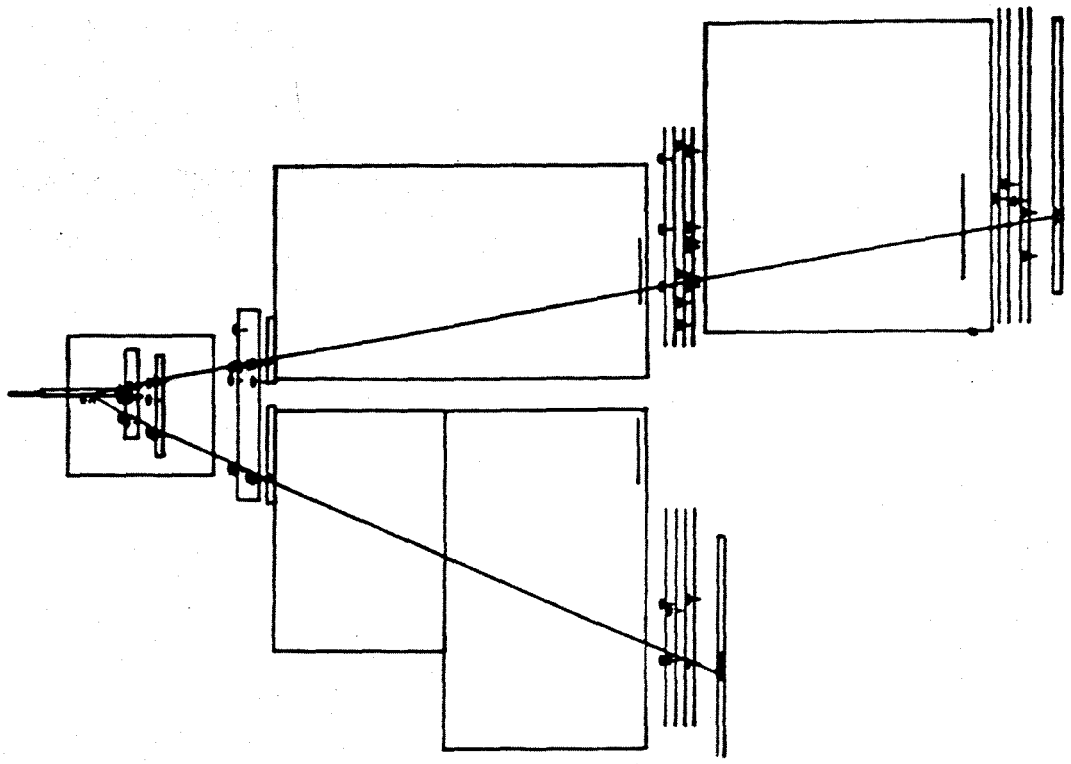

(a)

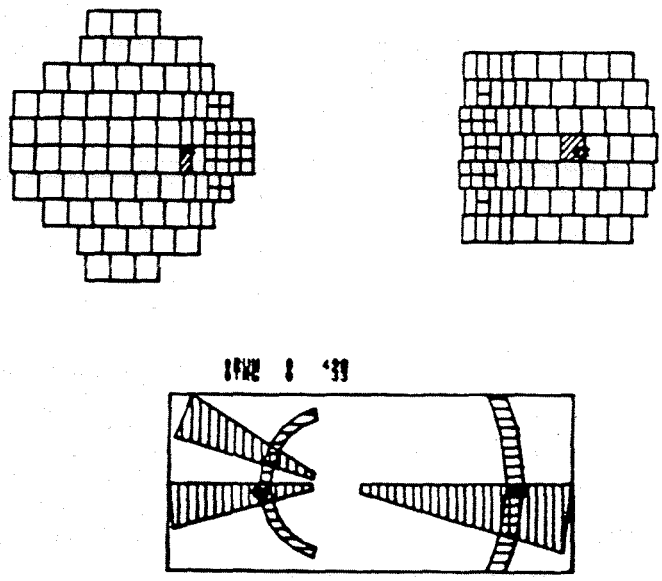

(b)

Fig.4.19 "Event pattern" displays.
(a) The event in horizontal projection.
(b) Fired elements in the hodoscopes.

4.10 The Micro - Processors

To cope with the highest intensities, the on-line data-taking system is designed for using two micro-processors. When this is written, none of them has been into operation.

One is a fast, hard-wired processor built by a CERN-group [56]. It is intended to use MWPC-information to reconstruct straight lines outside the magnetic field and perform certain kinematical tests. This will allow for more stringent trigger criteria than is possible with the fast electronics described in section 4.8. The fast processor will thus serve as part of the trigger logic, representing a third logical level.

The other one, the Rutherford processor [57], is programmable and therefore slower. It is intended to be used to process the events which NORD10 has read before they eventually are written onto tape, thus reducing the amount of data still more. This will be done in the interval between the bursts.

4.11 Iron Calorimeter and Mu-Trigger

Behind each prompt hodoscope is mounted a roughly 3 m long unit consisting of 200×200×10 cm^3 iron plates sandwiched with scintillation counter planes and drift chamber planes [58]. Fig. 4.20 shows a scintillation counter plane. At the time of writing, the calorimeter has not been into operation.

By integrating the pulses from the scintillators, one gets a measure of the energy deposited in the calorimeter. It may thus be used for triggering purposes. At the higher energies it is expected that the use of the calorimeter in elastic triggering will reduce the trigger rate significantly. The reason is that by far the largest part pf the background trigger rate is caused by electrons and low momentum mesons.

Since the iron effectively absorbs hadrons, the calorimeter may also be used

for muon triggering purposes. It is intended to make use of this to study the production of heavy mesons which decay into muon pairs. We will return to this point in chapter 6.

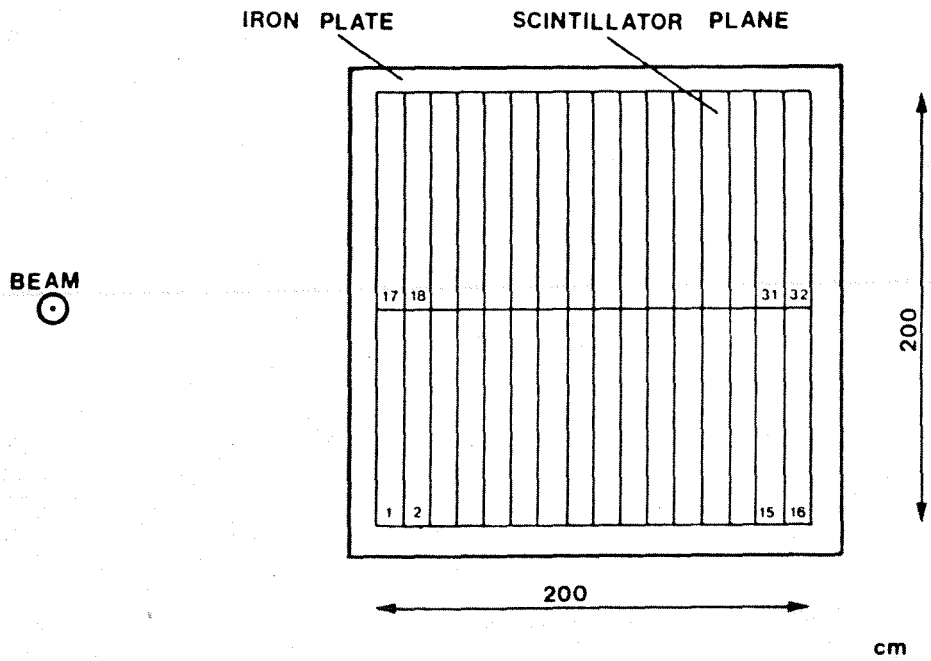

Fig. 4.20
A Scintillation counter plane in the calorimeter (from [58]).

CHAPTER 5 OFF-LINE SOFTWARE - DATA ANALYSIS

5.1 Introduction

Large computer programs are used to decode the information on the raw data tapes written by the on-line computer, and to process this information. These programs constitute the analysis chain. The ultimate goal of the analysis is to compute the cross sections of the reactions studied.

In order to compute the cross section of a reaction, detailed knowledge of the geometrical acceptance is needed. This is calculated by the Monte Carlo programme which is described in chapter 6 together with some of its applications.

5.2 Soft-Ware Organization

Most of the programme packages of the analysis chain are kept on PATCHY Master files, or PAM-files. PATCHY is a flexible system for maintenance and evolution of the programs [59].

In addition to the programs written by the group, supporting material of different kinds exists. This includes a data-file containing all the parameters necessary to describe the experiment, hereafter called GENDATA, a library containing frequently used routines, hereafter called UTYLIB, the CERN programme library [60], and SUMX [61].

UTYLIB contains among other things the magnetic field routines [62] and a package of input/output routines. These input/output routines are written with the scope of being able to cope with different machines and different tape formates [63]. This makes it simpler to perform the production runs at different laboratories.

At the time of writing, the analysis is performed at CERN's IBM 370/168 and the IBM 360/195 of UCL in London (at the Rutherford High Energy Labora-

tory). In addition it is planned to run production on the IBM 370/165 of NBI in Copenhagen and the CDC CYBER 74 in Oslo.

When an external laboratory is going to make a production run, it is provided with copies of the raw data tapes. High density copies of the original raw data are kept at CERN.

An automatic book-keeping system at CERN [64] keeps track of what happens to the data from the different runs.

5.3 The Analysis Chain

The analysis chain may naturally be divided into three parts:

(i) Pattern recognition and preliminary analysis of accepted event candidates. This programme package will be referred to as PROG1 in the following.

(ii) Further analysis of accepted event candidates, including a chi-squared fit with the application of vertex- and kinematical constraints. This package will be referred to as PROG2 in what follows.

(iii) A programme package mainly based on SUMX for detailed studies of events and event candidates, and final cross section computations. This programme package, which will (not surprisingly) be referred to as PROG3 in the following, also includes a programme for off-line display of events.

PROG1 produces a data summary tape, DST1, containing parts of the raw data and information on the accepted event candidates.

PROG2 uses DST1 as input and produces a new data summary tape, DST2, which contains all the information of DST1 plus new information on the accepted event candidates.

PROG3 may use either DST1 or DST2 as input. The analysis chain is schematically shown in fig. 5.1.

It should be noted that PROG1 and PROG2 are usually run together without producing a DST1, as indicated by the dotted line in fig. 5.1.

For reasons explained in the preface to this thesis, the PROG2 package is described in considerably more detail than the two other programme packages.

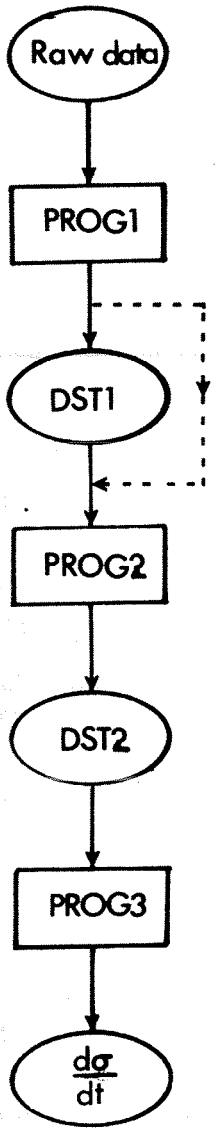

Fig. 5.1
The Analysis Chain (see the text).

5.4 The PROG1 Programme Package

5.4.1 Short Description of the Raw Data Format.

A raw data tape consists of one or more files, each file consisting of data from one run. A run is ended when the experimental conditions are changed or when end of tape is reached.

A raw data file is divided into physical records, each consisting of 1890 16-bit words. The information contained in the physical records is organized as logical blocks of variable lengths. One logical block may extend from one physical record to another.

Two kinds of logical blocks exist on the raw data files: the standard event block and the burst scaler block.

The standard event blocks contain CAMAC readout, MWPC readout and fast processor readout for each trigger.

The burst scaler blocks are written one at each end of burst and contain information on the ionization chamber, certain beam hodoscope elements, and statistical information such as the accumulated number of events.

Detailed discriptions of the different blocks can be found in [65].

5.4.2 The Structure of the PROG1 Program Package

The PROG1 package may naturally be divided into four stages. This is indicated in fig. 5.2 which shows a simplified flow chart of the package. In the first stage the control cards are read and analyzed. By means of these control cards the user may perform file handling like skipping certain files etc.

In addition tape reading initialization and file initialization is performed in this stage, as well as the reading of the parameters from the GENDATA file.

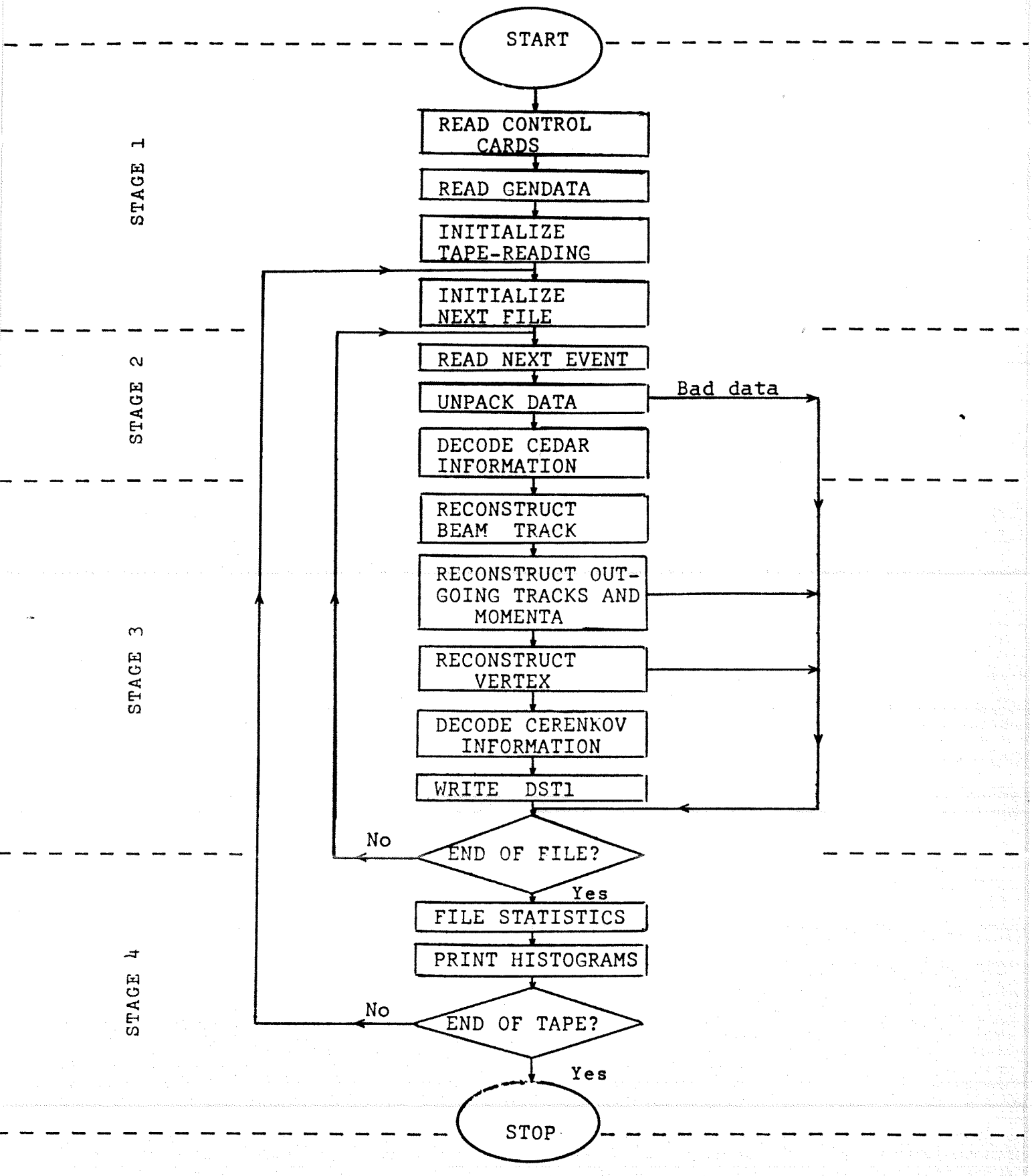

Fig.5.2 Simplified flow-chart of the PROG1 programme package.

In the second stage the raw data from one event are read, unpacked and stored in COMMON areas after conversion from 16-bit words to the appropriate word length.

In the third stage the pattern recognition is performed. The second and third stages are repeated once for each trigger until end of file is reached.

In the fourth stage different kinds of statistics are printed and written to the DST. This stage is executed once at the end of each file.

We now turn to a short description of the geometrical reconstruction of the events.

5.4.3 Basic Philosophy of the Pattern Recognition

The task of stage three of the PROG1 package is to reconstruct events from the MWPC-, CEDAR- and Cerenkov information.

The main problem is to reconstruct the outgoing tracks behind and inside the magnet from the MWPC information, and to associate correctly tracks in the two arms with each other to get the vertex. The procedure is basically the following.

Two clusters in a chamber define a point if they belong to planes with the wires in different inclinations. Two points belonging to different chambers behind the magnet define a straight line.

The chambers used to define straight lines in this way, the so called pivot chambers, are CH3 and CH5 in the left arm, and CH3 and CH6 in the right arm.

In order to see whether the straight line belongs to a track, the clusters inside a given "road" of ±0.8 cm along the track are counted. If the number of clusters is less than a given minimum number (11 in the left arm and 7 in the right one), the straight line is not accepted as belonging to a particle trajectory.

Next is demanded that the straight line piece should have an extension into the magnet. To check if that is the case, the straight line is extrapolated to all the planes of CH1 and CH2.

It is further assumed that if two clusters in two planes inside the magnet belong to the same track, their distances from the extrapolated straight line are proportional. The proportionality factors are given by the magnetic field and the z-positions of the planes.

Again the track candidate is accepted only if the number of clusters inside the magnet belonging to the track is larger than a given minimum number (4 for both arms).

The momentum calculation algorithm is a very crude and simple one. The magnetic field is assumed to be constant inside a box and zero outside. Thus the momentum can be calculated directly from the deflection of the track in CH1 compared to the straight line downstream of the magnet.

The next constraint to be fulfilled is that there should exist at least one track in each arm which together give a reasonable 2-prong vertex parameter. The 2-prong vertex parameter is the smallest distance between the two tracks.

The vertex reconstruction algorithm is based on simple geometrical considerations [66]. The magnetic field is assumed to have cylindrical symmetry around the vertical line through the magnet centre. According to this a track is assumed to be mirror symmetric about a vertical plane through the magnet centre perpendicular to the track.

With this assumption a 2-prong vertex is constructed from the outgoing tracks. If one or more beamtracks are successfully reconstructed, these are used to construct 3-prong vertices. Beamtracks giving 3-prong vertex parameters larger than a given maximum are not accepted.

The output from the vertex reconstruction is the vertex position $(x,y,z)_v$

and the track derivatives, $\left(\frac{dx}{dz}, \frac{dy}{dz}\right)_v$, at the vertex.

It should be noted that neither the momentum nor the vertex reconstruction algorithm makes use of a magnetic field map or equivalent magnetic field routines. This is done in order to make the programme fast.

Because of the crude approximations used, the PROG1 package is often not able to solve ambiguities where for example different straight lines seem to have the same extension into the magnetic field, or different tracks in one arm may be combined with a track in the other arm, all giving acceptable vertices etc.

The resolution of such ambiguities and the accurate calculation of the event parameters are the tasks of the PROG2 programme package.

5.5 The PROG2 Programme Package

The PROG2 programme package performs an iterative track fitting procedure. The track parameters are determined by a least squares fit which gives more accurate results than the PROG1 package, but which on the other hand uses considerably more time per sevent.

The time consumption is not a very serious problem, however, since only event candidates with correct charge combination* are processed by PROG2. Only a few percent of the event candidates written to DST1 have correct charge combination.

The vertex constraint is always applied, whereas the use of the kinematical constraints is optional. Under production runs the kinematical constraints are always used, though. Se section 5.5.5 for more details.

---

* The charge is determined by PROG1 from the direction of the x-bending in the magnet. With 20 GeV/c negative beam only events with a negative particle in the left arm and a positive one in the right arm are accepted. With positive beam one obviously demands a positive particle in each arm.

5.5.1 Chi-squared and the Method of Least Squares

We want to parametrize the m measurements a_i, $i = 1, \ldots, m$ with the m functions f_i, $i = 1, \ldots, m$, which are functions of the n ($< m$) parameters ξ_α, $\alpha = 1, \ldots, n$. In vector notation:

$$f = f(\xi) \tag{5.1}$$

with

$$f = \begin{pmatrix} f_1 \\ \vdots \\ f_m \end{pmatrix} \qquad \text{and} \qquad \xi = \begin{pmatrix} \xi_1 \\ \vdots \\ \xi_n \end{pmatrix}$$

We define the m residues d_i, $i = 1, \ldots, m$ by (again in vector notation as explained above):

$$d = a - f(\xi) \tag{5.2}$$

The matrix of derivatives, D, is defined by

$$D_{i\alpha} = \frac{\partial f_i}{\partial \xi_\alpha} \tag{5.3}$$

In general f does not depend linearly on ξ, but we may linearize it by setting

$$f(\xi + \Delta\xi) \approx f(\xi) + D\Delta\xi \tag{5.4}$$

We then define the weight matrix W as the inverse of the error matrix Σ:

$$W = \Sigma^{-1} \tag{5.5}$$

In the case where all the correlations between measurement errors are neglected, Σ is diagonal with the m squared measurement errors σ_i^2, $i = 1, \ldots, m$ along the diagonal.

The problem is now to find the "best possible" values of the parameters ξ. When applying the method of least squares, the "best possible" values of the parameters are taken to be those which minimize the sum of squares

$$s^2 = d^T W d \tag{5.6}$$

d^T denotes the transposed of d, i.e.

$$d^T = (d_1, \ldots, d_m) \tag{5.7}$$

When such a problem is to be solved on a computer, it is usual to work with approximate values for the variables ξ and accordingly approximate values of the residues d. Demanding s^2 to be at a minimum leads to equations for the corrections $\Delta\xi$ to ξ the following way.

Written in terms of $\Delta\xi$, the component form of eq. (5.6) reads

$$s^2(\xi + \Delta\xi) = \sum_{i,k,\alpha} (x_i - f_i(\xi) - \frac{\partial f_i}{\partial \xi_\alpha} \Delta\xi_\alpha) W_{ik} (x_k - f_k(\xi) - \frac{\partial f_k}{\partial \xi_\alpha} \Delta\xi_\alpha) \tag{5.8}$$

From the constraint of s^2 to be at a minimum we get the n equations

$$\frac{\partial s^2}{\partial \Delta\xi_\beta} = 0, \quad \beta = 1, \ldots, n \tag{5.9}$$

On component form these equations may be written

$$\sum_{i,k,\alpha} D_{i\beta} W_{ik} D_{k\alpha} \Delta\xi_\alpha = \sum_{i,k} D_{i\beta} W_{ik} d_k \tag{5.10}$$

or, in matrix notation:

$$D^T W D \, \Delta\xi = D^T W d \tag{5.11}$$

If W is diagonal, we have

$$W_{ij} = w_i^2 \delta_{ij}, \tag{5.12}$$

$w_i = \frac{1}{\sigma_i}$ being the inverse of the standard deviation of the measurement error on a_i.

With

$$D_{i\alpha} = w_i D_{i\alpha}$$

and (5.13)

$$\delta_i = w_i d_i$$

we can then write (5.11) as

$$D^T D \, \Delta\xi = D^T \delta \tag{5.14}$$

We will return to the problem of non-diagonal error-matrix, i.e. the general solution of (5.11), in section 5.5.6.

Equation (5.14) is clearly solvable as long as the matrix $D^T D$ is invertible, with solutions

$$\Delta\xi = (D^T D)^{-1} D^T \delta \tag{5.15}$$

"The best" values of the parameters are accordingly given by

$$\xi \to \xi + \Delta\xi$$

with $\Delta\xi$ as in (5.15). The matrix

$$\varepsilon = (D^T D)^{-1} \tag{5.16}$$

is the error matrix (or covariance matrix) of the fitted variables ξ. When f is not a linear function of ξ, one generally has to iterate. The minimum value of s^2, usually arrived at after 3-6 iterations in our applications, is called chi-squared, or χ^2, i.e.

$$\chi^2 = \min s^2 = \min(\delta^T \delta) \tag{5.17}$$

It can be shown that if the measurement errors on a_i, $i = 1, \ldots, m$ follow Gaussian distributions, χ^2 is chi-squared distributed with

$$\nu = m - n \tag{5.18}$$

degrees of freedom.

A schematic representation of the iterative least squares fitting procedure is given in fig. 5.3.

Application in the PROG2 programme package

In the PROG2 package M = 29 maximum, and the 29 measured quantities are:

$a_1, \ldots, a_8$: cluster centre positions in the 8 planes inside the magnet for the first outgoing track (left arm).

$a_9, \ldots, a_{12}$: $x, y, \frac{dx}{dz}, \frac{dy}{dz}$ in the reference plane at z = 400 cm for the left arm track.

$a_{13}, \ldots, a_{24}$: as $a_1, \ldots, a_{12}$, but for the right arm outgoing track.

$a_{25}, \ldots, a_{28}$: $x, y, \frac{dx}{dz}, \frac{dy}{dz}$ in the reference plane at z = - 600 cm for the beam track†.

a_{29} : the magnitude of the beam track momentum *.

As the MWPC planes are not 100% effective, the number of clusters inside the magnet per outgoing track is allowed to vary between 8 and 4.

Thus m varies between 21 and 29.

In PROG2 n has the value 12 and the 12 parameters to be fitted are:

$\xi_1, \ldots, \xi_3$: x,y,z of the vertex

$\xi_4, \ldots, \xi_6$: $\frac{dx}{dz}, \frac{dy}{dz}, \frac{c}{p}$ at vertx for the left arm outgoing particle (c = speed of light, p is the momentum).

$\xi_7, \ldots, \xi_9$: as above, but for the right arm particle

$\xi_{10}, \ldots, \xi_{12}$: the same for the beam track.

Accordingly the number of degrees of freedom, ν, varies between 9 and 17.

---

† See the footnote of table 5.2, page 114.

* The magnitude of the beam momentum is treated as a measured quantity with the nominal beam momentum as the measurement result, and with the beam line momentum resolution ($\frac{\Delta p}{p} \simeq 1\%$) as measurement uncertainty.

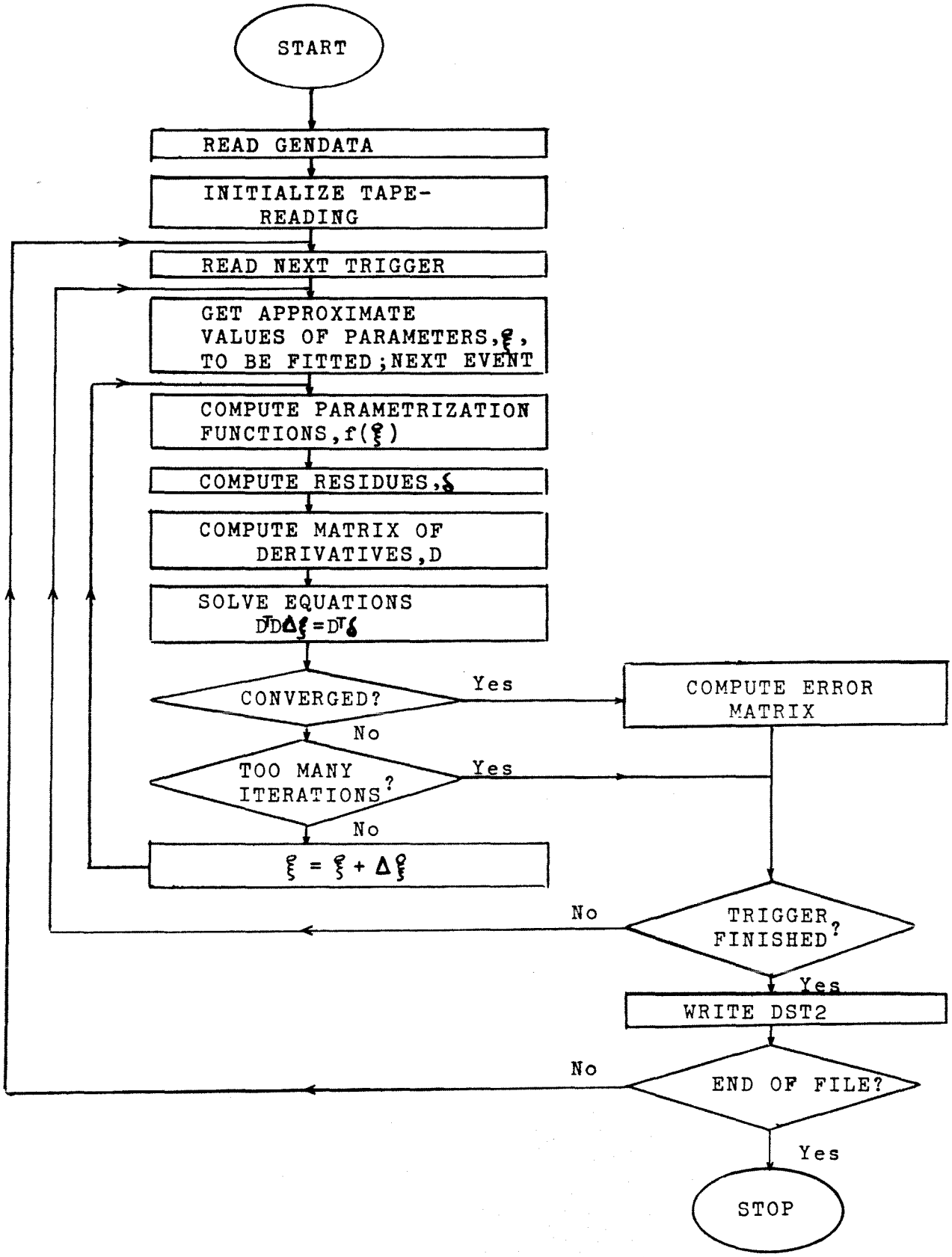

Fig.5.3 General structure of the PROG2 programme package without kinematical constraints (see the text).

The vertex constraint is simply implied by for each iteration letting the beam track end and the outgoing tracks start at the same point (ξ_1, ξ_2, ξ_3). Up to now we have not mentioned the problem of determining the parametrisation functions $f(\xi)$. To get these functions the original version of the PROG2 package used a quintic spline method [67,68]. The current version of PROG2, however, uses a different method based on familiar Runge Kutta integration [69]. We will shortly describe both methods.

5.5.2 The Quintic Spline Fit

The basic idea behind the quintic spline method [67], is to fit measured points with a "smooth" curve. In the quintic spline model of a track the "smooth" curve is defined as a curve which is consistent with the equation of motion of a charged particle in a magnetic field, and which is continuous down to (included) the fourth derivative. I.e. firstly the fifth derivative of the track in the quintic spline model is discontinuous.

From the equations of motion

$$\frac{d\vec{p}}{dt} = q\,\vec{v} \times \vec{B} \tag{5.19}$$

where $\vec{p}$ is the particle momentum, q the charge, $\vec{v}$ the speed and $\vec{B}$ the magnetic field, we get after some algebraic manupulations.

$$\begin{aligned} X'' \equiv px'' &= q\sqrt{1 + x'^2 + y'^2}\,(x'y'B_x - (1 + x'^2)\cdot B_y + y'B_z) \\ Y'' \equiv py'' &= q\sqrt{1 + x'^2 + y'^2}\,((1 + y'^2)\cdot B_x - x'y'B_y - x'B_z) \end{aligned} \tag{5.20}$$

The primes indicate differentiation with respect to z, for example $y'' = \frac{d^2y}{dz^2}$.

With the notation introduced in the previous section we can then write for the x-coordinates along the (left arm, say) track:

$$x_i \approx \xi_1 + (z_i - \xi_3)\xi_4 + \xi_6 X_i \tag{5.21}$$

Here z_i denotes the z-position of the plane in which x_i is measured, and similarly $X_i = X(z_i)$.

For the directions $x' = \frac{dx}{dz}$ along the track we have

$$x_i' \approx \xi_4 + \xi_6 X_i' \tag{5.22}$$

Similarly we have for y and y' :

$$\begin{aligned} y_i &\approx \xi_2 + (z_i - \xi_3)\xi_5 + \xi_6 Y_i \\ y_i' &\approx \xi_5 + \xi_6 Y_i' \end{aligned} \tag{5.23}$$

The functions X'' and Y'' are integrated twice following the method of [67].

When the measured coordinate, a_i, is x,y,x' or y', the corresponding f is simply $f_i \approx x_i$, y_i, x_i' or y_i'. If, on the other hand, a_i is a measured u or v coordinate, the f is given by the appropriate rotation

$$f_i = x_i \cos\theta_i + y_i \sin\theta_i \tag{5.24}$$

The matrix of derivatives, D, as defined in (5.3), is computed from eqs. (5.21-5.23). The only derivatives deserving a comment are those with respect to ξ_3.

Let us write (5.21) as

$$x = \xi_1 + (z - \xi_3)\xi_4 + \xi_6 \int_{\xi_3}^{z} dz_2 \int_{\xi_3}^{z_2} dz_1 \, X''(z_1)$$

Changing the order of integration, we obtain

$$x = \xi_1 + (z - \xi_3)\xi_4 + \xi_6 \int_{\xi_3}^{z} (z - z_1) \, X''(z_1) dz_1 \tag{5.25}$$

Similarly

$$x' = \xi_4 + \xi_6 \int_{\xi_3}^{z} X''(z_1) dz_1 \tag{5.26}$$

From (5.25) and (5.26) we get the derivatives:

$$\frac{\partial x_i}{\partial \xi_3} = -\xi_4 - (z_i - \xi_3)\xi_6 X''(\xi_3)$$

$$\frac{\partial x_i'}{\partial \xi_3} = -\xi_6 X''(\xi_3) \qquad (5.27)$$

We can then write down table 5.1 for the derivatives when f_i equals x_i, y_i, x_i' and y_i' (left arm, say).

Table 5.1 Derivatives $\frac{\partial f_i}{\partial \xi_\alpha}$ for $f_i = x_i, x_i', y_i, y_i'$ (left arm).

$\partial f_i / \partial$ \ f_i	ξ_1	ξ_2	ξ_3	ξ_4	ξ_5	ξ_6
x_i	1	0	$-\xi_4 - (z_i - \xi_3)\xi_6 X''(\xi_3)$	$z_i - \xi_3$	0	$X(z_i)$
x_i'	0	0	$-\xi_6 X''(\xi_3)$	1	0	$X'(z_i)$
y_i	0	1	$-\xi_5 - (z_i - \xi_3)\xi_6 Y''(\xi_3)$	0	$z_i - \xi_3$	$Y(z_i)$
y_i'	0	0	$-\xi_6 Y''(\xi_3)$	0	1	$Y'(z_i)$

In order to perform the first iteration, approximate values of the track derivatives x_i', y_i', $i = 1, \ldots, m$ are needed to compute X_i'', Y_i'' as in (5.20). In the spline fit version of PROG2 these were obtained from a standard Runge Kutta integration through the magnetic field. In the subsequent iterations values of x_i' and y_i' from eqs. (5.22) and (5.23) were used.

Thus the iteration procedure of the fitting of one event looks as indicated in fig. 5.4. The names of the appropriate PROG2-subroutines are indicated to the right.

It should be noted that in addition to the planes of measurement some interpolation planes have to be used in areas of the magnetic field with long distances between the measurement planes.

It turned out that one had to be careful when crossing the area in which the magnetic field decreases to zero. First of all it is necessary to

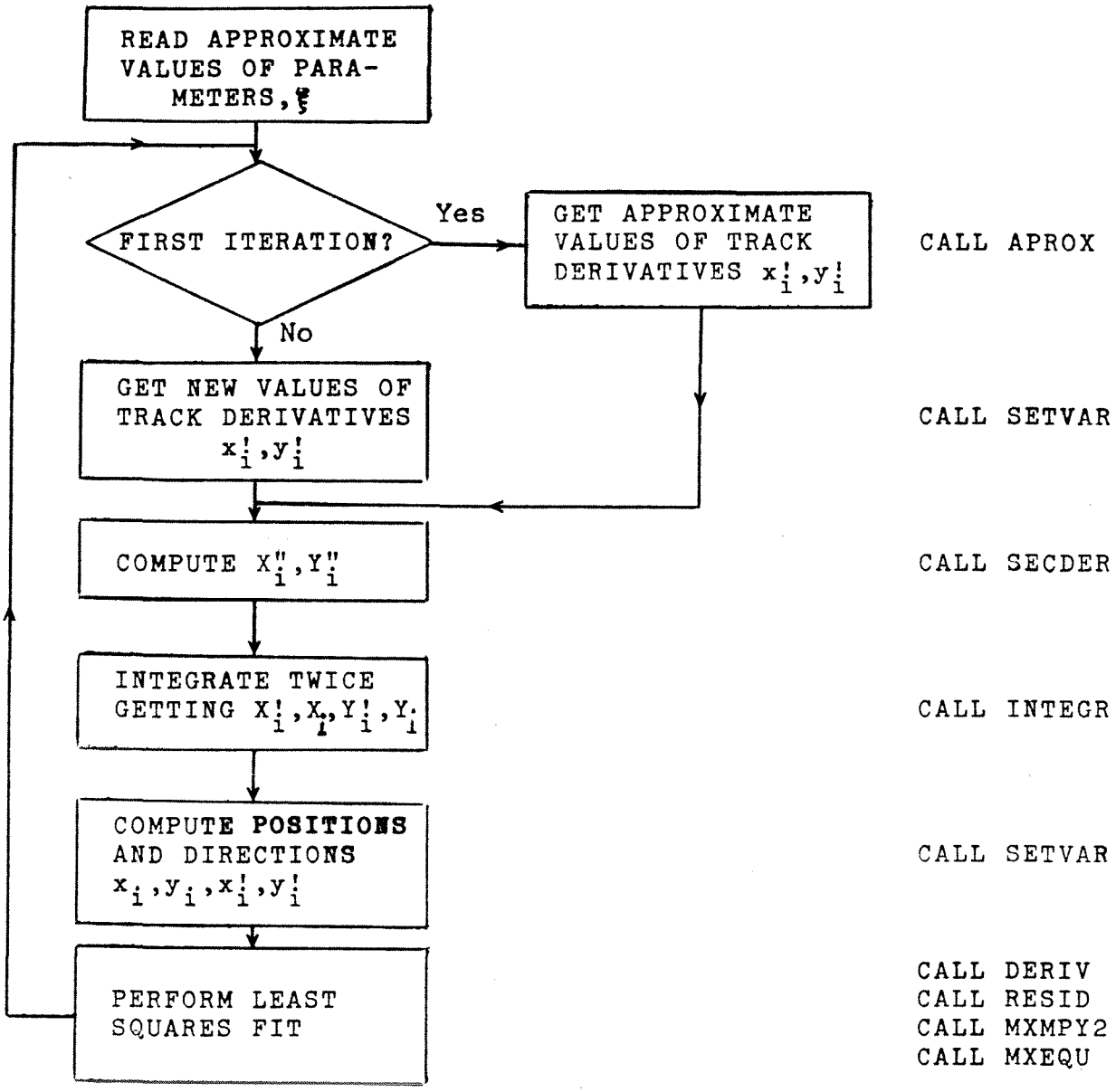

Fig.5.4 Iteration procedure of the quintic spline fit version of PROG2.
Tests on convergence,number of iterations performed etc.are not included for reasons of simplicity.
The MX-routines are those of [60].

have an interpolation plane at the end of the field to tell the programme that the magnetic field has reached zero. Secondly studies of Monte Carlo events showed that the programme worked better if it was not allowed to integrate according to the procedure of [67] all the way through the fringe field, but rather treat the second derivatives as constant between the interpolation planes of the fringe field.

5.5.3 The Runge Kutta Fit

Runge Kutta integration is an old and well known method of numerically integrating certain differential equations. It is straight forward to apply the Runge Kutta method to integrate equations (5.20), thus obtaining the functions f to be used in (5.2)

This has often been done in cases where high precision has been needed. The method has had the disadvantage, however, that the matrix of derivatives, D as defined in (5.3), has had to be computed numerically . To do that is very time-consuming since one full tracking is required for each parameter with respect to which the derivatives are to be computed.

During the work on the PROG2 package, however, it was discovered a simple way to compute the derivatives analytically together with the track positions and directions [69].

It turned out that in this way the Runge Kutta method became comparable to the quintic spline fit both with respect to speed and accuracy. A detailed description of the algorithm used and a comparison between the two methods, are given in Appendix II.

Analogously to fig. 5.4, fig. 5.5 shows the iteration procedure of the Runge Kutta version of the PROG2 package. Again the names of the appropriate subroutines are indicated to the right in the figure.

The reasons for choosing to use the Runge Kutta version instead of the quintic

spline fit were several.

The first and maybe most important reason is the simple one that the Runge Kutta method of integrating the equations of motion is an old, well tested and well understood method which is not expected to give surprises of any kind.

Secondly the Runge Kutta method can explicitly take into account the dependence of the magnetic field on x and y , simply by not making the approximation of eq. (27) in Appendix II.

It also seems to be more straight forward to perform things like fitting multiple scattering angles and taking energy loss along the track into account in the Runge Kutta formalism than in the quintic spline fit. It should be noted, however, that these things have not yet been incorporated in the PROG2 package, neither in the quintic spline nor in the Runge Kutta version.

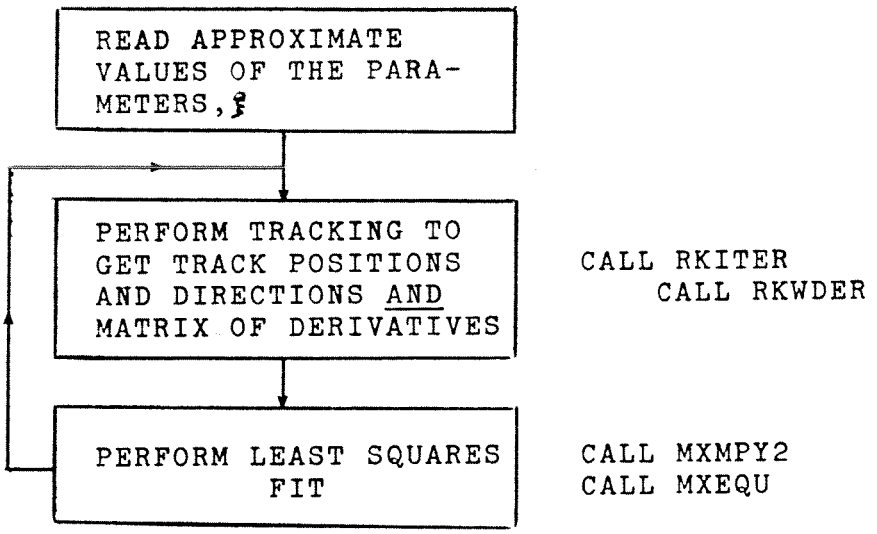

Fig.5.5 Iteration procedure of the Runge Kutta version of PROG2. See text.
Tests on convergence, number of iterations etc. are not included for reasons of simplicity.
The MX-routines are those of [60].

5.5.4 Performance of the PROG2 Package Without Kinematical Constraints

To test the PROG2 package numerous runs on Monte Carlo and real data have been performed. Firstly one may fit Monte Carlo events without introducing measurement errors. Then a chi-squared of effectively zero is expected for all the events. This is also what happens - with our choice of interpolation planes a fit of 100 elastic Monte Carlo events without errors gives a mean of $< \chi^2 > = 0.008$ and a standard deviation $\chi^2_{rms} = 0.02$.

Secondly one may introduce Gaussian distributed measurement errors on the track positions and directions, with standard deviations corresponding to the inverse of the weights used in the fit. Then the theoretically expected chi-squared distribution should have a mean value equal to the number of degrees of freedom, ν. As stated earlier, ν equals 17 when all the planes inside the magnet have clusters of both the outgoing tracks. The chi-squared distribution resulting from a run where 1000 such events were fitted, is shown in fig. 5.6. The theoretical chi-squared distribution with 17 degrees of freedom is superimposed on the histogram.

Fig. 5.7 shows the chi-squared distribution from a run where 2000 real events from a DST1 are fitted. The constraint of correct charge combination is not applied to the data. The long tail in the distribution is due to false event candidates.

More interesting is the low-chi-squared part of the histogram. We see that the region of maximum probability is well below 10, in contradiction to the previous (Monte Carlo) case.

Obviously the chi-squared distribution for real events is expected to be somewhat shifted towards smaller chi-squared since the number of degrees of freedom is not constantly equal to 17, but varies between 9 and 17. Therefore the plot of fig. 5.7 represents a superposition of chi-squared distributions with different numbers of degrees of freedom. This fact alone,

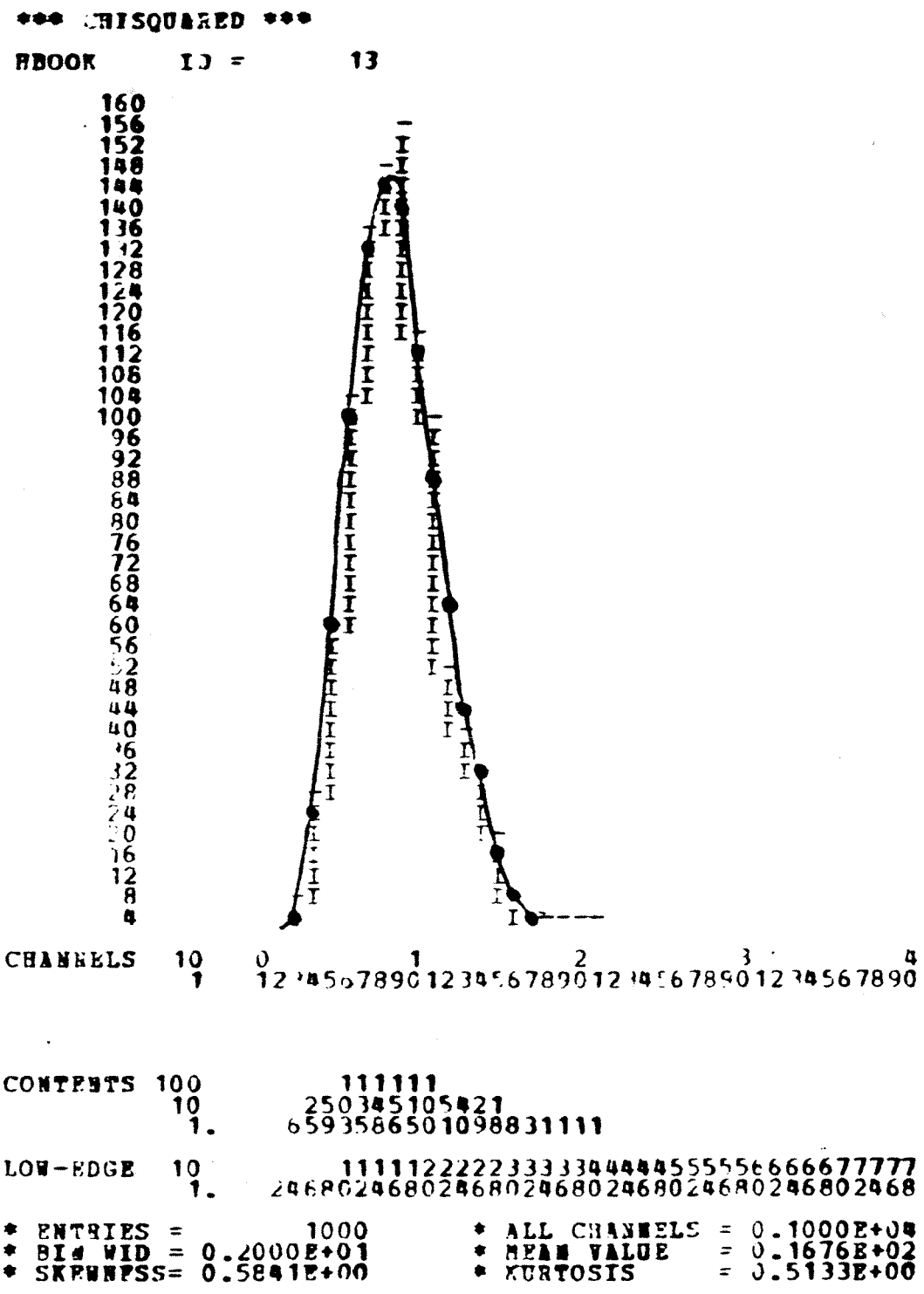

Fig. 5.6

Chi-squared distribution of 1000 fitted Monte Carlo events with Gaussian distributed measurement errors generated.

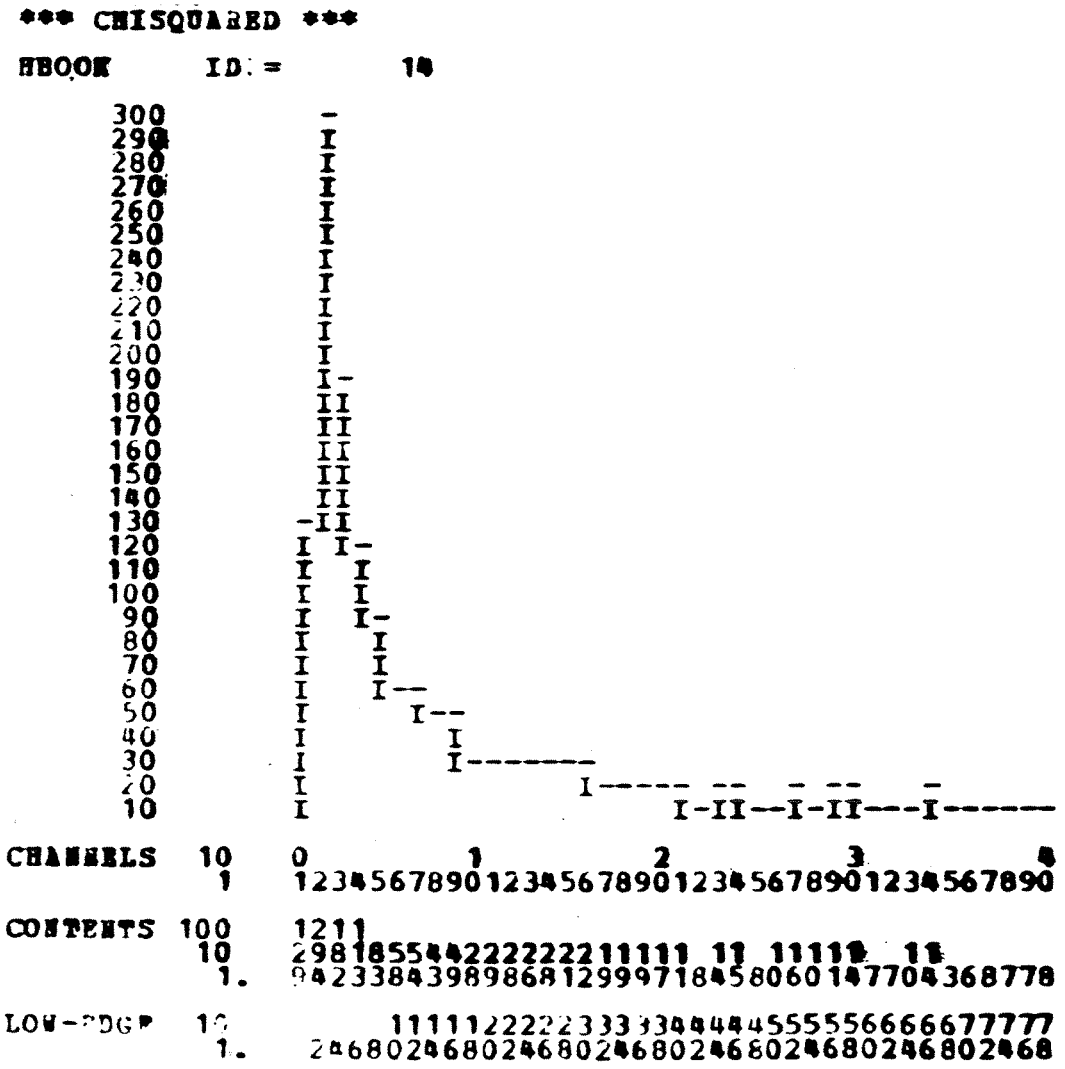

Fig. 5.7

Chi-squared distribution of 2000 fitted real events.

Correct charge combinations not required.

however, can not explain the large difference between the histograms of figs. 5.6 and 5.7.

The conclusion we must draw from the comparison of the two figures, is that the program operates with overestimated measurement errors, or equivalently under-estimated weights. The weights used in the fitting are those of table 5.2.

Table 5.2 Weights used in PROG2·

Measurement	Weight	Error
Digitisings in MWPC-planes (x,y,u,v)	5.	2 mm
x,y in reference planes (all tracks)*	5.	2 mm
$\frac{dx}{dz}$, $\frac{dy}{dz}$ in reference planes (all tracks)*	6000.	0.17 mrad
Beam momentum ($\Delta p/p$ = 1%; nom.value 20 GeV/c)	5.	200 MeV

* It should be noted that in cases when no beam track is reconstructed, the PROG2 package assumes a "measured" beam with $\left(x, y, \frac{dx}{dz}, \frac{dy}{dz}\right)$ =(0.,0.,0.,0.) in the beam reference plane, and errors 5 cm in x, y and 1 mrad in $\frac{dx}{dz}$, $\frac{dy}{dz}$, corresponding to weights of 0.2 and 1000., respectively.

A detailed study of what the correct weights should look like has not been carried out at the time of writing. It is, however, obviously not correct to apply the same weights on measured positions in a 1 mm plane as in a 2 mm plane, the same weights on positions and directions in the left arm as in the right one etc. We will not go further into this matter here. For details on execution times, one should consult section 6 of Appendix II.

5.5.5 The Application of the Kinematical Constraints

An elastic event satisfies the following constraint equations from energy-momentum conservation:

$$F_\ell(\xi) = 0 \qquad \ell = 1, \ldots, 4 \tag{5.28}$$

$\ell = 1, \ldots,3$ represent momentum conservation and $\ell = 4$ represents energy conservation. We have

$$\begin{aligned}
F_1(\xi) &= \xi_4 \frac{c/\xi_6}{\sqrt{1+\xi_4^2+\xi_5^2}} + \xi_7 \frac{c/\xi_9}{\sqrt{1+\xi_7^2+\xi_8^2}} - \xi_{10} \frac{c/\xi_{12}}{\sqrt{1+\xi_{10}^2+\xi_{11}^2}} \\
F_2(\xi) &= \xi_5 \frac{c/\xi_6}{\sqrt{1+\xi_4^2+\xi_5^2}} + \xi_8 \frac{c/\xi_9}{\sqrt{1+\xi_7^2+\xi_8^2}} - \xi_{11} \frac{c/\xi_{12}}{\sqrt{1+\xi_{10}^2+\xi_{11}^2}} \\
F_3(\xi) &= \frac{c/\xi_6}{\sqrt{1+\xi_4^2+\xi_5^2}} + \frac{c/\xi_9}{\sqrt{1+\xi_7^2+\xi_8^2}} - \frac{c/\xi_{12}}{\sqrt{1+\xi_{10}^2+\xi_{11}^2}} \\
F_4(\xi) &= \sqrt{m_1^2 + c^2/\xi_6^2} + \sqrt{m_2^2 + c^2/\xi_9^2} - \sqrt{m_3^2 + c^2/\xi_{12}^2} - m_4
\end{aligned} \tag{5.29}$$

In the above expressions c is the speed of light, $m_1(m_2)$ is the mass of the left (right) arm outgoing particle, and $m_3(m_4)$ the mass of the beam (target) particle.

Eqs. (5.28) can be taken into account in different ways by the fitting program. We will shortly describe two of them.

(i) The Method of Lagrangian Multipliers

We now search for corrections $\Delta\xi$ to ξ such that s^2 as defined in (5.6) is minimum under the boundary conditions that

$$F_\ell(\xi + \Delta\xi) = 0 \quad ; \ell = 1, \ldots, 4 \tag{5.30}$$

As seen from eqs.(5.29) F is not linear in ξ, but we linearize it by setting

$$F_\ell(\xi + \Delta\xi) = F_\ell(\xi) + \sum_\alpha \frac{\partial F_\ell}{\partial \xi_\alpha} \Delta\xi_\alpha \tag{5.31}$$

With $B_{\ell\alpha} = \frac{\partial F_\ell}{\partial \xi_\alpha}$ we can then write (5.30) in matrix notation :

$$F(\xi) + B\Delta\xi = 0 \tag{5.32}$$

The computation of B is easily performed by differentiation of eqs.(5.29).

Minimization of the sum of squares, s^2, with the conditions (5.32) leads to the following analogy to eq.(5.14) :

$$D^T D\Delta\xi = D^T\delta + B^T\alpha \tag{5.33}$$

α containing the Lagrangian multipliers. I.e., the variation of s^2 along the hypersurface F should be zero.

Solving (5.33) for $\Delta\xi$ and putting the result into (5.32) gives for α :

$$\alpha = -(B^T)^{-1} D^T[DB^{-1}F + \delta] \tag{5.34}$$

By substituting this for α in (5.33), we finally arrive at

$$\Delta\xi = (D^T D)^{-1}[D^T\delta - \{D^T DB^{-1}F + D^T\delta\}] \tag{5.35}$$

We see that the method of Lagrangian multipliers requires one extra matrix inversion compared to the case with no constraints applied. It turned out that this in some cases gave rise to numerical problems because of the limited calculational accuracy on an IBM with 32 bit wordlength. It was therefore decided to change to the method described below.

(ii) The Method of Explicit Elimination of Variables

The four constraints reduce the number of free parameters from 12 to 8. It is therefore possible to use the constraint equations to eliminate four parameters and express the 12 ξ's by 8 free parameters η

$$\xi = \xi(\eta) \tag{5.36}$$

In order to make a fit for η, we need the derivatives $\frac{\partial f}{\partial \eta}$.

Let us define

$$D'_{i\beta} = \frac{\partial f_i}{\partial \eta_\beta}$$

$$A_{\alpha\beta} = \frac{\partial \xi_\alpha}{\partial \eta_\beta} \qquad (5.37)$$

Then we may write in matrix notation

$$D' = DA \quad \text{and, by multipling by the weights,}$$

$$D' = \mathcal{D}A \qquad (5.38)$$

D and $\mathcal{D}$ are the matrices defined in (5.3) and (5.13), respectively. The equation for the corrections $\Delta\eta$ then looks like (in analogy to eq.(5.14)) :

$$D'^{T}D' \, \Delta\eta = D'^{T}\delta \qquad (5.39)$$

The new values of ξ are given by $\xi = \xi(\eta + \Delta\eta)$.

The parameters η may be chosen in different ways. The choice adopted by the PROG2 package is the following.

$\eta_{1, \ldots,3}$: the x,y,z component of the final state centre of mass momentum.

$\eta_{4,5}$: the directions $\frac{dx}{dz}$, $\frac{dy}{dz}$ of the beam track at vertex.

$\eta_{6, \ldots,8}$: x,y,z of the vertx

When the constraint equations are applied, the number of degrees of freedom, ν, increases by 4. I.e., with all planes giving clustes, ν equals 21.

5.5.6 Fit with Non-Diagonal Error Matrix

The approximation of diagonal error matrix which makes (5.11) change into (5.14) is only correct as far as Coulomb scattering can be neglected. A little investigation on this problem, which verifies this approximation in the WA7 case, is presented in Appendix III.

CHAPTER 6 OFF-LINE SOFTWARE - MONTE CARLO

6.1 Introduction

Monte Carlo calculations are essential to any high energy physics experiment. A Monte Carlo programme simulates events on the basis of random numbers. Such simulations have to be done for a number of reasons:

(1) To find the optimum geometrical arrangement of the apparatus.

(2) To select reasonable triggering criteria.

(3) To test the on- and off-line software.

(4) To study different effects and processes (like multiple Coulomb scattering, energy loss, particle decays, background reactions etc.).

(5) To compute the final geometrical acceptance.

We will not discuss the theory behind the Monte Carlo method here, but restrict ourselves to a short description of the WA7 Monte Carlo programme and some of its applications.

6.2 The WA7 Monte Carlo Programme

The basic version of the WA7 Monte Carlo programme generates elastic collisions, performs tracking of the beam and outgoing particles, computes the impacts in the various planes of measurement and eventually produces a Monte Carlo data tape. Other reactions than elastic scattering may be generated by substituting the elastic event generating routine by other user-supplied routines.

By applying another program, CODEMC, the Monte Carlo data may be converted to cluster centres, fired hodoscope elements etc., thus simulating the raw data written by the on-line computer.

An elastic event is completely described by 8 independent variables. The 8 variables which are generated in the WA7 Monte Carlo programme are:

(i) The magnitude of the beam momentum.

(ii) $\frac{dx}{dz}$ of the beam at the target entrance.

(iii) $\frac{dy}{dz}$ of the beam at the target entrance.

(iv) the x-position of the beam at the target entrance.

(v) the y-position of the beam at the target entrance.

(vi) the z-position of the vertex.

(vii) the cosine of the radial scattering angle.

(viii) the azimuthal scattering angle.

All these variables are generated uniformly distributed between upper and lower limits set by the user.

6.2.1 Tracking and Calculation of Hit-Points

The tracking of the particles through the magnetic field is done by the same Runge Kutta integration method as is described in Appendix II, except that the derivatives with respect to the initial track parameters are of course not calculated.

The routine uses z as integration variable, and the tracking is performed between fixed z-positions, not dependent on the positions of the measurement planes. Positions, derivatives and second derivatives in these fixed planes are stored and eventually written to tape. Hitpoints in actual detector planes are determined by a fifth order interpolation between the two nearest fixed z-planes.

This makes a flexible system. For instance the data from one single Monte Carlo run may be used to study the effect of changing the positions of certain detector planes.

To save time bad events should be thrown away as early as possible. Therefore rough tests are made immediately after the event is generated to ensure that the tracks go forward in lab and that they escape through the magnet.

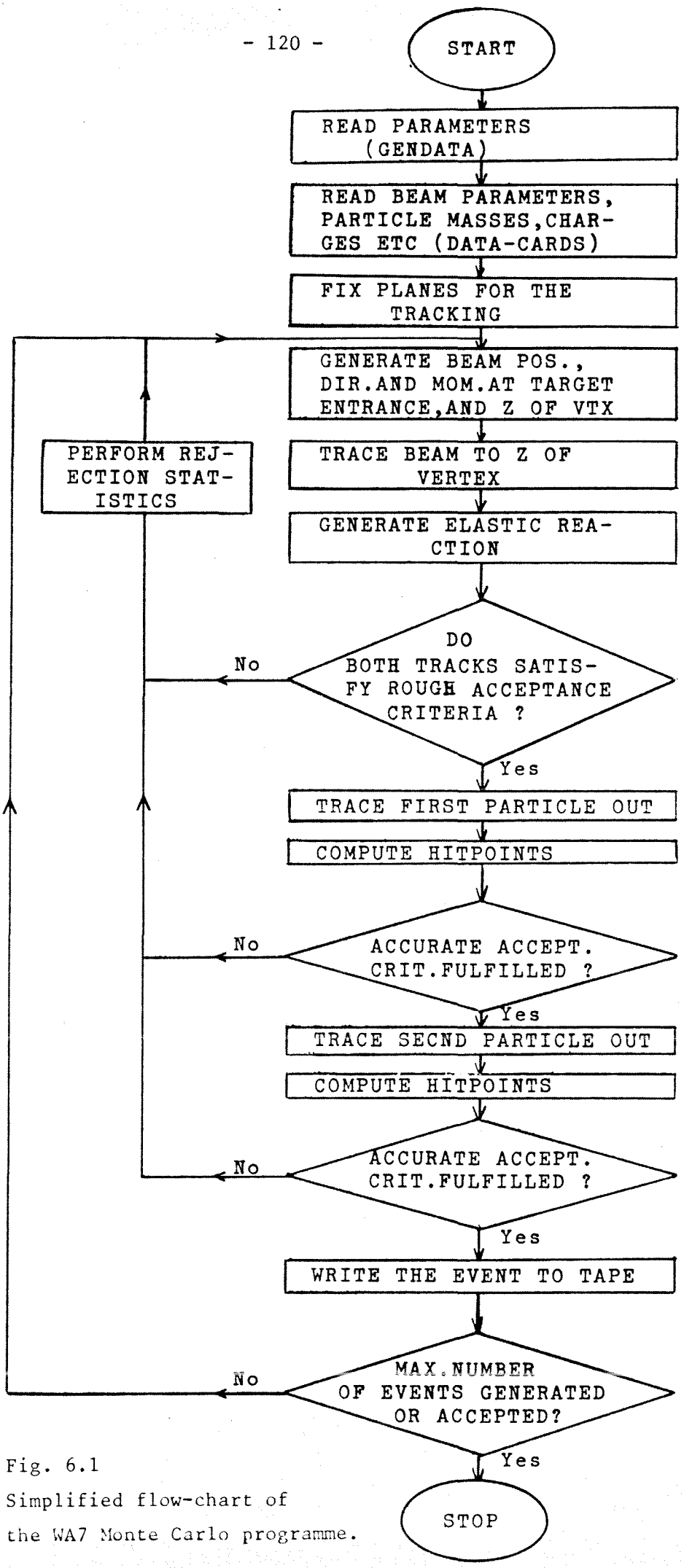

Fig. 6.1
Simplified flow-chart of the WA7 Monte Carlo programme.

After the tracking accurate acceptance criteria may be applied. For an event to be accepted, one may demand that all the hodoscopes are hit, that more than a minimum number of MWPC-planes are hit in the sensitive area, etc. A simplified flow-chart of the Monte Carlo programme is presented in fig. 6.1.

6.3 Monte Carlo Calculation of the Geometrical Acceptance

The number of accepted events, n, in a bin (of t, say), out of N generated ones in the same bin, follows a binomial distribution

$$Pr(n) = \binom{N}{n} a^n (1 - a)^{(N-n)} \tag{6.1}$$

Here a is the acceptance in that bin. We estimate it by

$$a = \frac{n}{N} \tag{6.2}$$

From the expectation value and variance of the binomial distribution it follows that this estimator has correct expectation value, and that the standard derivation may be estimated by

$$\sigma_a = \frac{\sqrt{n}}{N} \sqrt{1 - \frac{n}{N}} \tag{6.3}$$

For small $\frac{n}{N}$ we may write

$$\sigma_a \approx \frac{\sqrt{n}}{N} \tag{6.4}$$

Fig. 6.2 shows the acceptance as a function of t and $\cos\theta_{CM}$ for 20 GeV/c π^-beam and geometrical parameters as used in the run of June 1978.
To be accepted the events had to hit all the four hodoscopes and all MWPC-planes in the sensitive area. In addition it was required that the π should go in the left arm. The matrices of the trigger were not taken into account. Two short reports on special acceptance calculations are presented in Appendix IV.

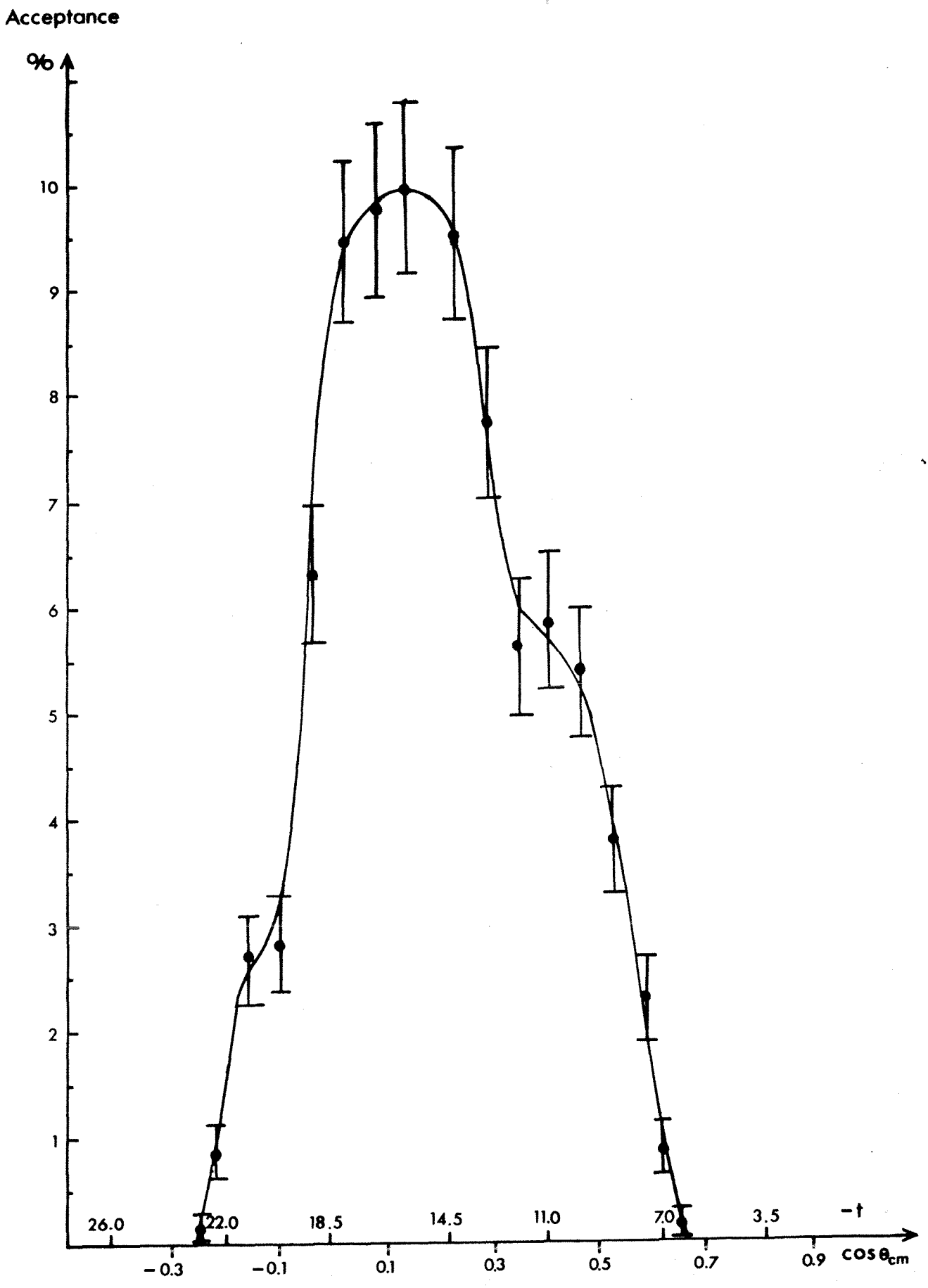

Fig. 6.2

Acceptance for $\pi\bar{p}$ at 20 GeV/c. See the text.

6.4 Monte Carlo Generation of Multiple Coulomb Scattering

When a particle traverses a material it suffers multiple Coulomb scattering. We denote by θ the angle which the particle makes with its original direction after having traversed a thickness x of the medium. The projection of θ onto any plane containing the initial direction is called θ^{proj}. The projected angle is approximately Gaussian distributed [70] with mean zero.

If the particle has momentum p (in GeV/c), velocity β (in units of c), and the material has radiation length x_o, the standard deviation in the Gaussian distribution is

$$\sigma = \sqrt{<\theta^{proj\,2}>} = \frac{0.015}{p\beta}\sqrt{\frac{x}{x_o}} \qquad (6.5)$$

If the particle traverses N different materials, each with radiation length x_{o_i} and thickness x_i, the standard deviation in the distribution is

$$\sigma = \frac{0.015}{p\beta}\sqrt{\sum_{i=1}^{N}\frac{x_i}{x_{o_i}}} \qquad (6.6)$$

The formula is only correct to within 10-20% [71]. If $x < \frac{1}{10}x_o$ a better estimate of the standard deviation is obtained by multiplying σ by a factor $(1 + \varepsilon)$ where ε is of the order of 0.1.

In Appendix V a way of Monte Carlo generating multiple scattering is presented together with some results for 20 GeV/c elastic scattering.

CHAPTER 7 THE ANALYSIS OF 20 GeV/c DATA

7.1 Introduction

In this chapter we will shortly discuss some aspects of the data analysis at 20 GeV/c, and present preliminary results for π^+p and π^-p elastic scattering.

7.2 Trigger and Analysis Performance

In order to understand the data, we will consider a representative run and follow the stream of data in some detail. For this purpose we have chosen run no. 2020, which was a run with positive 20 GeV/c beam. The data were recorded in November 1978. The majority veto for this run was set according to eq. (4.9), chapter 4.

The mean number of incoming particles per burst was $\sim 30.4 \times 10^6$. Out of the resulting reactions, by far the largest fraction was filtered out at the trigger level. On the average only $\sim$ 109 triggers were accepted per burst and written to the raw data tape. I.e., only a fraction $\sim 3.6 \times 10^{-6}$ of the incoming particles gave rise to event candidates.

Details on the numbers of the various coincidences in the trigger can be found in table 7.1.

From the table we see that the PR1•PR2 coincidence (an "or" of the two programmable or's, see chapter 4), is the part of the strobe which rejects most reactions. Likewise we see that among the fast matrices, the one which performs the PR2•H2R coincidences accepts the least fraction of the reactions.

From the table it is also possible to estimate the effect of having the Cerenkovs and CEDARs in the trigger. The reduction from 902 (48×48) •strobe• $\overline{\text{majority}}$ -coincidences to 109 "events" per burst is partly due to the Cerenkovs and CEDARs, and partly a dead-time effect.

Table 7.1 Trigger performance for a typical run (see the text).

	Total	Per burst	Per burstscaler
No. of bursts	428		
No. of integrated burstscalers	1.3×10^{10}	30.4×10^{6}	
No. of PR1·PR2 coincidences	8.17×10^{7}	1.91×10^{5}	6.3×10^{-3}
No. of PR1·H1R coincidences	3.11×10^{8}	7.24×10^{5}	2.4×10^{-2}
No. of PR2·H2R coincidences	1.80×10^{8}	4.21×10^{5}	1.4×10^{-2}
No. of H1R·H2R coincidences	2.41×10^{8}	5.63×10^{5}	1.9×10^{-2}
No. of H1W·H2W coincidences	3.63×10^{8}	8.48×10^{5}	2.8×10^{-2}
No. of fast strobes	5.48×10^{6}	1.28×10^{4}	4.2×10^{-4}
No. of 48×48 -coincidences	3.23×10^{6}	7.55×10^{3}	2.5×10^{-4}
No. of (48×48)·strobe·$\overline{\text{majority}}$	3.86×10^{5}	902	3.0×10^{-5}
No. of triggers to NORD10 ("events")	4.67×10^{4}	109	3.6×10^{-6}

Estimating the live-time fraction to be ~ 0.65 (from the ratio of gated to ungated scalers, see also p. 85), the real number of "events" per burst is ~ 170. I.e., the Cerenkovs and CEDARs represent a reduction of the trigger rate by a factor ~ 5 .

The 46797 triggers written to tape were then input to the analysis chain. Roughly 80% of the triggers were rejected by the PROG1 package. The majority of the rejections occurred in the pattern recognition stage (~ 69%) and in the vertex reconstruction routine (~ 8%). The rest of the rejections were due to bad data and occurred in various decoding routines. The dominant reason of rejections in the pattern recognition, was lack of digitisings (see section 5.4.3). The rejections in the vertex reconstruction part were due to too large 2-prong vertex parameter (> 3 cm).

The 20% of the triggers accepted by PROG1 were then input to the PROG2 programme package which performed a geometrical fit (without the application

of the kinematical constraints). Only events with correct c
(see p. 99) were fitted. It turns out that the constraint o
combination is a very selective one.

For the run under consideration, the number of triggers inpu
was 9299, with a number of event candidates of 11336 (corres
average of 1.2 event candidates per trigger). Out of these,
had wrong charge combination.

Among the 466 remaining event candidates, 263 gave a success
fit with chi-squared less than 100. These 263 event candidat
input to PROG2, this time performing a combined geometrical
fit (see section 5.5.5). The nominal beam (see footnote to
was used for all events. 30 events survived with a kinemati
less than 500. Out of these 2 had a chi-squared less than 4
seriously might be considered as possible elastic event cand
next section).

The history of the run is indicated in table 7.2

Table 7.2 Run history of a typical run, 20 GeV/c positive be

TRIGGER	No. of bursts	428
	No. of integrated burstscalers	1.3×10^{1}
	No. of fast strobes (ungated)	5.5×10^{6}
	No. of triggers to tape	4.7×10^{4}
PROG1	No. of triggers input	$4.7\ 10^{4}$
	No of triggers accepted	9299 (20
PROG2 WITHOUT KINEMATICS	No. of triggers input	9299
	No. of events input	11336
	No. of events with correct charge comb.	466
	No. of events accepted, $\chi^2_g < 100$	263
PROG2 WITH KINEMATICS	No. of events input	263
	No of events with $\chi^2_k < 500$	30
	No of events with $\chi^2_k < 40$	2

Runs with negative beam do not look very different, and the numbers of table 7.2 are representative for all the data taken at 20 GeV/c incident momentum. Some distributions of reconstructed quantities (PROG1 without cuts) are presented in figs. 7.1 and 7.2. Fig. 7.1 (a), (b), (c) and (d) shows x,y, $\frac{dx}{dz}$ and $\frac{dy}{dz}$, respectively, in the beam reference plane of the reconstructed beam tracks.

In fig. 7.2 (a) and (b) are shown the 2-prong vertex parameter and the squared 3-prong parameter, respectively. Vertices are only accepted as 3-prong ones if the squared 3-prong parameter is less than 1 cm^2.

Fig. 7.2 (c) and (d) shows the z-vertex distribution for 2- and 3-prong vertices, respectively. In (c) we observe that a rather large fraction of the vertices have z outside the target. The peak to the left corresponds to vertices in the beam hodoscope just upstream of the target. The vertices downstream of the target are mostly false event candidates with reconstructed vertices in CH1. This is clearly seen from (d), where only 3-prong vertices enter the histogramme. Requiring 3-prong vertices makes a much cleaner sample, and nearly all the vertices in CH1 disappear.

To get a feeling of what the background looks like, it is of interest to study the reconstructed (PROG1) momenta of the accepted triggers. It turns out that the forward (left arm) particles are mostly positive, and the recoil (right arm) particles are mostly negative. This is true both for positive and negative beam, and is in accordance to the low number of triggers with correct charge combination already mentioned. In addition the recoil arm Cerenkov requirement $\overline{C3} \cdot \overline{C4}$ accepts unwanted, low-momentum pions. The K- and p -triggers (C2 and $\overline{C1} \cdot \overline{C2}$, respectively), also accept low-momentum pions in the forward arm. Thus the background generally consists of low-momentum pions, a positive one in the forward arm, and a negative one in the recoil arm. This charge combination is favoured by the trigger because then the low-momentum pions are bent outwards towards

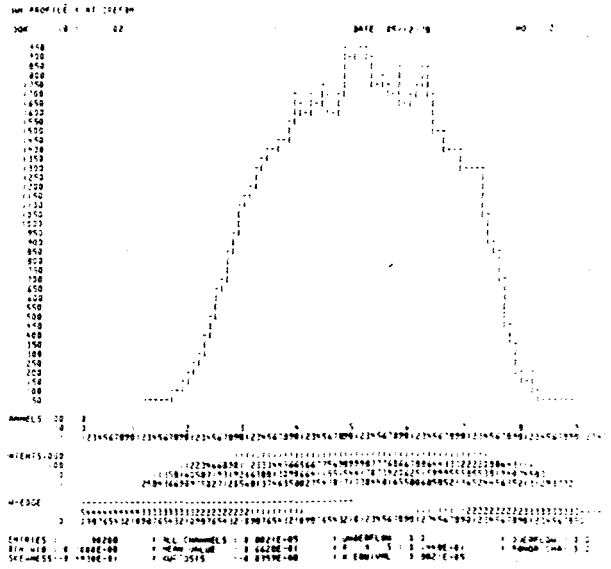

(a)

x of the beam

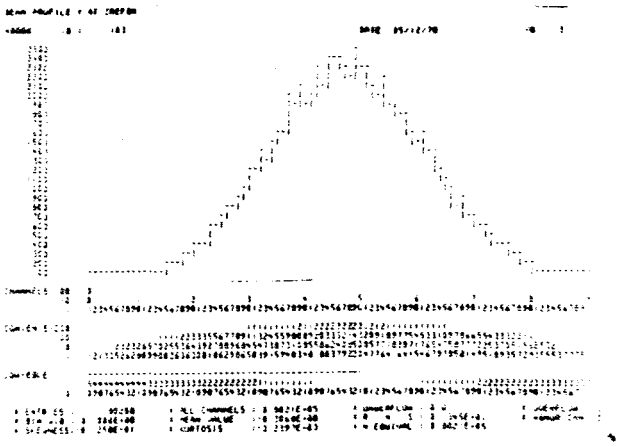

(b)

y of the beam

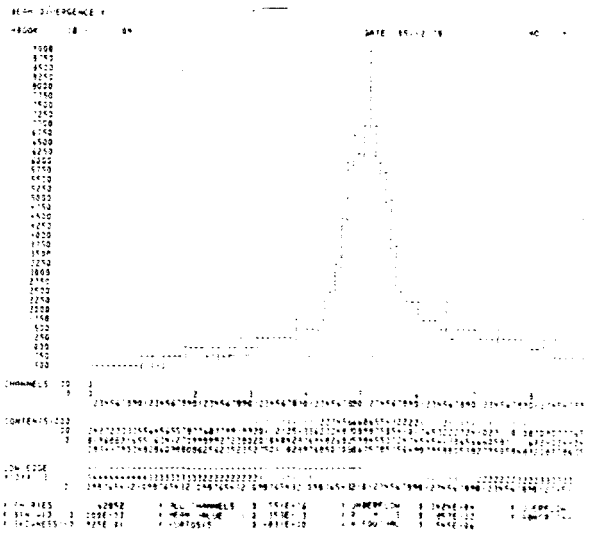

(c)

dx/dz of the beam

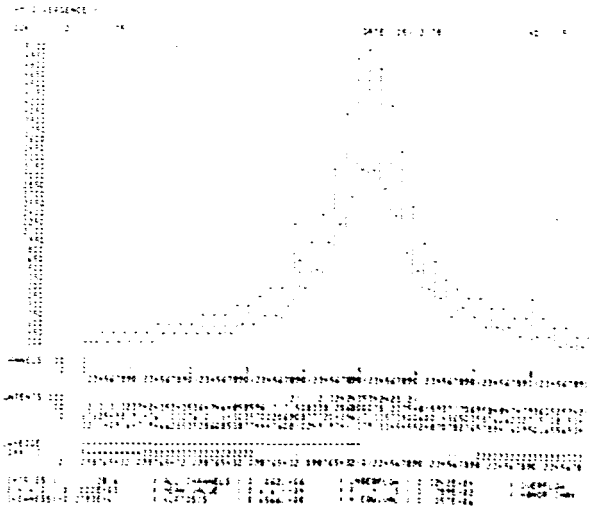

(d)

dy/dz of the beam

Fig.7.1

PROG1 reconstructed beam parameters.

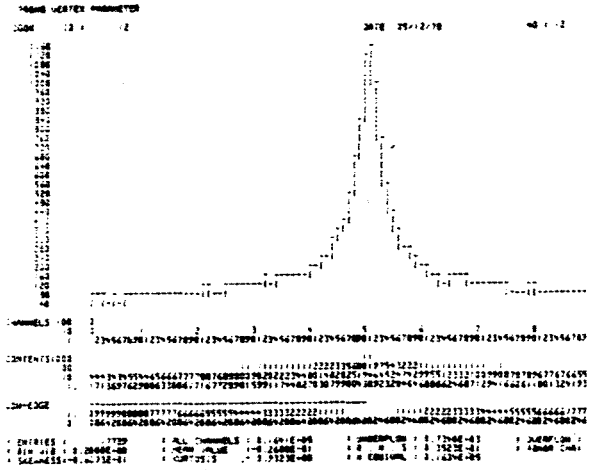

(a)

2-prong vertex parameter

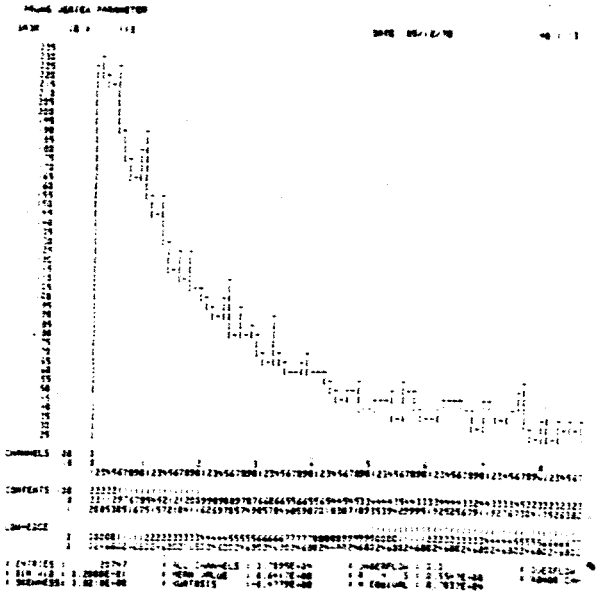

(b)

3-prong vertex parameter squared

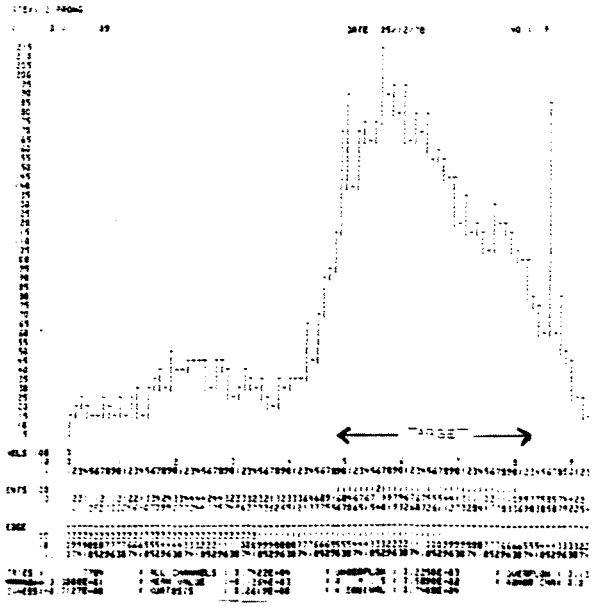

(c)

z-distribution,2-prong vertices

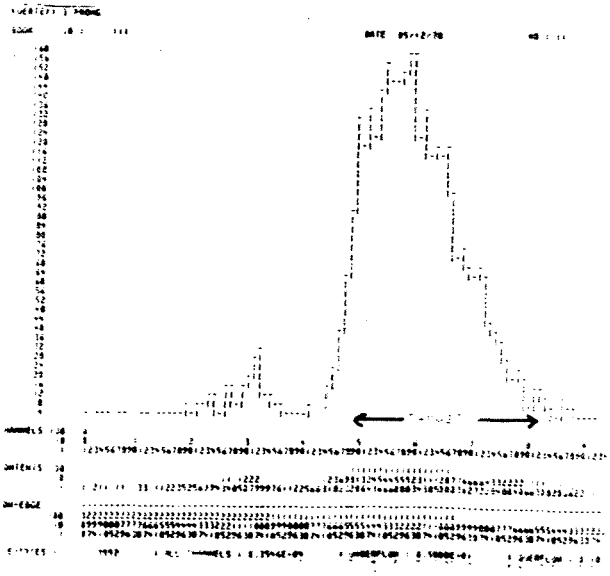

(d)

z-distribution,3-prong vertices

Fig.7.2

PROG1 reconstructed vertex parameters.

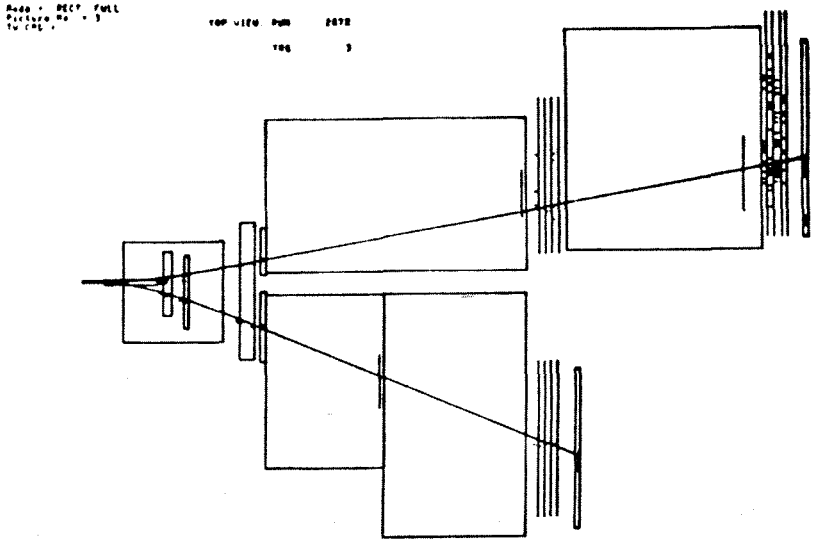

(a)

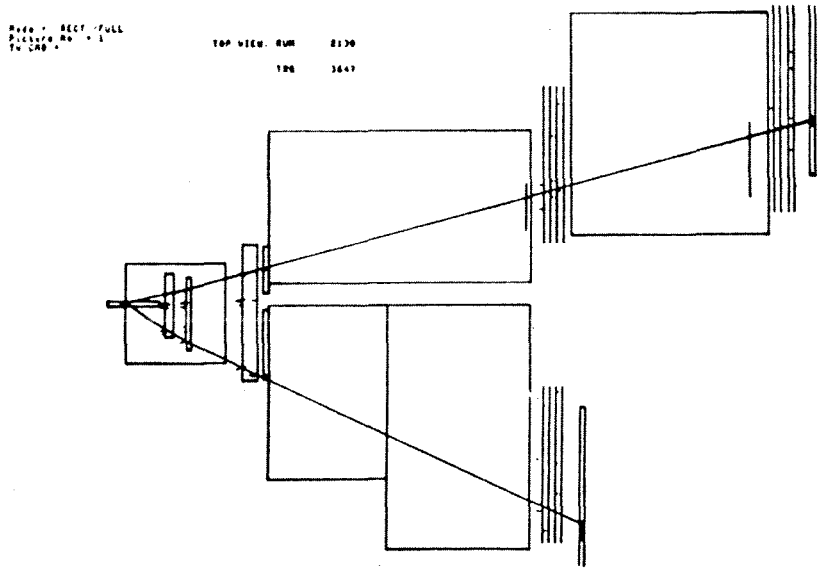

(b)

Fig.7.3 (a) Typical background event.
(b) Elastic π^+-event.

an opening angle simulating elastic geometry. Display of a typical background event is shown in fig. 7.3 (a), whereas a genuine π^+p -event is shown in fig. 7.3 (b).

As seen from fig. 7.2 (c) and (d), the requirement of 3-prong vertices highly increases the data quality. Because of the limited combined beam track detection and -reconstruction probability, however, the existence of a 3-prong vertex can not be taken as an acceptance criterion. At the level of output from PROG1, only ~ 40% of the events have a 3-prong vertex.

7.3 Event Selection

In fig. 7.4 kinematical chi-squared distributions for the π^+-data are presented. In (a) no cuts are applied except that the CEDAR signals should be those of π incoming. In (b) an additional requirement of the Cerenkovs to satisfy the π-trigger, is applied. We observe a dramatic enhancement of the elastic signal. Requiring now in addition the vertex to be inside target, we arrive at (c). We already see a clean event distribution against an as "clean" background distribution.

All the chi-squareds of fig. 7.4 result from fits with the nominal beam. Now throwing away all the 3-prong events which give a kinematical chi-squared greater than 100 for a fit with the measured beam, we arrive at (d). For π^- the data are even cleaner. Fig. 7.5 (a)-(d) show exactly the same chi-squared distributions for negative beam.

According to these plots, and supported by the Monte Carlo data results of fig. 7.6 (a) and (b), we choose the following simple acceptance criteria in our preliminary analysis, both for π^+ and π^- :

(i) There should be a π incident.

(ii) The vertex should be inside the target.

(iii) The kinematical chi-squared from a fit with nominal beam should be less than 40.

(iv) If the event has a 3-prong vertex, a kinematical fit with the measured beam should give a chi-squared less than 100.

An elastic event is coplanar. With $\vec{p}_1$ being the beam momentum, and $\vec{p}_2$ and $\vec{p}_3$ the forward and recoil arm momentum, respectively, we define the coplanarity factor c as follows

$$c = \frac{\vec{p}_1 \cdot (\vec{p}_2 \times \vec{p}_3)}{|\vec{p}_1| \cdot |\vec{p}_2 \times \vec{p}_3|} \qquad (7.1)$$

Within the resolution, the events should have $c = 0$. In fig. 7.7 is shown a scatterplot of c against the kinematical chi-squared for the π^+ events which are accepted. We see that the events with worst coplanarity also have the biggest chi-squareds. It is possible that some of these events will be thrown away by a more refined analysis.

7.4 Results

The cross section in a bin, Δt, of t is given by

$$\frac{d\sigma}{dt} = \frac{1}{n_{tgt}^{area} \cdot F_{corr} \cdot corr \cdot \Delta t} \cdot \frac{N^{obs}}{acc} \qquad (7.2)$$

Here n_{tgt}^{area} is the number of target protons per unit area perpendicular to the beam, F_{corr} is the counted number of incoming particles corrected for dead-time, C1, C2 efficiency and random veto (see below), corr is an overall correction factor (to be specified below), N^{obs} is the observed number of events in the t-bin, and acc is the acceptance in that bin.

For the number of target protons per area we have

$$n_{tgt}^{area} = 2 \cdot \frac{\rho_{H_2} N_{avo}}{m_{H_2}} \cdot L \qquad (7.3)$$

ρ_{H_2} is the density of liquid hydrogen (0.071 g/cm^3). N_{avo} is Avogadro's number ($6.022 \times 10^{23}\ \frac{1}{g}$), m_{H_2} is the hydrogen molecular mass in atomic units

(a)

(b)

(c)

(d)

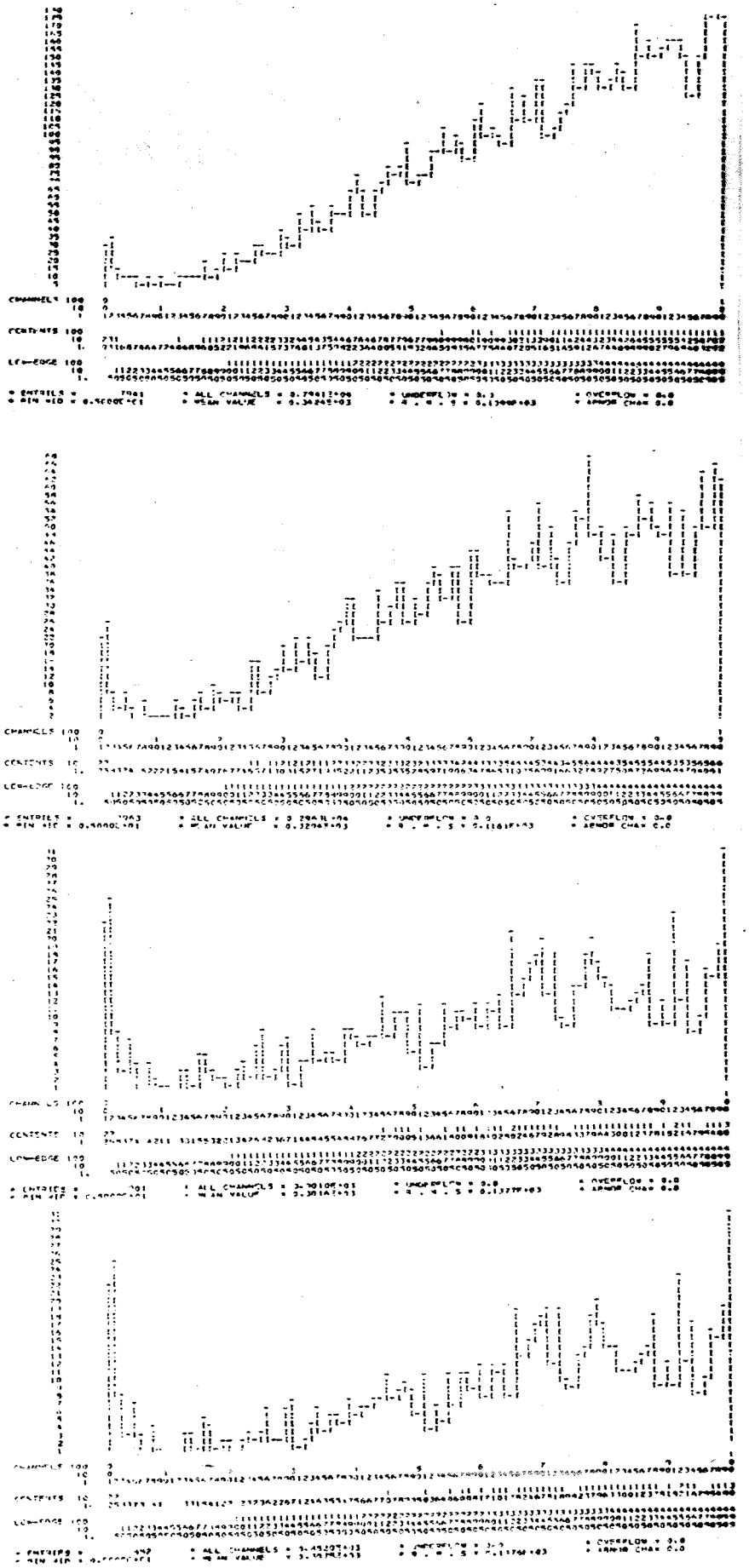

Fig.7.4 Kinematical chi-squared distributions for π^+.
See the text.

(a)

(b)

(c)

(d)

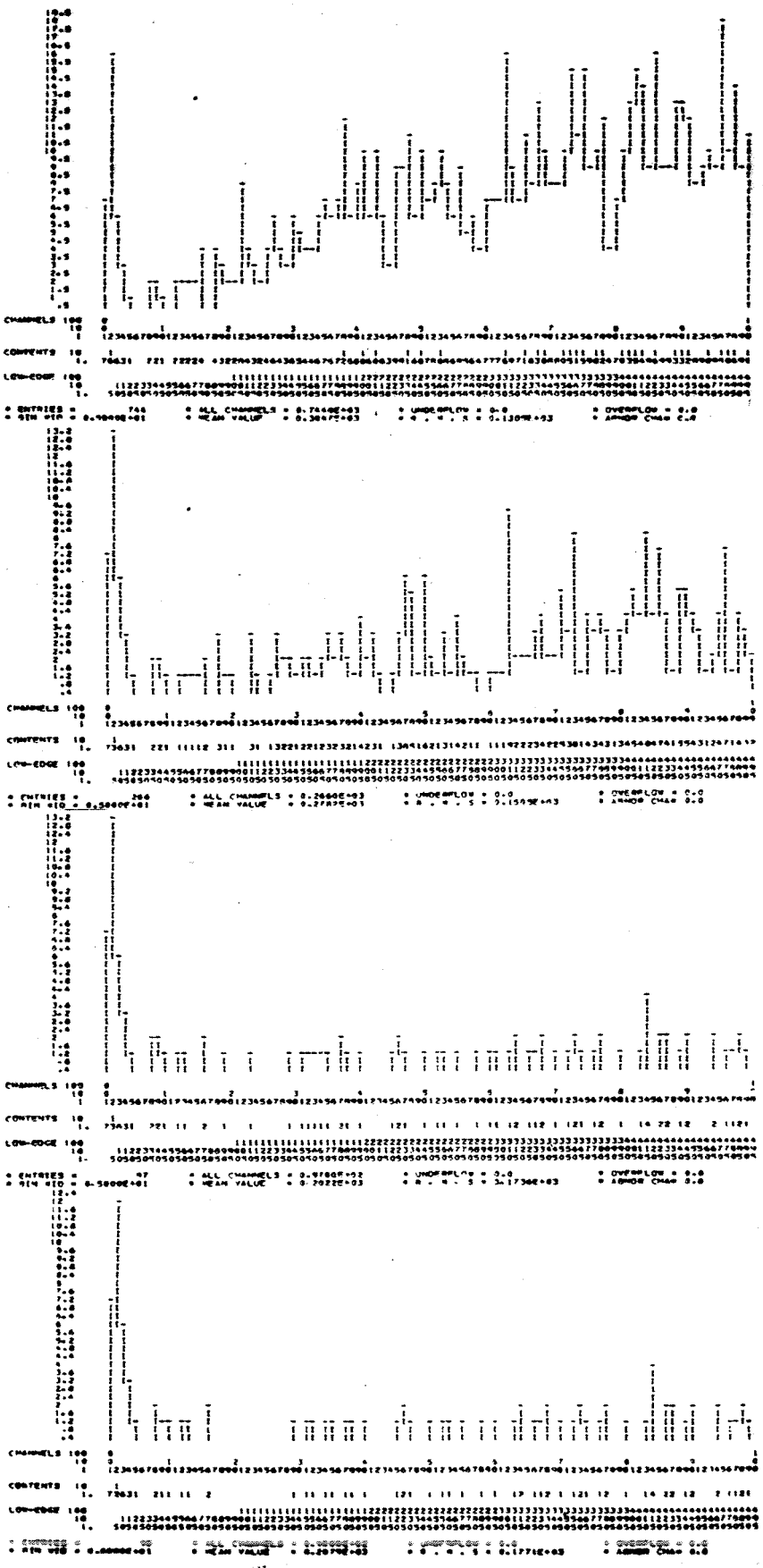

Fig.7.5 Kinematical chi-squared distributions for π^-.
See the text.

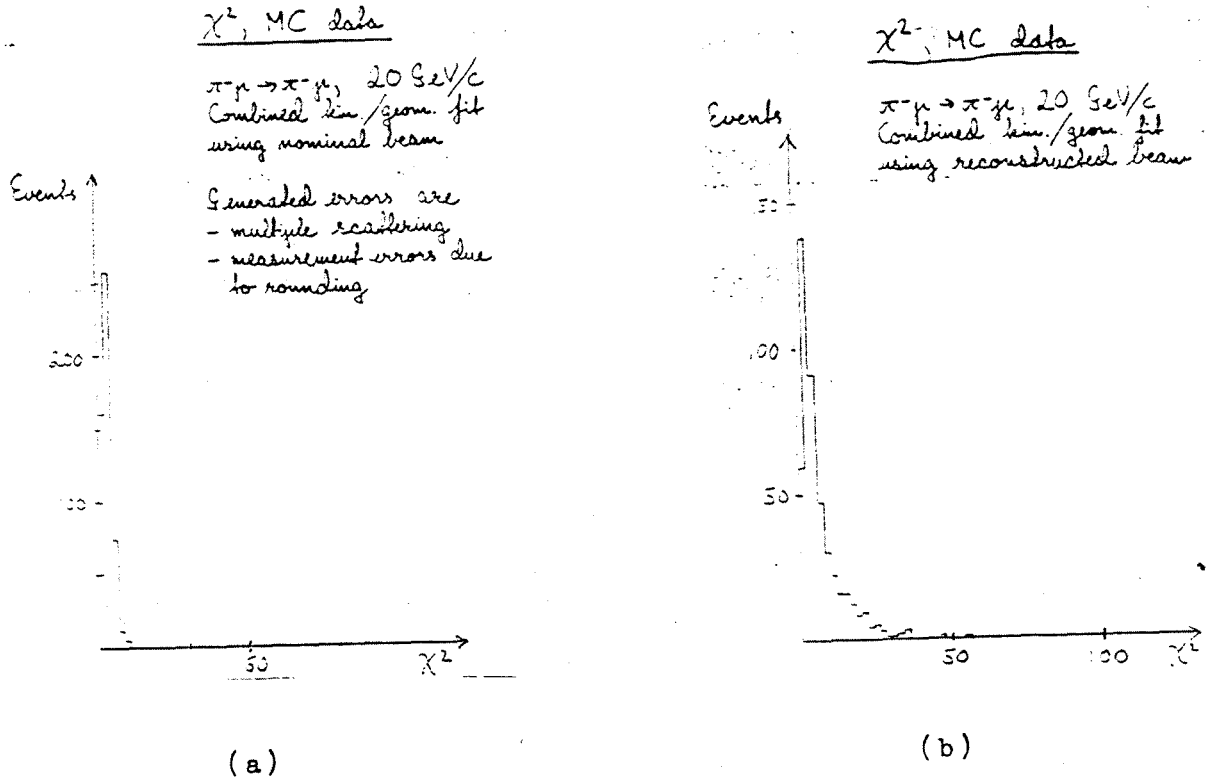

Fig.7.6 Kinematical chi-squared distributions of fitted Monte Carlo events.

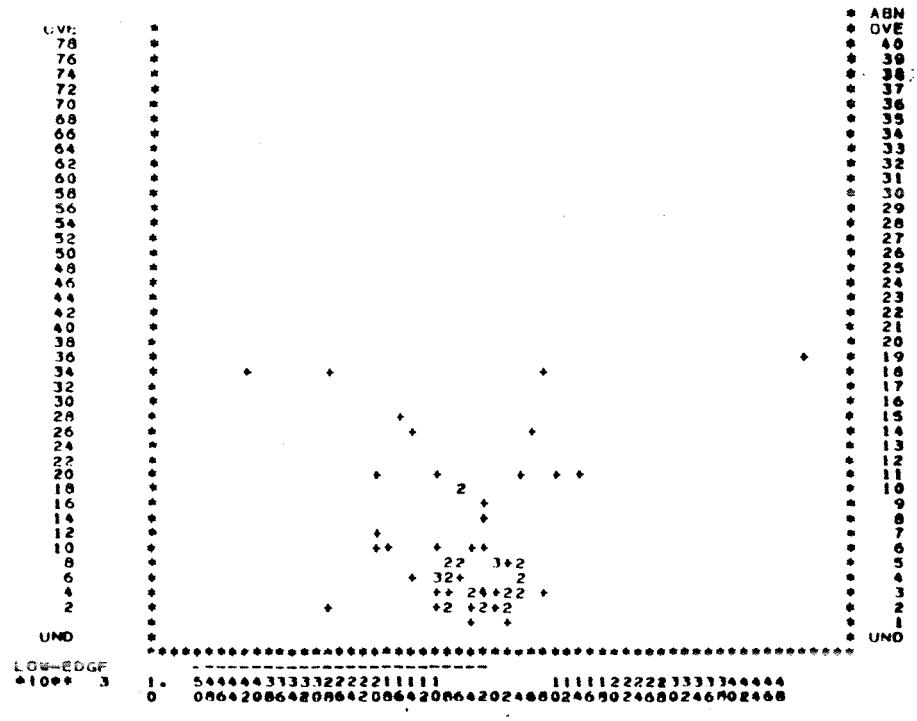

Fig.7.7 Coplanarity factor vs.kinematical chi-squared for π^+-events.

(2.02 amu), and L is the length of the target (100 cm). We arrive at

$$n_{tgt}^{area} = 4.22\times10^{24}\ \frac{1}{cm^2} \qquad (7.4)$$

Because of problems with the event-scalers, we calculate the incoming useful number of particles from the burstscalers, weighted by the livetime fraction which is calculated from a mean value of the ratio eventscalers/burstscalers. There is a probability that the majority veto rejects good events. This has been measured, and we apply an average correction factor of 0.65 to the incoming flux for this effect.

For the inefficiency of C1•C2, we apply a correction factor of 0.95 to the flux.

Then we arrive at the following corrected fluxes for π^+ and π^-, respectively

$$F_{corr}^{+} = 1.509\ \times10^{12}$$
$$F_{corr}^{-} = 0.6673\times10^{12} \qquad (7.5)$$

The correction factor corr contains all other corrections. Two effects tend to make the beam hodoscope count more than the true number of beam particles: the geometrical overlap structure of the planes (see section 4.3.3) and the δ-ray effect. On the other hand, the counter dead-time has an opposite effect. Altogether the correction factor for these effects is estimated to 0.88 [51].

The muon content of the beam, $\mu/\pi \sim 0.06$ (see section 4.3.4), gives rise to a correction of 0.94.

Due to the reactions, the beam intensity decreases along the target. With N_o particles arriving at the target entrance, the number of remaining particles at a length z in the target, is $N(z) = N_o e^{-n\sigma z}$. n is the number of target protons per volume and σ the total inelastic πp cross

section. Thus the mean value of beam particles over the target is

$$\langle N \rangle = \frac{1}{L} \int_0^L N(z)dz = 0.95 \qquad (7.6)$$

We therefore apply a correction factor of 0.95 for this effect.

Likewise interactions in the beam hodoscope will reduce the beam intensity. This gives rise to a correction factor of 0.97.

The H1H2 hodoscopes and the prompts are not sensitive over 100 % of their area. Applying a correction factor of 0.98, we take care of this geometrical efficiency. The mean chamber efficiency is calculated off-line. We arrive at efficiencies of 0.75 when averaged over the data-taking period with positive beam, and 0.80 for the negative beam.

With positive beam, the K^+,p content was measured to be 14%, so we apply a correction factor of 0.86. For negative beam, the K^-,$\bar{p}$ content was about 6%, leading to a correction factor of 0.94.

The factor corr is the product of all the factors mentioned above, and summarised in table 7.3.

Table 7.3 Correction Factors

	Positive beam	Negative beam
Overlap, δ-rays, deadtime in beam hodoscope	0.88	0.88
Interactions in beam hodoscope	0.97	0.97
Interactions in target	0.95	0.95
H1H2 and prompts' geometrical efficiency	0.98	0.98
Muon content in the beam	0.94	0.94
K,p content in the beam	0.86	0.94
Mean chamber efficiency	0.75	0.80

Choosing a bin width of $\Delta t = 2$, we finally arrive at the following expressions for the cross sections

$$\frac{d\sigma}{dt}(\pi^+ p \to \pi^+ p) = 1.618\times10^{-37} \frac{N_{obs}}{acc} \frac{cm^2}{(GeV)^2}$$

$$\frac{d\sigma}{dt}(\pi^- p \to \pi^- p) = 3.186\times10^{-37} \frac{N_{obs}}{acc} \frac{cm^2}{(GeV)^2} \qquad (7.7)$$

The preliminary results for π^- and π^+ elastic scattering are given in tables 7.4 and 7.5.

Table 7.4 WA7 preliminary results for 20 GeV/c $\pi^- p$ elastic scattering

t-bin	N^{obs}	acc	$\frac{d\sigma}{dt}$ $(cm^2/(GeV)^2)$
$6 < t < 8$	8	0.017	$(1.5 \pm 0.5) \times 10^{-34}$
$8 < t < 10$	9	0.048	$(6.0 \pm 2) \times 10^{-35}$
$10 < t < 12$	8	0.071	$(3.6 \pm 1) \times 10^{-35}$
$12 < t < 14$	2	0.084	$(7.6 \pm 5) \times 10^{-36}$
$14 < t < 16$	3	0.093	$(1.0 \pm 0.6) \times 10^{-35}$

Table 7.5 WA7 preliminary results for 20 GeV/c $\pi^+ p$ elastic scattering

t-bin	N^{obs}	acc	$\frac{d\sigma}{dt}$ $(cm^2/(GeV)^2)$
$6 < t < 8$	25	0.025	$(1.6 \pm 0.3) \times 10^{-34}$
$8 < t < 10$	18	0.055	$(5.3 \pm 1) \times 10^{-35}$
$10 < t < 12$	8	0.072	$(1.8 \pm 0.6) \times 10^{-35}$
$12 < t < 14$	12	0.085	$(2.3 \pm 0.7) \times 10^{-35}$
$14 < t < 16$	2	0.075	$(4.3 \pm 3) \times 10^{-36}$
$16 < t < 18$	2	0.010	$(3.2 \pm 2) \times 10^{-35}$

Only the statistical uncertainty on the number of events is included in the tables. Because of the low numbers of events in the bins, this dominates over the uncertainty in normalization.

I figs. 7.8 and 7.9 are shown the cross sections for π^+ and π^-, respec-

tively, together with the predicted curves of the CIM-model. The normalization constant (see section 3.3.2) of the CIM cross sections is for both cases calculated from 10 GeV/c π^+ -data (Lundby, [36]). The agreement with the CIM predictions seems good, but one should stress the preliminary character of the data.

In order to establish the energy dependence of the cross sections, they are integrated over a certain range of t to reduce the uncertainty. According to the dimensional counting rules (see section 3.3.2), the integrated cross section should obey the same energy dependence as the fixed angle cross section itself, provided the region of integration is contained in the wide angle range where dimensional counting is supposed to be valid. We have chosen a region of integration from $\cos\theta_{CM} = 0.20$ to $\cos\theta_{CM} = 0.55$.

The energy dependence for π^-p and π^+p fixed angle elastic scattering is shown in fig. 3.11 on p. 48. The π^- data above 6 GeV/c seem to agree with the dimensional counting rule prediction of an s^{-8} dependence, whereas no safe conclusion may be drawn from the π^+ data.

In order to get a rough estimate of the π^- and π^+ energy dependencies at the highest energies available, the integrated cross sections (as explained above) have been plotted for only two values of s. These are $s = 19.6$ (10 GeV/c Lundby data [36]) and 38.4 (20 GeV/c, this experiment) for π^+, and $s = 19.3$ (9.8 GeV/c Owen data [73]) and 38.4 (20 GeV/c, this experiment) for π^-. See figs. 7.10 and 7.11. It would obviously have been interesting to include the 12 GeV/c π^- data of Bellefon et al. [37] in fig. 7.11, but their π^- data are not presented sufficiently detailed to make the above described integration over our $\cos\theta_{CM}$-region possible.

Assuming an s^{-n} energy dependence, we arrive at $n = 7.0 \pm 0.6$ for π^+ and $n = 8.0 \pm 0.7$ for π^-. The π^- result is clearly consistent with the dimensional counting rule prediction of s^{-8}, whereas the π^+ result

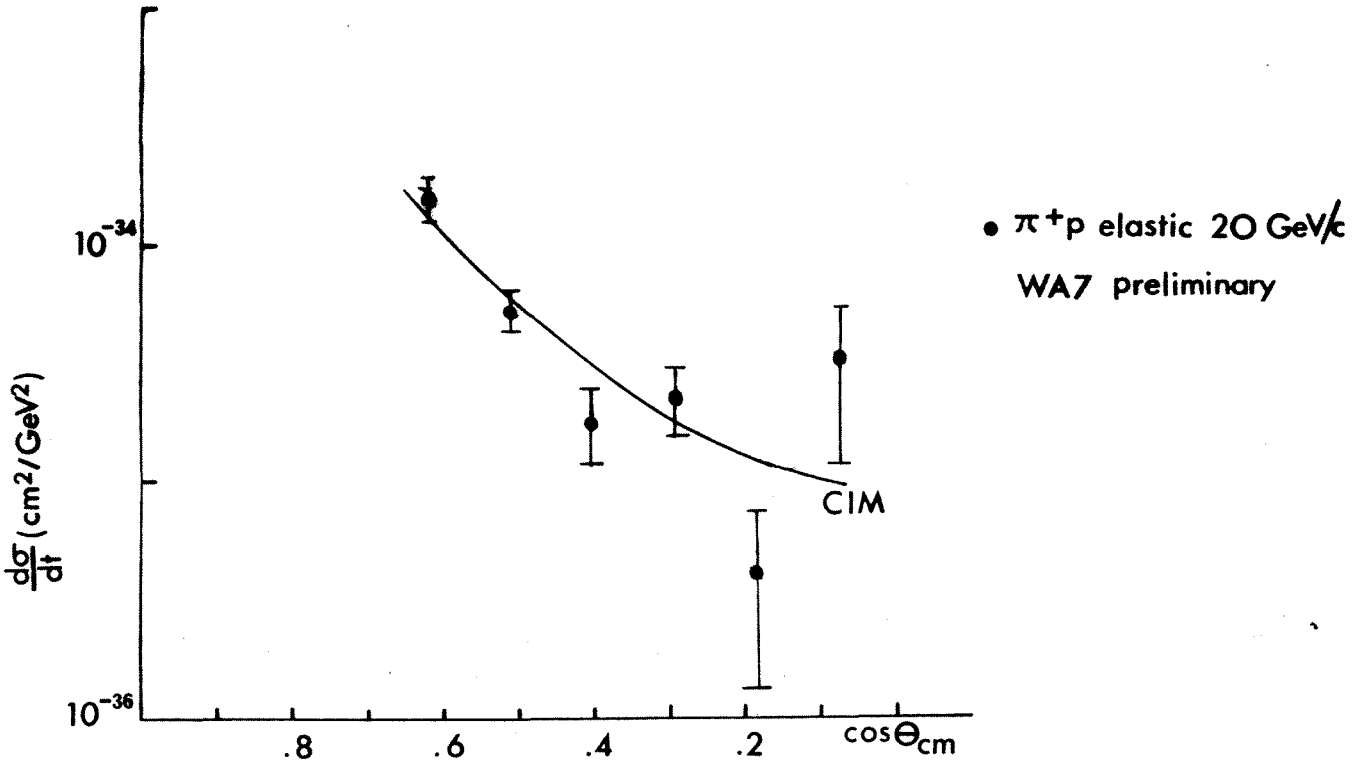

Fig.7.8
WA7 preliminary differential cross section for π^+p elastic scattering compared to CIM prediction.CIM normalization from 10GeV/c π^+-data [36].

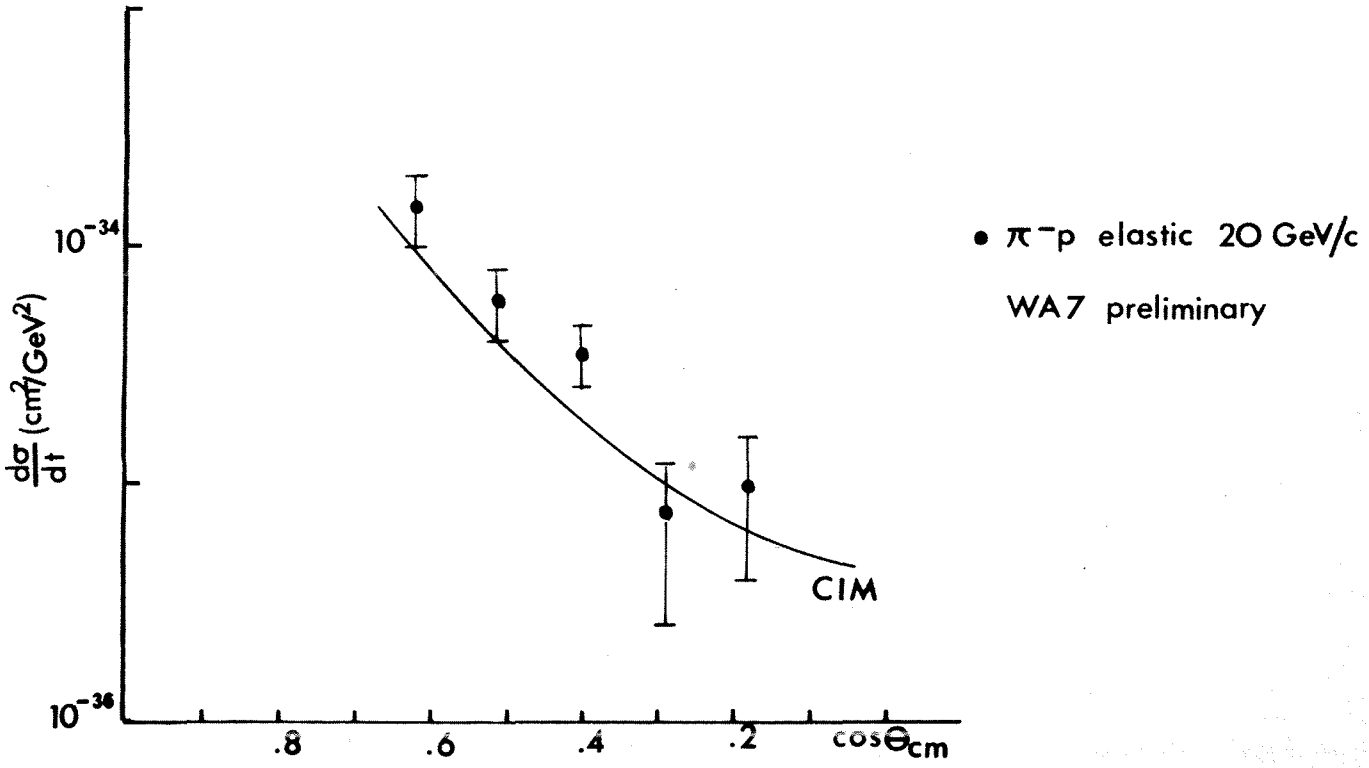

Fig.7.9
WA7 preliminary differential cross section for π^-p elastic scattering compared to CIM prediction.CIM normalization as above.

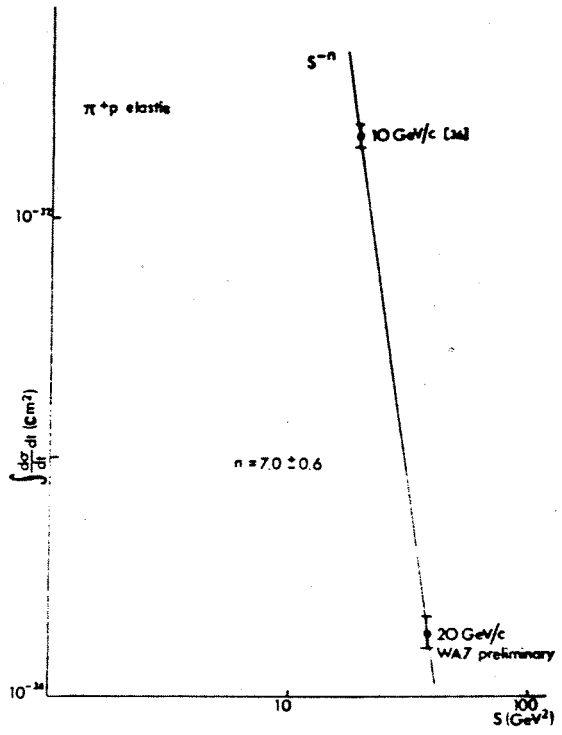

Fig.7.10 Indication of s-dependence for π^+p elastic scattering.

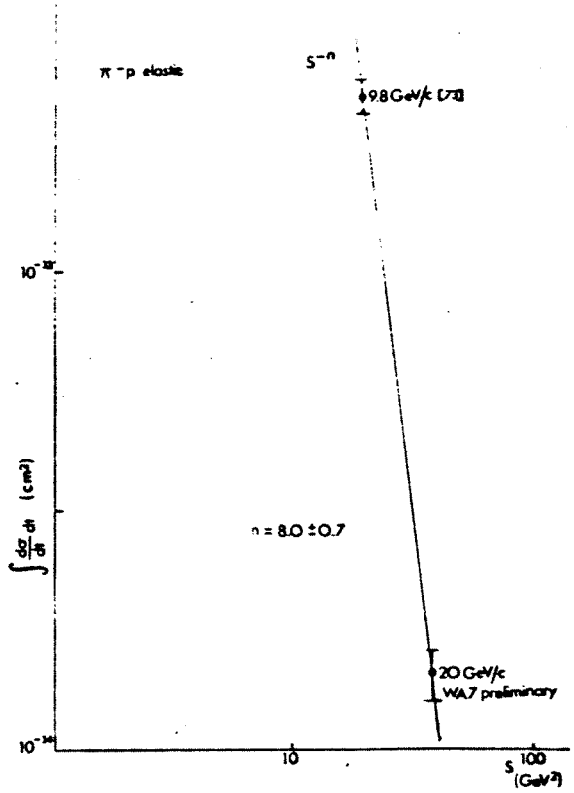

Fig.7.11 Indication of s-dependence for π^-p elastic scattering.

In these figures are plotted elastic cross sections integrated over t-ranges corresponding to $0.20 \leq \cos\theta_{CM} \leq 0.55$. To get an indication of the s-dependence in the asymptotic region where dimensional counting is supposed to work, only the two highest energy data-points available are used. See the text. One should be aware of the possible influence of systematic errors when only two data-points are used.

is not. Whether this will change with a more refined analysis, remains to be seen. One should also be aware of the possible influence of systematical errors when only two data points are used to define the exponent n.

The next step of the experiment is to measure π^- and π^+ elastic scattering at 30 GeV/c. It will be most interesting to see whether the 30 GeV/c data confirm the above results.

APPENDIX I NOTATION AND DEFINITIONS

AI.1 Metric and Four-Vectors

A general four-vector A is written

$$A = (A_1, A_2, A_3; A_4) = (\vec{A}; A_4) \tag{AI.1}$$

Our metric is such that the product of two four-vectors A and B is

$$AB = \vec{A} \cdot \vec{B} - A_4 B_4 \tag{AI.2}$$

AI.2 Units and Kinematics

We use units with

$$\hbar = c = 1 \tag{AI.3}$$

Our unit of energy is GeV. It follows that the units of momentum and mass are GeV/c and GeV/c^2, respectively.

The Mandelstam variables s, t and u for a 2-body reaction ab → cd are defined as follows (see Fig. AI.1), $p_i = (\vec{p}_i; E_i)$ being the four-momentum of particle i

$$\begin{aligned} s &= -(p_a + p_b)^2 = E_{CM}^2 \\ t &= -(p_a - p_c)^2 \\ u &= -(p_a - p_d)^2 \end{aligned} \tag{AI.4}$$

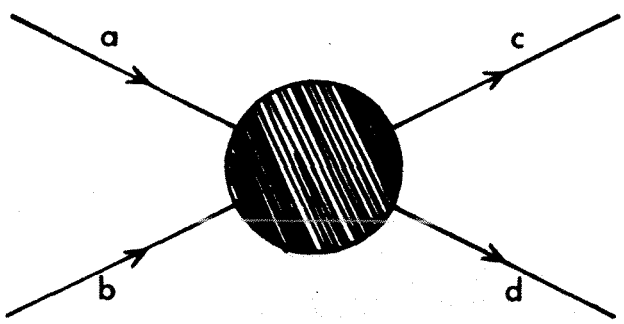

Fig. AI.1 2-body reaction ab → cd

AI.3 Statistics

The probability distribution $f(x)$ of a random variable X is such that the probability of X taking values between x_1 and x_2 is

$$Pr(x_1 \leq X \leq x_2) = \int_{x_1}^{x_2} f(x)dx \qquad (AI.5)$$

We denote the expectation value of X by $\langle X \rangle$ or EX, i.e.

$$\langle X \rangle = EX = \int xf(x)dx \qquad (AI.6)$$

The variance is denoted σ_X^2, X_{rms}^2 or $\mathrm{Var}\ X$, i.e.

$$\sigma_X^2 = X_{rms}^2 = \mathrm{Var}\ X = \int (x - \langle x \rangle)^2 f(x)dx \qquad (AI.7)$$

The standard deviation of the distribution is $\sigma_X = X_{rms}$.

NUCLEAR INSTRUMENTS AND METHODS 160 (1979) 43-48 ; © NORTH-HOLLAND PUBLISHING CO.

A FAST RUNGE–KUTTA METHOD FOR FITTING TRACKS IN A MAGNETIC FIELD

JAN MYRHEIM* and LARS BUGGE*

CERN, Geneva, Switzerland

Received 3 October 1978

Efficient methods for fitting tracks of charged particles in magnetic fields need derivatives of track coordinates with respect to the parameters defining the track. The problem of computing derivatives analytically is solved for a particular Runge–Kutta integration method. This Runge–Kutta fitting method is being used in the off-line analysis of a CERN SPS experiment, where it was developed as an alternative to the quintic spline method. It converges faster than the quintic spline, and is quite comparable with respect to computer speed and precision.

1. Introduction

The different Runge–Kutta integration methods that are being used for tracking charged particles through magnetic fields, in general combine high precision with high speed[1]). These methods are also often used for fitting tracks when high precision is needed, but have then had the disadvantage of being rather slow, because they did not give derivatives of coordinates with respect to the track parameters to be fitted, i.e. the initial values in the integration.

The method described here can be used to compute the required derivatives together with the track coordinates themselves, at the expense of little extra computer time. We have used a Runge–Kutta tracking routine RKPATH written by Wind[2]) and essentially added just a few lines of FORTRAN. The routine has been tested inside a program for track fitting with vertex constraints that has been developed for the CERN SPS experiment WA7[3]), originally based on the quintic spline method[4]).

We first discuss the method, and then we present the results of a few test-runs where we have compared this new Runge–Kutta method and the quintic spline fit. These tests show that the two methods are quite comparable, both with respect to speed and accuracy.

2. Basic equations

The equation of motion for a particle of mass m and charge q in a magnetic field $\boldsymbol{B}$ is

$$\frac{\mathrm{d}\boldsymbol{p}}{\mathrm{d}t} = q\boldsymbol{v}\times\boldsymbol{B} \quad \text{(in MKSA units)}. \tag{1}$$

* Visitors from Physics Institute, University of Oslo, Oslo, Norway.

v is the velocity and

$$p = \frac{mv}{\sqrt{(1-v^2/c^2)}} \tag{2}$$

is the momentum of the particle.

We rewrite eq. (1) in the form

$$u'' = (q/p)\, f(u, u', z), \tag{3}$$

with

$$u = \begin{pmatrix} x \\ y \end{pmatrix}, \qquad f = \begin{pmatrix} f_x \\ f_y \end{pmatrix},$$

$$u' = \frac{\mathrm{d}u}{\mathrm{d}z}, \qquad u'' = \frac{\mathrm{d}^2u}{\mathrm{d}z^2},$$

$$\begin{aligned} f_x &= \sqrt{[1+(x')^2+(y')^2]} \times \\ &\quad \times \{x'y'B_x - [1+(x')^2]\, B_y + y'B_z\}, \\ f_y &= \sqrt{[1+(x')^2+(y')^2]} \times \\ &\quad \times \{[1+(y')^2]\, B_x - x'y'\, B_y - x'B_z\}. \end{aligned} \tag{4}$$

The solution of eq. (3) is determined by the constant of motion

$$\lambda = q/p, \tag{5}$$

and by the initial values at a given $z = z_0$,

$$u(z_0) = \begin{pmatrix} x_0 \\ y_0 \end{pmatrix}, \qquad u'(z_0) = \begin{pmatrix} a \\ b \end{pmatrix}. \tag{6}$$

Given a set of observed coordinates on a track, the problem is to make a fit for the five variables x_0, y_0, a, b and λ. In order to have an efficient iteration procedure for the fit we want the derivatives of $u(z)$ and $u'(z)$ with respect to x_0, y_0, a, b and λ.

If $u(z)$ is the solution with initial values x_0, y_0,

a, b, λ, and $(u+\Delta u)(z)$ is the solution with the perturbed initial values $x_0+\Delta x_0$, $y_0+\Delta y_0$, $a+\Delta a$, $b+\Delta b$, $\lambda+\Delta\lambda$, then we have

$$u'' = \lambda f(u, u', z),$$

$$u(z_0) = \begin{pmatrix} x_0 \\ y_0 \end{pmatrix}, \qquad u'(z_0) = \begin{pmatrix} a \\ b \end{pmatrix}, \tag{7}$$

and

$$u''+\Delta u'' = (\lambda+\Delta\lambda) f(u+\Delta u, u'+\Delta u', z),$$

$$(u+\Delta u)(z_0) = \begin{pmatrix} x_0+\Delta x_0 \\ y_0+\Delta y_0 \end{pmatrix}, \tag{8}$$

$$(u'+\Delta u')(z_0) = \begin{pmatrix} a+\Delta a \\ b+\Delta b \end{pmatrix}.$$

We write

$$\lambda f(u+\Delta u, u'+\Delta u', z)$$
$$= \lambda f(u, u', z) + C(u, u', z)\,\Delta u + A(u, u', z)\,\Delta u', \tag{9}$$

where C and A are 2×2 matrices, for example

$$A = \lambda \frac{\partial f}{\partial u'} = \lambda \begin{pmatrix} \frac{\partial f_x}{\partial x'} & \frac{\partial f_x}{\partial y'} \\ \frac{\partial f_y}{\partial x'} & \frac{\partial f_y}{\partial y'} \end{pmatrix}, \tag{10}$$

and we arrive at the equation for Δu,

$$\Delta u'' = \Delta\lambda f + C\Delta u + A\Delta u' \tag{11}$$

with the initial conditions

$$\Delta u(z_0) = \begin{pmatrix} \Delta x_0 \\ \Delta y_0 \end{pmatrix}, \qquad \Delta u'(z_0) = \begin{pmatrix} \Delta a \\ \Delta b \end{pmatrix}. \tag{12}$$

The general solution for the perturbation Δu is

$$\Delta u(z) = \Delta\lambda\, L(z) + N(z)\,\Delta u(z_0) + M(z)\,\Delta u'(z_0), \tag{13}$$

where L is a 2×1 matrix, N and M are 2×2 matrices, and

$$L'' = f + CL + AL',$$
$$L(z_0) = 0,\ L'(z_0) = 0, \tag{14}$$

$$N'' = CN + AN',$$

$$N(z_0) = I = \begin{pmatrix} 1 & 0 \\ 0 & 1 \end{pmatrix}, \qquad N'(z_0) = 0, \tag{15}$$

$$M'' = CM + AM',$$

$$M(z_0) = 0,\ M'(z_0) = I. \tag{16}$$

From eq. (13) we read out the required derivatives,

$$\frac{\partial u(z)}{\partial\lambda} = L(z), \qquad \frac{\partial u'(z)}{\partial\lambda} = L'(z),$$

$$\frac{\partial u(z)}{\partial u(z_0)} = \begin{pmatrix} \frac{\partial x(z)}{\partial x_0} & \frac{\partial x(z)}{\partial y_0} \\ \frac{\partial y(z)}{\partial x_0} & \frac{\partial y(z)}{\partial y_0} \end{pmatrix} = N(z),$$

$$\frac{\partial u'(z)}{\partial u(z_0)} = N'(z),$$

$$\frac{\partial u(z)}{\partial u'(z_0)} = M(z) \tag{17}$$

$$\frac{\partial u'(z)}{\partial u'(z_0)} = M'(z).$$

When fitting a vertex between several tracks we need, in addition, the derivatives with respect to z_0. However, these can be computed from the above derivatives, because a solution with initial values x_0, y_0, a, b, λ at $z = z_0 + \Delta z_0$ is the same as a solution with initial values

$$x_0 - a\Delta z_0,$$

$$y_0 - b\Delta z_0,$$

$$a - \lambda f_x(x_0, y_0, a, b, z_0)\,\Delta z_0, \tag{18}$$

$$b - \lambda f_y(x_0, y_0, a, b, z_0)\,\Delta z_0,$$

and λ at z_0. Therefore,

$$\frac{\partial u(z)}{\partial z_0} = -a\frac{\partial u(z)}{\partial x_0} - b\frac{\partial u(z)}{\partial y_0}$$
$$-\lambda f_x(x_0, y_0, a, b, z_0)\frac{\partial u(z)}{\partial a} \tag{19}$$
$$-\lambda f_y(x_0, y_0, a, b, z_0)\frac{\partial u(z)}{\partial b},$$

and similarly for $\partial u'(z)/\partial z_0$.

In principle we ought to solve the eqs. (14), (15) and (16) together with eq. (3). What we do in practice, however, is to define an approximation to the solution of eq. (3) and compute the derivatives within this approximation.

3. Runge–Kutta integration

The particular Runge–Kutta formula used is due to Nyström[5]). The step from z_n to $z_{n+1} = z_n + h$ is

$$u_{n+1} = u_n + hu'_n + \frac{h^2}{6}(K_1+K_2+K_3), \tag{20}$$

$$u'_{n+1} = u'_n + \frac{h}{6}(K_1 + 2K_2 + 2K_3 + K_4),$$

where

$K_i = \lambda f_i \quad$ for $\quad i = 1, 2, 3, 4,$,

$f_1 = f(u_n, u'_n, z_n)$,

$$f_2 = f\left(u_n + \frac{h}{2}u'_n + \frac{h^2}{8}K_1, u'_n + \frac{h}{2}K_1, z_n + \frac{h}{2}\right), \tag{21}$$

$$f_3 = f\left(u_n + \frac{h}{2}u'_n + \frac{h^2}{8}K_1, u'_n + \frac{h}{2}K_2, z_n + \frac{h}{2}\right),$$

$$f_4 = f\left(u_n + hu'_n + \frac{h^2}{2}K_3, u'_n + hK_3, z_n + h\right).$$

Differentiating these formulae with respect to, say, x_0, we get recursion formulae for the derivatives $\partial u(z)/\partial x_0$ and $\partial u'(z)/\partial x_0$,

$$\frac{\partial u_{n+1}}{\partial x_0} = \frac{\partial u_n}{\partial x_0} + h\frac{\partial u'_n}{\partial x_0} + \frac{h^2}{6}\frac{\partial}{\partial x_0}(K_1+K_2+K_3),$$

$$\frac{\partial u'_{n+1}}{\partial x_0} = \frac{\partial u'_n}{\partial x_0} + \frac{h}{6}\frac{\partial}{\partial x_0}(K_1 + 2K_2 + 2K_3 + K_4), \tag{22}$$

where

$$\frac{\partial K_1}{\partial x_0} = C_1\frac{\partial u_n}{\partial x_0} + A_1\frac{\partial u'_n}{\partial x_0},$$

$$\frac{\partial K_2}{\partial x_0} = C_2\left(\frac{\partial u_n}{\partial x_0} + \frac{h}{2}\frac{\partial u'_n}{\partial x_0} + \frac{h^2}{8}\frac{\partial K_1}{\partial x_0}\right) + A_2\left(\frac{\partial u'_n}{\partial x_0} + \frac{h}{2}\frac{\partial K_1}{\partial x_0}\right).$$

$$\frac{\partial K_3}{\partial x_0} = C_3\left(\frac{\partial u_n}{\partial x_0} + \frac{h}{2}\frac{\partial u'_n}{\partial x_0} + \frac{h^2}{8}\frac{\partial K_1}{\partial x_0}\right) + A_3\left(\frac{\partial u'_n}{\partial x_0} + \frac{h}{2}\frac{\partial K_2}{\partial x_0}\right), \tag{23}$$

$$\frac{\partial K_4}{\partial x_0} = C_4\left(\frac{\partial u_n}{\partial x_0} + h\frac{\partial u'_n}{\partial x_0} + \frac{h^2}{2}\frac{\partial K_3}{\partial x_0}\right) + A_4\left(\frac{\partial u'_n}{\partial x_0} + h\frac{\partial K_3}{\partial x_0}\right).$$

We have written

$A_1 = A(u_n, u'_n, z_n)$,

$$A_2 = A\left(u_n + \frac{h}{2}u'_n + \frac{h^2}{8}K_1, u'_n + \frac{h}{2}K_1, z_n + \frac{h}{2}\right),$$

$$A_3 = A\left(u_n + \frac{h}{2}u'_n + \frac{h^2}{8}K_1, u'_n + \frac{h}{2}K_2, z_n + \frac{h}{2}\right), \tag{24}$$

$$A_4 = A\left(u_n + hu'_n + \frac{h^2}{2}K_3, u'_n + hK_3, z_n + h\right),$$

and similarly for C_1, C_2, C_3 and C_4.

For the derivatives with respect to y_0, a and b we get similar formulae. When differentiating with respect to λ, we get similar formulae except for one extra term f_i in the formula for K_i, thus

$$\frac{\partial K_1}{\partial \lambda} = f_1 + C_1\frac{\partial u_n}{\partial \lambda} + A_1\frac{\partial u'_n}{\partial \lambda},$$

$$\frac{\partial K_2}{\partial \lambda} = f_2 + C_2\left(\frac{\partial u_n}{\partial \lambda} + \frac{h}{2}\frac{\partial u'_n}{\partial \lambda} + \frac{h^2}{8}\frac{\partial K_1}{\partial \lambda}\right) + A_2\left(\frac{\partial u'_n}{\partial \lambda} + \frac{h}{2}\frac{\partial K_1}{\partial \lambda}\right). \tag{25}$$

etc.

4. A useful approximation

We will assume that the x and y partial derivatives of the magnetic field components are all zero along the track,

$$\frac{\partial B_i}{\partial x} = \frac{\partial B_i}{\partial y} = 0, \quad \text{for} \quad i = x, y, z, \tag{26}$$

implying that

$$C = \lambda\,\partial f/\partial u = 0. \tag{27}$$

This is a good approximation in many cases, and it simplifies considerably the above formulae.

Thus, if we write out in detail eq. (25) we now get

$$\frac{\partial K_1}{\partial \lambda} = f_1 + A_1\frac{\partial u'_n}{\partial \lambda},$$

$$\frac{\partial K_2}{\partial \lambda} = f_2 + \frac{h}{2}A_2 f_1 + A_2\left(I + \frac{h}{2}A_1\right)\frac{\partial u'_n}{\partial \lambda},$$

$$\frac{\partial K_3}{\partial \lambda} = f_3 + \frac{h}{2}A_3\left(f_2 + \frac{h}{2}A_2 f_1\right) + A_3\left[I + \frac{h}{2}A_2\left(I + \frac{h}{2}A_1\right)\right]\frac{\partial u'_n}{\partial \lambda}, \tag{28}$$

$$\frac{\partial K_4}{\partial \lambda} = f_4 + hA_4\left[f_3 + \frac{h}{2}A_3\left(f_2 + \frac{h}{2}A_2 f_1\right)\right] + A_4\left\{I + hA_3\left[I + \frac{h}{2}A_2\left(I + \frac{h}{2}A_1\right)\right]\right\}\frac{\partial u'_n}{\partial \lambda}.$$

The recursion step for $\partial u/\partial\lambda$ and $\partial u'/\partial\lambda$ now

takes the following form:

$$\frac{\partial u_{n+1}}{\partial\lambda} = \frac{\partial u_n}{\partial\lambda} + h\frac{\partial u'_n}{\partial\lambda} + \frac{h^2}{6}\frac{\partial}{\partial\lambda}(K_1+K_2+K_3)$$

$$= \frac{\partial u_n}{\partial\lambda} + h\frac{\partial u'_n}{\partial\lambda} + \tag{29}$$

$$+\frac{h}{3}\left[\frac{h}{2}A_3+\frac{h}{2}A_1 + \left(I+\frac{h}{2}A_3\right)\frac{h}{2}A_2\left(I+\frac{h}{2}A_1\right)\right]\frac{\partial u'_n}{\partial\lambda} +$$

$$+\frac{h^2}{6}\left[f_3+f_1+\left(I+\frac{h}{2}A_3\right)\left(f_2+\frac{h}{2}A_2 f_1\right)\right],$$

$$\frac{\partial u'_{n+1}}{\partial\lambda} = \frac{\partial u'_n}{\partial\lambda} + \frac{h}{6}\frac{\partial}{\partial\lambda}(K_1+2K_2+2K_3+K_4)$$

$$= \left\{\frac{1}{3}\left(I+\frac{h}{2}A_4+\frac{h}{2}A_1\right) + \tag{30}\right.$$

$$+\frac{2}{3}\left[I+\left(I+\frac{h}{2}A_4\right)\frac{h}{2}A_3\right]\times$$

$$\left.\times\left[I+\frac{h}{2}A_2\left(I+\frac{h}{2}A_1\right)\right]\right\}\frac{\partial u'_n}{\partial\lambda} +$$

$$+\frac{h}{6}\left\{f_4+f_1+2\left(I+\frac{h}{2}A_4\right)f_3 + \right.$$

$$\left.+2\left[I+\left(I+\frac{h}{2}A_4\right)\frac{h}{2}A_3\right]\left(f_2+\frac{h}{2}A_2 f_1\right)\right\}.$$

The formulae for the derivatives with respect to x_0, y_0, a and b are similar to eqs. (29) and (30), with the only difference that they do not contain the terms with f_1, f_2, f_3 and f_4.

5. Test results

We have made some test runs using alternatively the Runge–Kutta method or the quintic spline fit as part of the off-line analysis chain of the elastic scattering experiment WA7 [6]). The tests were made both with Monte Carlo generated elastic events and with real non-elastic events, fitting two outgoing tracks with vertex constraints. On our Monte Carlo elastic data we also imposed the momentum conservation constraints. All data relate to an incident π^- beam at 20 GeV/c.

Running on Monte Carlo data we used the Monte Carlo generated coordinates with no generated errors; this was therefore a test of the accuracy of the two methods. We used weights corresponding to measurement errors of 0.5 mm in all coordinates and the first iteration was started from perturbed values for the Monte Carlo generated vertex position and momenta. We added to the correct values perturbations of ± 3 cm in x and y of the vertex, ± 15 cm in z of vertex, ± 0.05 in dx/dz and dy/dz of the two tracks at vertex, and $\pm 20\%$ in the momenta.

Running on real data we have used weights corresponding to errors of 2 mm in single detector planes. The question of whether or not these weights are correct, should not be important for the comparison between the two methods. The starting point for the first iteration on a real event was the vertex position and momenta given as output from the pattern recognition program.

We incorporated a convergence test, which was that the "step squared" in one iteration should be less than 0.01. Let Δ_i be the weighted residual in the ith measured coordinate after a given number of iterations, then at that stage in the fitting process the approximate value for χ^2 is, assuming independent measurements,

$$\chi^2 = \sum_i \Delta_i^2. \tag{31}$$

If after the next iteration, the weighted residuals are Δ'_i, we define the step length by

$$(\text{step})^2 = \sum_i (\Delta'_i - \Delta_i)^2. \tag{32}$$

This is the most natural measure of how much the parameters to be fitted are changed during one iteration.

In order to get an idea of the relative speed and precision of the two methods, we used them in such a way that they computed the magnetic field at nearly the same points. That is, we used steps in z of 25 cm for the Runge–Kutta integration, and 12.5 cm for the quintic spline fit.

Of 500 Monte Carlo generated elastic events all converged from the perturbed event variables back to the correct values, giving a χ^2 of effectively zero. Out of a sample of 1000 real triggers with altogether 1113 candidates for two-prong vertices, many vertices failed to give a fit, for different reasons. The Runge–Kutta method finally made a fit for 813 vertices, whereas the quintic spline fitted 798 vertices. We do not consider this 2% difference to be very significant, however, since many vertices have an ill-defined z-coordinate because the two tracks are nearly parallel at the vertex, and these vertices may cause convergence problems.

TABLE 1
Execution times (ms/event).

	Runge–Kutta	Quintic spline
Monte-Carlo data (6 iterations, no convergence test)	146	138
Monte-Carlo data (stop after convergence)	121	123
Real data (ms/input vertex, $\leqslant 8$ iterations, with convergence test)	126	123
Real data (same run, ms/fitted vertex)	173	172

6. Execution times

Table 1 summarizes the results of our timing on an IBM 370 computer, under the different conditions.

We should add a few remarks. We have used a magnetic field routine requiring 0.126 ms for one call, and for 6 iterations on Monte Carlo data the total time spent in computing the field was 34 ms/event for either program. In addition, in the quintic spline fit, before the first iteration a Runge–Kutta tracking was done in order to define starting values for coordinates and derivatives, and this tracking required about 15 ms/event, including 11 ms/event for computing field values.

Thus, both methods could be speeded up somewhat by a more efficient representation of the magnetic field, in discrete planes only, and by not computing the field in every iteration. Also, a more efficient method for defining first approximations could save some time for the quintic spline fit.

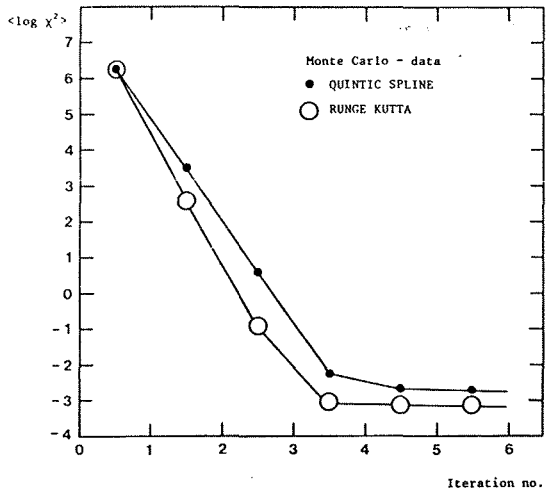

Fig. 1. Mean of $\log \chi^2$ before iteration 1, 2, 3, ... for 500 Monte Carlo events.

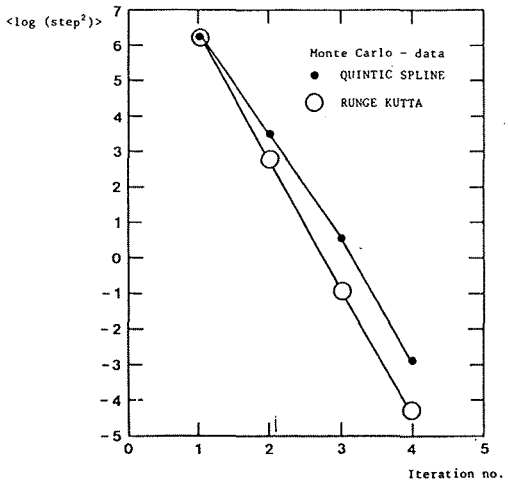

Fig. 2. Mean of log (step^2) in iteration 1, 2, 3, ... for the same Monte Carlo events.

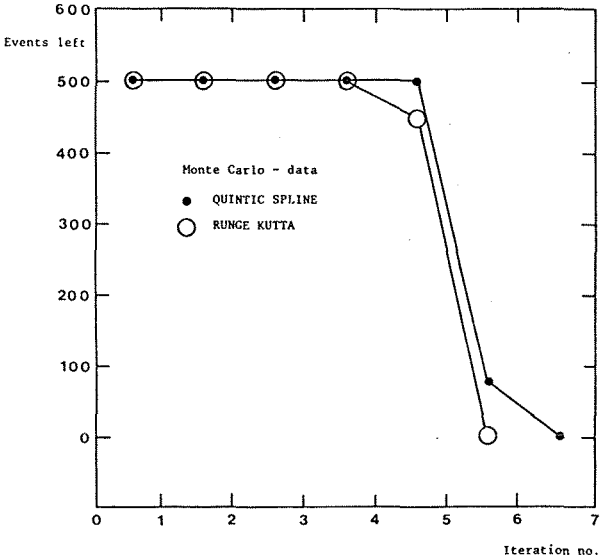

Fig. 3. Number of events passed on from iteration $n-1$ to iteration n, $n = 1, 2, 3, \ldots$, Monte Carlo data.

7. Convergence properties

We have also compared the convergence of the two methods, and the results are shown in figs. 1–3 for Monte Carlo data and in figs. 4–6 for real data.

Figs. 1 and 4 show the mean of the logarithm (to base 10) of the approximation to χ^2, after $0, 1, 2, \ldots$ iterations. Figs. 2 and 5 show the mean of the logarithm of the "step squared" in iteration

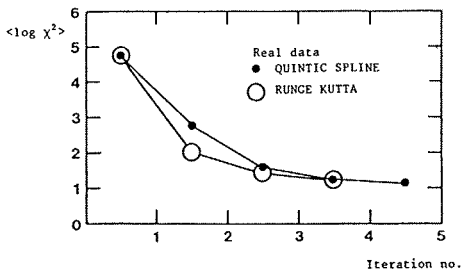

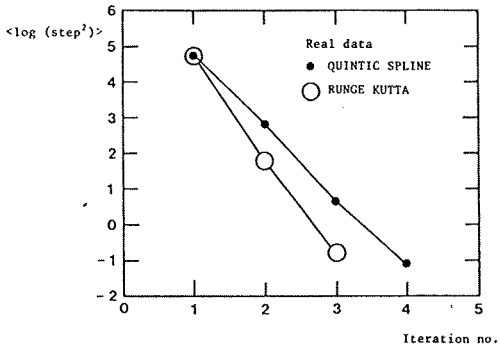

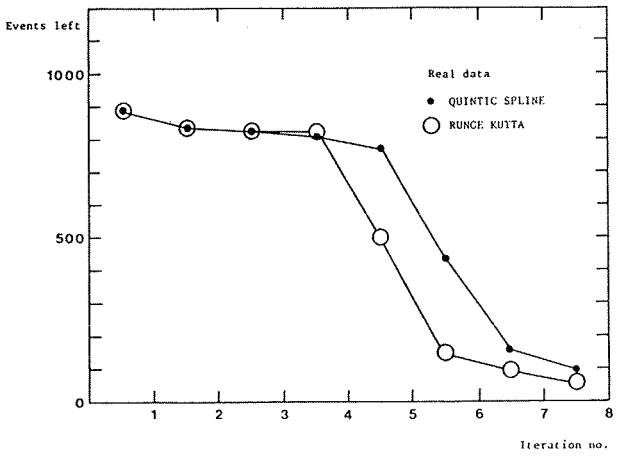

Figs. 4–6. The same as figs. 1–3, but for real data.

1, 2, 3, ... Finally, figs. 3 and 6 show the number of events left after 0, 1, 2. ... iterations, when the convergence test is applied. On real data, events are sometimes cut out during the fitting, not because they have converged, but because they diverge in some way or other (tracks pass outside boundaries of the magnetic field, etc.). Thus the convergence test starts cutting the number of events only in the fourth iteration.

8. Conclusion

From the test we have done, using fixed steps through the magnetic field, it appears that the Runge–Kutta method spends somewhat more time per iteration, but on the other hand it is more precise and converges faster than the quintic spline method. If both methods are optimised to give a certain precision with a minimum of time spent in computing values of the magnetic field, one method or the other might be the most efficient, depending on which one of the effects mentioned turns out to be the most important one.

We therefore conclude that the present Runge–Kutta method can compete with the quintic spline fit, not only in precision, but also in speed.

References

[1] M. G. Shiel, Internal Note CERN/DD 75-22.
[2] CERN Program Library, algorithm S4101.
[3] R. K. Böck, WA7 Internal Note ELAS 77.
[4] H. Wind, Nucl. Instr. and Meth. **115** (1974) 431.
[5] National Bureau of Standards Handbook, procedure 25.5.20.
[6] Study of Exclusive Hadronic Processes at large p_T, CERN/SPSC 74-28 (P-9) and CERN/SPSC 74-49 (P-9, Add. 1) (March/April 1974).

APPENDIX II A FAST RUNGE-KUTTA METHOD FOR FITTING TRACKS IN A MAGNETIC FIELD.

APPENDIX III ON A FIT WITH CORRELATED ERRORS.

01.11.78

L. Bugge

On a Fit with Correlated Errors

A usual approximation in least squares fitting procedures, is to assume the (measurement-) error matrix diagonal, i.e. to neglect any correlations between the measurement errors. This is, however, only an approximation, because the parts of the measurement errors in the various measurement planes that are due to Coulomb scattering, are clearly correlated.

Nevertheless, the little investigation on this problem described below seems to justify such an approximation, at least for amounts of Coulomb scattering comparable to the ones treated here.

The Fit

We want to parametrize the m measurements x_i, $i = 1, \ldots, m$ with the m functions f_i, $i = 1, \ldots, m$ which are functions of the $n(< m)$ parameters ξ_α, $\alpha = 1, \ldots, n$. In vector notation:

$$f = f(\xi) \tag{1}$$

We define the m residues δ_i, $i = 1, \ldots, m$ by

$$\delta = x - f(\xi) \tag{2}$$

The matrix of derivatives, D, is defined by

$$D_{i\alpha} = \frac{\partial f_i}{\partial \xi_\alpha} \tag{3}$$

In general f is not linear in ξ, but we may linearize it by setting

$$f(\xi + \Delta\xi) = f(\xi) + D\Delta\xi \tag{4}$$

We then define the weight matrix W as the inverse of the error matrix Σ:

$$W = \Sigma^{-1} \tag{5}$$

In a case where all the correlations between measurement errors are neglected, Σ is diagonal with the m squared measurement errors σ_i^2, $i = 1, \ldots, m$ along the diagonal.

The least squares fit consists of finding the set ξ which minimizes the sum of squares (T denotes transpose):

$$s^2 = \delta^T W \delta \tag{6}$$

This leads to the following equations for the corrections $\Delta\xi$ to ξ :

$$D^T W D \Delta\xi = D^T W \delta \tag{7}$$

Because of the linearization (4) one usually has to iterate.

In the diagonal case W can be written as $W_{ij} = w_i^2 \delta_{ij}$ with $w_i^2 = \frac{1}{\sigma_i^2}$, $i = 1, \ldots, m$. By simply multiplying the w_i's into the D-matrix, setting $D_{i\alpha} = \frac{\partial f_i}{\partial \xi_\alpha} w_i$, we can forget about W, solving instead the equations

$$D^T D \Delta\xi = D^T \delta \tag{8}$$

In this way one may save a fair amount of computer time.

When Coulomb scattering is taken into account, the total Σ-matrix can be written as the sum

$$\Sigma = \Sigma^C + \Sigma^D \tag{9}$$

where Σ^D is a diagonal error matrix containing uncorrelated measurement errors (σ_i^2, $i = 1, \ldots, m$ along the diagonal), and Σ^C contains errors with correlations from Coulomb scattering.

The Σ^C-matrix

In the following, $\langle Z \rangle$ will denote the expectation value of the variable Z.

If generally ε_i denotes the contribution to x_i which is due to Coulomb scattering, we have:

$$\Sigma^C_{ij} = \langle \varepsilon_i \cdot \varepsilon_j \rangle - \langle \varepsilon_i \rangle \cdot \langle \varepsilon_j \rangle = \langle \varepsilon_i \cdot \varepsilon_j \rangle \qquad (10)$$

To construct Σ^C the following assumptions are made:

(i) The Coulomb scattering is assumed to take place in discrete planes.

(ii) The tracks are treated as straight ones and the scattering angles are regarded as small ones, in the sense that the deviation ε at a z-position z resulting from Coulomb scattering an angle θ_i^{proj} in the proper projection at a z-value z_i is

$$\varepsilon = (z - z_i)\theta_i^{proj} \qquad (11)$$

(iii) The projected (in some plane) Coulomb scattering angle from one unit (target, chamber, hodoscope, ...) is taken to be Gaussian distributed around zero with variance

$$\text{Var}\ \theta_{proj} = \langle \theta^2_{proj} \rangle = \left(\frac{0.015}{p.\beta}\right)^2 (1 + \varepsilon)^2 \sum_{\text{materials}} \frac{L_k}{L^0_k} \ (\text{radians})^2 \qquad (12)$$

where p is momentum in GeV/c, β velocity in units of c, and L_k, L^0_k is traversed length, radiation length for material no. k of the unit. ε is a constant taken to be $\varepsilon = 0.1$.

Let then

$$u_i = x_i \cos\alpha_i + y_i \sin\alpha_i \qquad (13)$$

be a measured coordinate in a measurement plane at $z = z_i$. (u_i might be x,y,u,v in WA7.)

For the error in u_i from Coloumb scattering, ε_{u_i}, we can write

$$\varepsilon_{u_i} = \varepsilon_{x_i} \cos\alpha_i + \varepsilon_{y_i} \sin\alpha_i \qquad (14)$$

According to (11) we have, when ε'_{x_i} (ε'_{y_i}) denotes error from Coulomb scattering on measured direction $\frac{dx}{dz}$ ($\frac{dy}{dz}$), the following relations:

$$\varepsilon_{x_i} = \sum_{\ell} (z_i - z_\ell)\theta_\ell^{x\text{-proj}}$$

$$\varepsilon_{y_i} = \sum_{\ell} (z_i - z_\ell)\theta_\ell^{y\text{-proj}}$$

$$\varepsilon'_{x_i} = \sum_{\ell} \theta_\ell^{x\text{-proj}}$$

$$\varepsilon'_{y_i} = \sum_{\ell} \theta_\ell^{y\text{-proj}}$$

where the sums extend over all scattering planes

We use this and the fact that Coulomb scattering i
x- and y-projections are independent processes and
(in any projection) from different scatterers are
the expectation $<\varepsilon_{u_i}>$ equals zero. When we in a
$<\theta_i^{x\text{-proj}^2}> = <\theta_i^{y\text{-proj}^2}> = <\theta_i^2>$, we arrive at the
the elements $\Sigma^C_{k\ell}$ which correspond to the covaria
coordinates :

$$\Sigma^C_{k\ell} = <\varepsilon_{u_k} \cdot \varepsilon_{u_\ell}> = \sum_i (z_k - z_i)(z_\ell - z_i)(\cos\alpha_k \cos\alpha_\ell +$$

where the sum extends over all scattering planes
of k,ℓ.

For the covariance between measured coordinate and

$$\Sigma^C_{k\ell} = <\varepsilon_{u_k} \cdot \varepsilon'_{u_\ell}> = \sum_i (z_k - z_i)(\cos\alpha_k \cos\alpha_\ell + \sin\alpha_k \sin\alpha$$

And finally for the covariance between two measured

$$\Sigma^C_{k\ell} = <\varepsilon'_{u_k} \cdot \varepsilon'_{u_\ell}> = \sum_i (\cos\alpha_k \cos\alpha_\ell + \sin\alpha_k \sin\alpha_\ell)<\theta_i^2>$$

For the beam we neglect the Coulomb scattering cont
ment errors.

Applications on Monte Carlo data for WA7

A few very simple tests have been made to get a rough feeling of how the quality of the fit depends on the use of a fit as described in the previous section.

Geometrical fit

Elastic $\pi^- p$ events at 20 GeV/c beam momentum were generated with three different amounts of Coulomb scattering. In all three cases the events in addition to Coulomb scattering were given Gaussian distributed, uncorrelated measurement errors, corresponding to the σ_i^2's on the diagonal of Σ^D.

The Coulomb scattering was generated as described in ELAS 119, except that scattering after the hodoscope was neglected (because of the reference plane at z = 400 cm).

Case I corresponds to an amount of Colulomb-scattering in the six scattering planes as given in Table 2, ELAS 119 . In cases II and III the six scattering constants are multiplied by factors 2.5, 5.0 respectively.

For each of the three cases the events were fitted twice, once with a fit with correlations as described in the previous paragraph, and once with a diagonal fit where Coulomb scattering is totally neglected. The fits were purely geometrical, with no use of kinematical constraints.

In each case the variances of the distributions

$$d_i = \xi_i^{\text{fitted}} - \xi_i^{\text{MC}} \quad , i = 1, \ldots, n$$

are computed. ξ_i^{MC} denotes the exact Monte Carlo generated value of the parameter ξ_i .

In the WA7 case $n = 12$ and the 12 fitted parameters ξ are x,y,z of vertex and $\frac{dx}{dz}$, $\frac{dy}{dz}$, $|\vec{p}|$ at vertex for the three tracks (two outgoing and beam).

The values of the ratio between the computed variances of d_i, $i = 1, \ldots, 9$

(the beam track is not affected by Coulomb scattering) for the diagonal fit (index D) and the fit with correlations (index C), $\frac{\sigma^2_D}{\sigma^2_C}$, are given together with their uncertainties (see the Addendum) in Table 1. Also the value of $\frac{\langle\chi^2\rangle_D}{\langle\chi^2\rangle_C}$ which is a quantitative measure of the amount of Coulomb scattering, is given in the table.

Table 1 $\frac{\sigma^2_D}{\sigma^2_C}$ for different cases (see text).

	VARIABLE NO									Case (see text)	$\frac{\langle\chi^2\rangle_D}{\langle\chi^2\rangle_C}$
	1	2	3	4	5	6	7	8	9		
$\frac{\sigma^2_D}{\sigma^2_C}$	0.98	0.95	0.95	1.02	1.05	0.98	0.97	1.19	0.97	I	1.02
RMS	0.10	0.10	0.10	0.10	0.11	0.10	0.10	0.12	0.10		
$\frac{\sigma^2_D}{\sigma^2_C}$	1.00	1.16	1.11	1.07	1.31	1.02	1.12	1.91	1.08	II	1.13
RMS	0.10	0.12	0.11	0.11	0.13	0.10	0.11	0.19	0.11		
$\frac{\sigma^2_D}{\sigma^2_C}$	1.04	2.02	1.75	1.33	1.78	1.30	1.73	3.04	1.48	III	1.53
RMS	0.10	0.20	0.18	0.13	0.18	0.13	0.17	0.30	0.15		
$\frac{\sigma^2_{DI}}{\sigma^2_C}$	1.03	0.90	1.12	1.12	1.22	1.12	1.06	1.72	0.92	III	1.53
RMS	0.10	0.09	0.11	0.11	0.12	0.11	0.11	0.17	0.09		

From the table we see that variables 2 (y_{vtx}), 5 ($dy/dz^{(1)}_{vtx}$) and 8 ($dy/dz^{(2)}_{vtx}$) seem to benefit most from taking the Coulomb scattering into account.

However, most of the benefit comes from the fact that the correlation fit gives a better estimate of the measurement errors and not from the off-diagonal-elements of Σ^C. This can be seen from the last two rows in table 1 which are obtained for case III. Here the errors σ_i in the

diagonal fit have been increased an amount corresponding to the diagonal elements of Σ^C (index DI).

We see that it is only variable no. 8 (dy/dz at vertex for arm 2) which benefits significantly from the non-diagonal terms of Σ^C even when the amount of Coulomb scattering is five times the normal WA7 case.

However, it is (for case III) large differences in the mean of chi-squared for the three fits. These are given in Table 2.

Table 2 Mean of χ^2 for three different fits (CASE III).

	THEORETICAL VALUE	FIT WITH CORRELATIONS	DIAGONAL FIT, COULOMB SCATT.NEGL.	DIAGONAL FIT INCR.DIAG.ELEM.
$<\chi^2>$	17.00	17.9	27.4	12.8
#EVENTS	∞	328	497	500

We see that for case III the fit with correlations is the only one which gives an approximately correct value of $<\chi^2>$.

Filtering of inelastic events

Another test was made to see whether a fit with correlations is better than a diagonal one to filter out inelastic events.

Elastic events and $\Delta(1236)$ events (where scattered π and decay p simulate elastic reaction) were generated at 20 GeV/c beam momentum. All the events were given uncorrelated measurement errors as in the previous section and Coulomb scattering corresponding to the normal WA7 case (case I).

Again the events were fitted twice, once with Coulomb scattering neglected and once with a fit with correlations. In all cases the elastic constraints were applied (elimination method).

Table 3 gives numbers of lost elastic events and accepted inelastic ones for the given cuts in chi-squared, and we see that inside statistics no difference is observed when the cuts are chosen properly.

Table 3 Lost elastics and accepted inelastics

FIT	CUT χ^2	LOST ELAST.	# EVENTS	%	ACCTED INEL.	# EVENTS	%
DIAGONAL	> 50	6	500	1.2	6	500	1.2
WITH CORRELTIONS	> 42	4	365	1.1	3	295	1.0

Conclusion

The conclusion which can be drawn from these small tests is that for WA7 it is not worth it to take Coulomb scattering into account in the track fitting. However, in cases where the Coulomb scattering becomes very large (comparable to case III or larger), one must seriously consider to use a time consuming fitting procedure with non -diagonal error matrix.

ADDENDUM

Uncertainty in the estimate of the quotient of two variances

Let d_i $i = 1, \ldots, n$ be n independent variables, each Gaussian distributed with variance σ^2.

An estimate for σ^2 is

$$S^2 = \sum_{i=1}^{n} \frac{(d_i - \bar{d})^2}{n - 1} \tag{A1}$$

where

$$\bar{d} = \sum_{i=1}^{n} \frac{d_i}{n}$$

The variance of S^2 is given by

$$\text{Var } S^2 \equiv \sigma^2_{S^2} = \frac{2\sigma^4}{n-1} \tag{A2}$$

which gives a relative uncertainty for S^2 :

$$\frac{\sigma_{S^2}}{S^2} = \sqrt{\frac{2}{n-1}} \tag{A3}$$

We shall also use that if F is a function of the independent, Gaussian variables u,v with variances σ^2_u, σ^2_v respectively, the relative error in F is approximately given by

$$\frac{\sigma_F}{F} = \sqrt{\left(\frac{\partial F}{\partial u}\,\sigma_u\right)^2 + \left(\frac{\partial F}{\partial v}\,\sigma_v\right)^2} \tag{A4}$$

Let then S_1^2 and S_2^2 be estimators for the variances σ_1^2 and σ_2^2 of two independent distributions as in (A1), with n_1 and n_2 measurements respectively.

For n_1 and n_2 large, one can take S_1^2 and S_2^2 to be Gaussian distributed. One then gets from (A3) and (A4) for the relative uncertainty in the estimate for σ_1^2/σ_2^2 :

$$\frac{\sigma_{S_1^2/S_2^2}}{S_1^2/S_2^2} = \sqrt{\frac{2}{n_1 - 1} + \frac{2}{n_2 - 1}} \qquad \text{(A5)}$$

Typical values of n_1 and n_2 in the tests described here, are $n_1 = 500$, $n_2 = 350$.

This gives a relative error

$$\frac{\sigma_{S_1^2/S_2^2}}{S_1^2/S_2^2} \approx 0.1$$

APPENDIX IV SOME MONTE CARLO APPLICATIONS

AIV.1 Monte Carlo Generation of ψ-production

It is intended to use the WA7 experiment to study the production of heavy mesons which decay into muon pairs. Special interest focuses on the ψ-meson of 3.1 GeV. The ψ is described as a bound state of a charm and an anticharm quark in the quark model.

The production mechanism of ψ is not very well known. This is one of the reasons why it is interesting to study ψ-production on a hydrogen target.

In 1976 some Monte Carlo calculations were performed in order to roughly study the possibilities of using WA7 to such investigations. The three-body process

$$\pi p \rightarrow \bar{D}\ \psi\ C \qquad \text{(AIV.1)}$$

was generated, $\bar{D}$ being a (anti-) charmed meson and C a charmed baryon. Masses of $M_{\bar{D}} = 2.5$ GeV and $M_C = 3$ GeV were supposed. (At that time no hadrons with "naked" charm were observed). As in [72] the following cascades were generated:

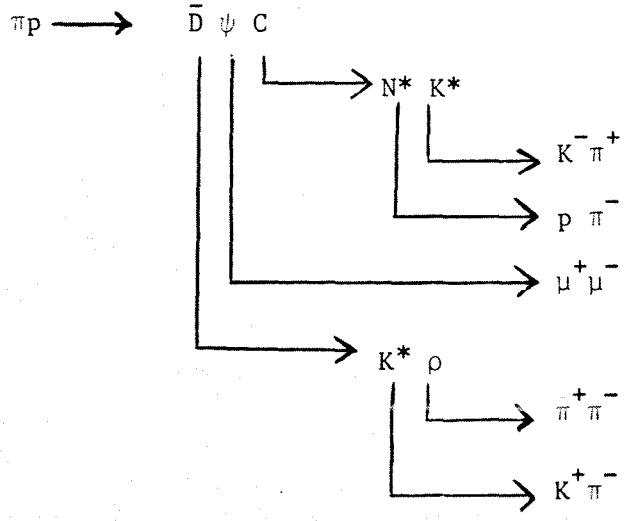

(AIV.2)

Transverse and longitudinal momentum of the ψ was generated in accordance to the then known experimental distributions (see [72] and references therein).

The longitudinal component of the momentum of ψ, $P_L(\psi)$, was computed as

$$P_L(\psi) = \frac{1}{2}\sqrt{s}\, x_L(\psi) \qquad \text{(AIV.3)}$$

where $x_L(\psi)$ was generated according to the following distribution :

$$x_L(\psi) \text{ uniformly on } [-0.6, 0.6]$$

$$x_L(\psi) \sim e^{-5|x_L(\psi)|} \text{ on } [-1, -0.6] \cup [0.6, 1] \qquad \text{(AIV.4)}$$

The transverse momentum of ψ, $P_T(\psi)$, was generated as

$$P_T^2(\psi) \sim e^{-P_T^2(\psi)} \qquad \text{(AIV.5)}$$

In addition the transverse component of the $\bar{D}$-momentum was generated according to a $e^{-6P_T(\bar{D})}$ distribution whereas the azimuthal angles for $\bar{D}$ and ψ were generated uniformly on $[0, 2\pi]$.

The longitudinal $\bar{D}$-momentum and all the parameters for the C then follow from energy-momentum conservation.

The decays were generated isotropic in the rest system of the appropriate particle, and the 4-momenta of the decay products were Lorentz transformed back to the lab. system. Thus, for example, the K^+ momentum needed three transformations:

1. From the rest system of K^* to the rest system of $\bar{D}$.
2. From the rest system of $\bar{D}$ to the $\bar{D}\,\psi\,C$ CM-system.
3. From the $\bar{D}\,\psi\,C$ CM-system to lab.

All the ten final state particles were traced from the same vertex.

If one is only interested in tracing the two muons, one may speed up the programme considerably by generating the ψ-momentum according to (AIV.4) and (AIV.5), and neglecting the $\bar{D}$ and C.

If this is done, and the acceptance criterion is that the two muons should go one in each arm through all MWPCs, hodoscopes and the calorimeters, one arrives at an integrated acceptance of $\sim$ 11% for 20 GeV/c lab momentum and $\sim$ 55% for 92 GeV/c lab momentum.

We will not go further into this matter here, since the primary subject of this thesis is elastic scattering, and since at the time of writing no runs have been performed exclusively concentrating on taking muon data.

AIV.2 Triggering on small t events at 20GeV/c.

TRIGGING ON SMALL T EVENTS AT 2oGeV/c.

The cross section for $\pi p \to \pi p$ exhibit an exponential-like behaviour for small $|t|$,($|t| \lesssim 1.$).In spite of the low acceptance in this t-domain (see below),one will therefore expect a large number of such small-t events.It might therefore be of interest to use such events for testing of apparatus and experimental arrangement.
We have monte-carlo-generated events with small $|t|$,and have found an acceptance of about 0.5% in the domain $|t| \epsilon [.06,.36]$.
By acceptance we here understand the probability that both the scattered π and the recoiling proton escape through the magnet.
Figs.1,2 show the plots of the generated and accepted t-values.
Fig.3 shows a typical low-t event.
The distribution of scattered π's (with the recoil proton escaping through the magnet) in a plane at z=1250.cm.and the corresponding distribution of non-scattered π's(the beam),are shown in figs.4,5 and 6.As one can see,are the scattered π's clearly separated from the beam at this distance from the magnet,and trigging should in principle not be difficult.
We suggest a trigger counter covering the area of the scattered π hits,that is about 1/8 of the total azimuth,placed at about z=1250.cm.

Trigger rates.

The integrated elastic cross section over our t-domain is roughly speaking 2.5 mb,that is about 1/10 of the total cross section at this energy.With a low-intensity beam of about 10^5 particles/burst one should expect about 10^4 reactions in a lm. target,of which about 10^3 should be elastic events in our t-domain.As mentioned before,the distribution of the elastically scattered π's with the corresponding proton escaping through the magnet,covers about 1/8 of the total azimuth,and one should therefore expect roughly 120 triggers from elastic scattering per burst with a trigger as suggested.
Taking into account inelastic events,one should expect the number of particles traversing this counter to increase by roughly a factor 8,i.e. about 1000.
To get rid of as much as possible of inelastic triggers,we would suggest the following trigger-system:

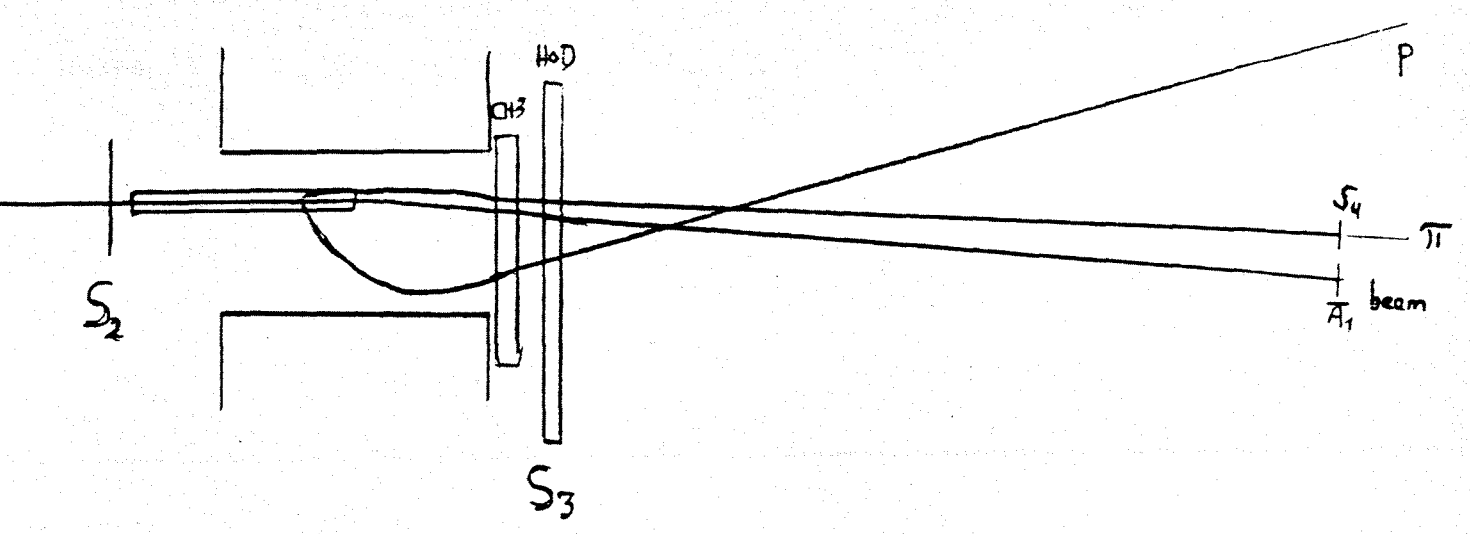

S_3 requires one and only one particle counted (the proton), since the scattered π will go in the beam. $\overline{A}_1$ is an anticounter in the beam. An elastic trigger should then be $S_1S_2S_3S_4\overline{A}_1$.
To get rid of even more of the inelastic triggers, we suggest that instead of using counters S_4 and $\overline{A}_1$ one uses the pr.hod. 1 in the following way:

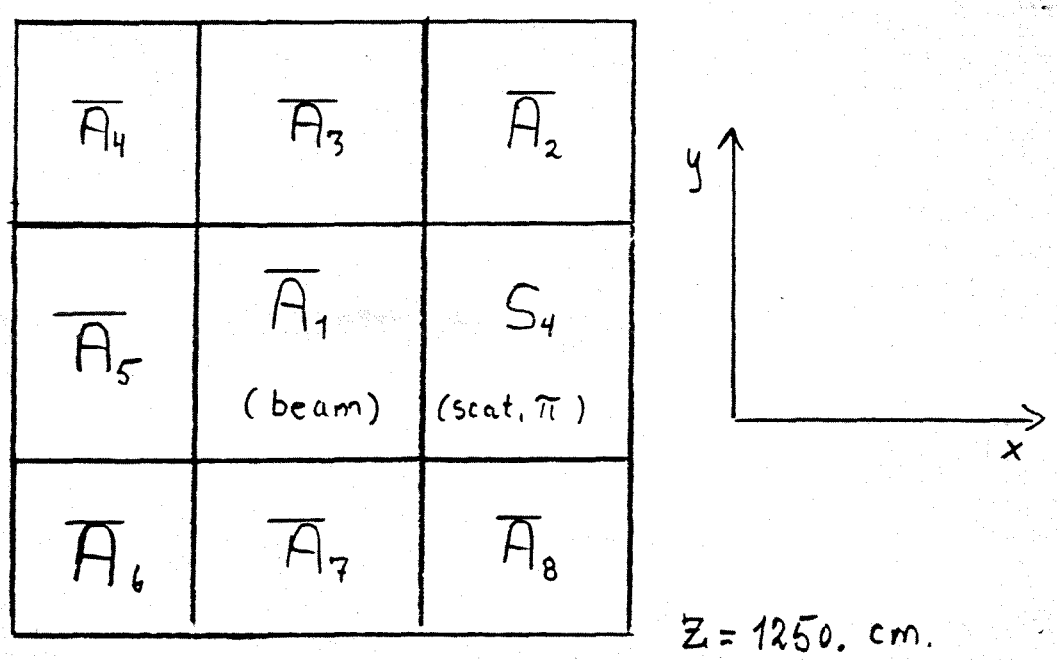

An elastic event would then look like

$$S_1S_2S_3S_4\overline{A}_1\overline{A}_2\overline{A}_3\overline{A}_4\overline{A}_5\overline{A}_6\overline{A}_7\overline{A}_8.$$

Roar Almaas.
Lars Bugge.

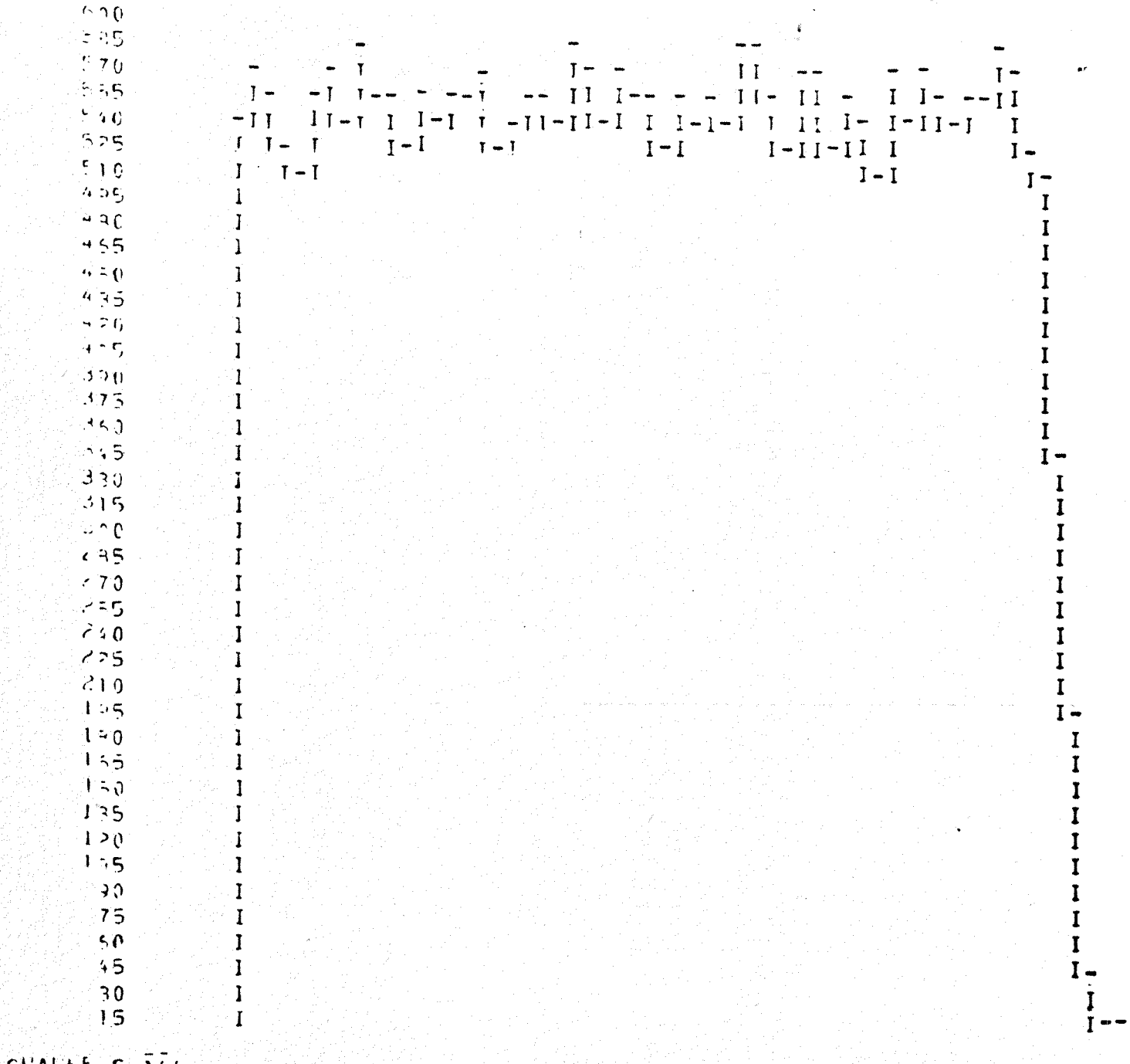

Fig. 1

t generated flat from 0. to 0.6

30000 entries.

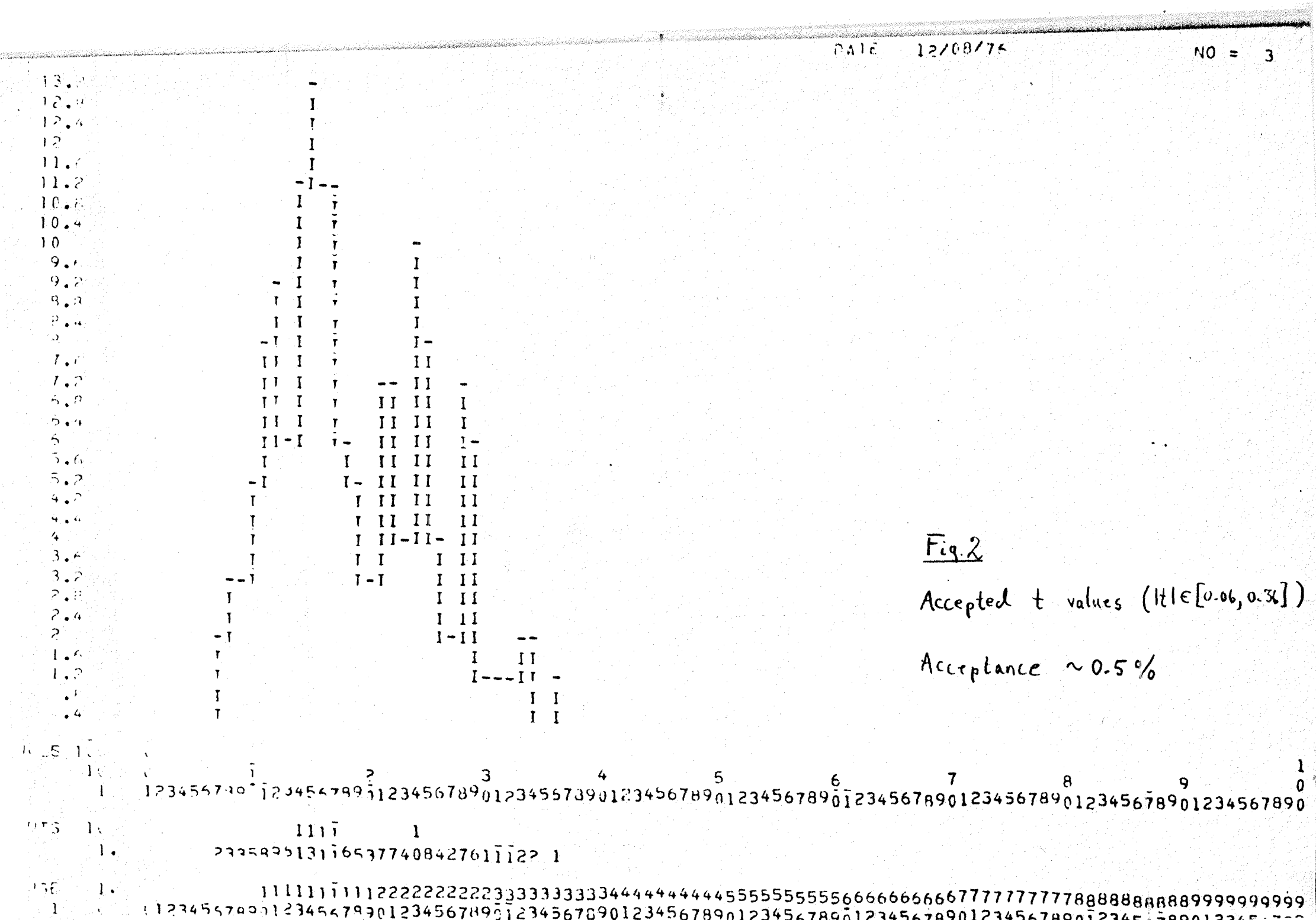

Fig.2

Accepted t values ($|t| \in [0.06, 0.3]$)

Acceptance $\sim 0.5\,\%$

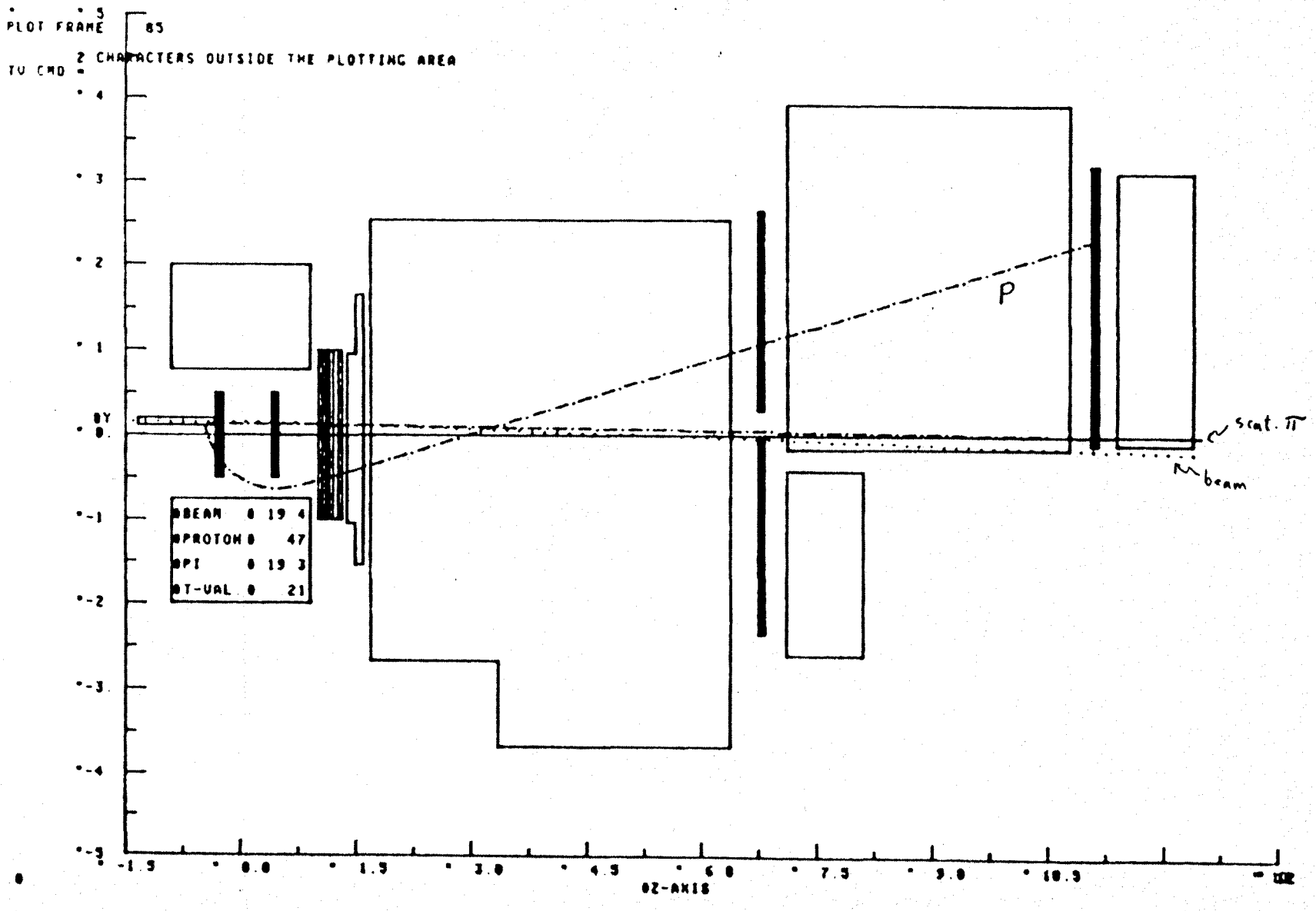

Fig 3.

Typical low t event

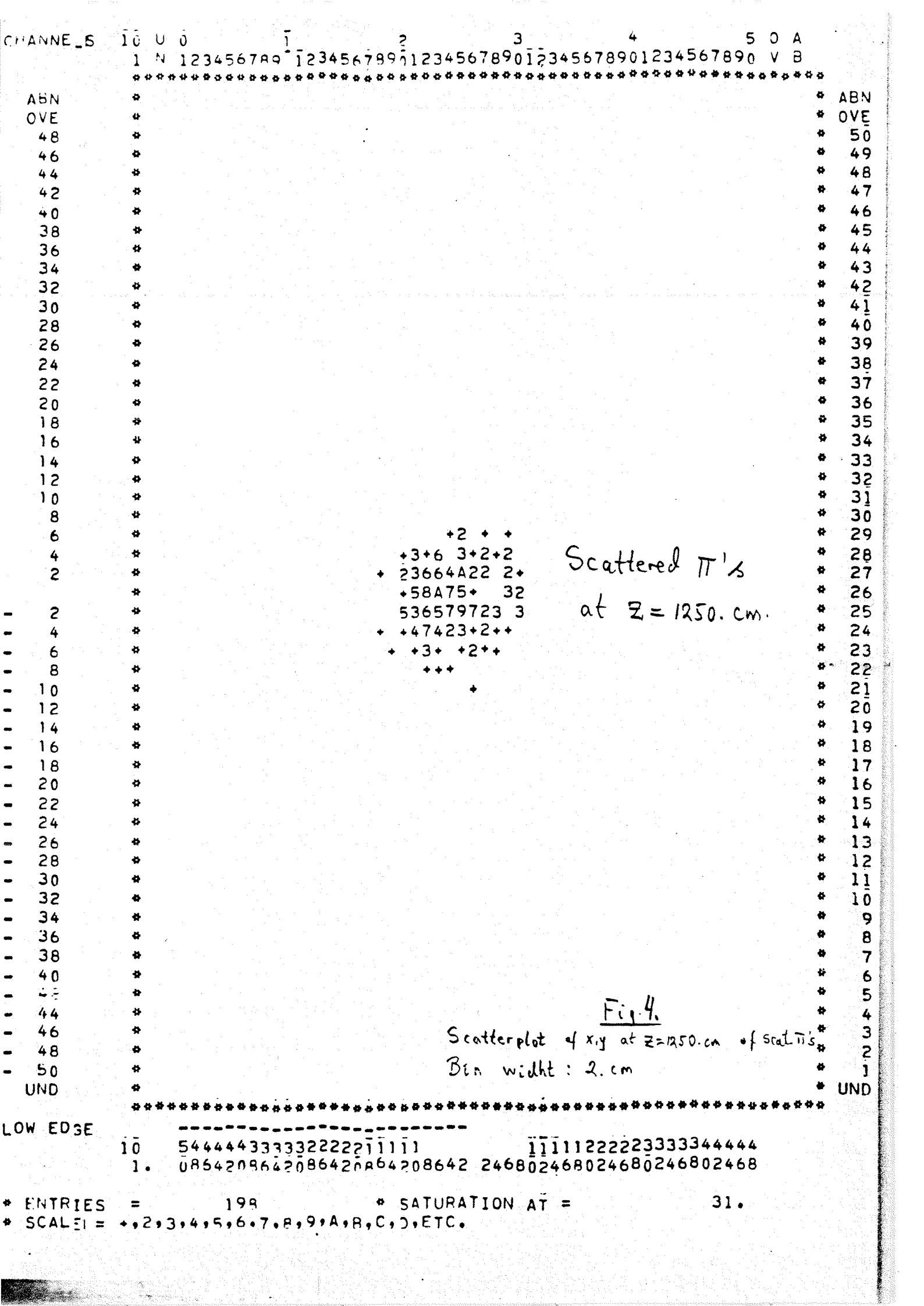

Fig. 4.

Scatterplot of x,y at Z=1250. cm of scat π's
Bin width : 2. cm

* ENTRIES = 198 * SATURATION AT = 31.
* SCALE = +,2,3,4,5,6,7,8,9,A,B,C,D,ETC.

-Y-PLAN22

BOOK ID = A DAT

CHANNELS 10 U 0 1 2 3 4 5 O A
1 N 1234567890123456789012345678901234567890 V B

Beam at Z=1250. cm.

Fig 5.

Scatterplot of x,y at Z=1250. cm. of the beam.

Bin widht: 2. cm.

W EDGE
10 5444443333222211111 1111122222333334444
1. 0864209642086420864208642 2468024680246802468024680

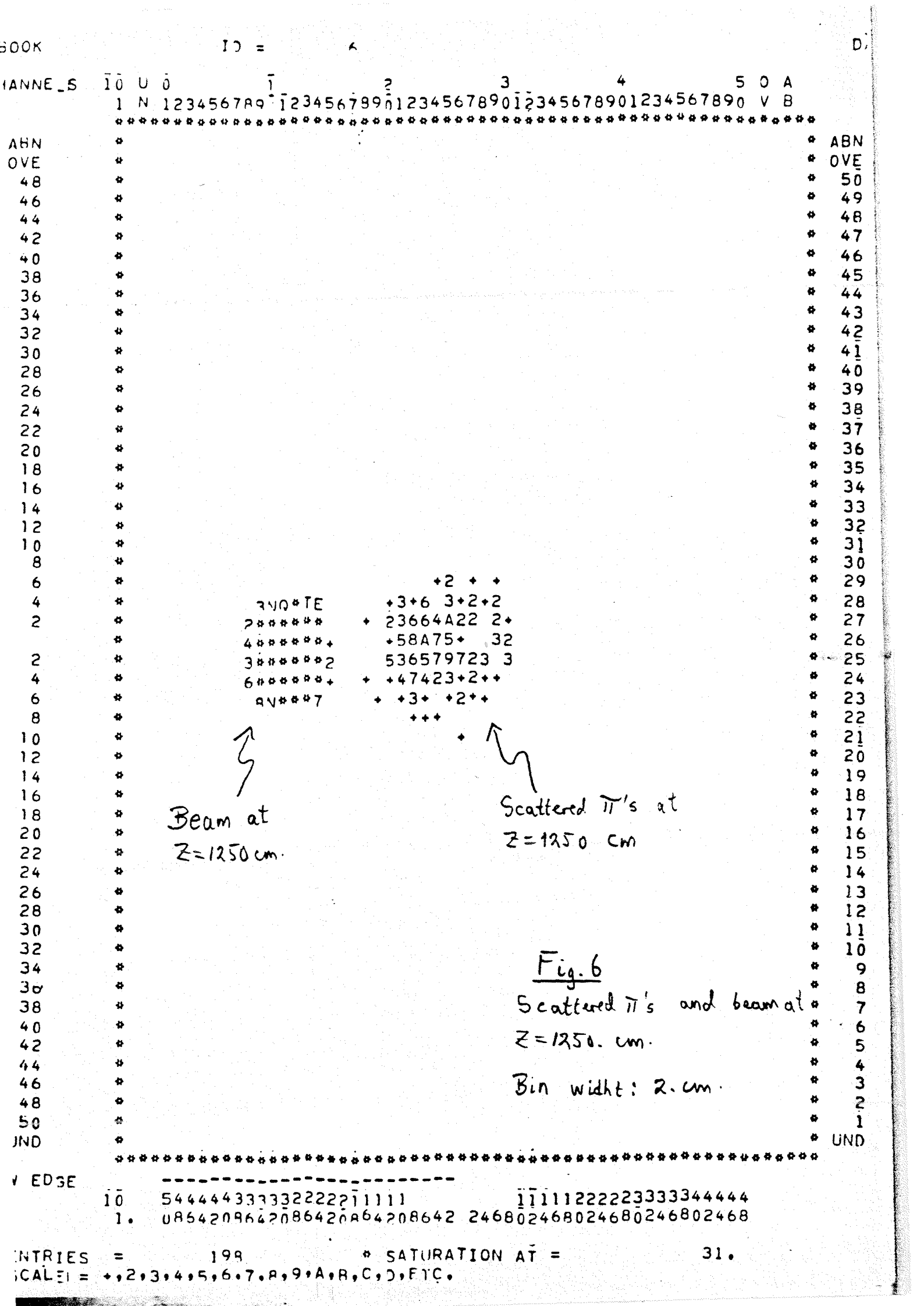

Fig. 6

Scattered π's and beam at Z=1250. cm.

Bin widht: 2. cm.

APPENDIX V MULTIPLE SCATTERING IN WA7 AT 20 GeV/c.

28.09.78
Lars Bugge.

Multiple Scattering in WA7 at 20 Gev/c.

Some Monte Carlo calculations concerning multiple scattering are made for π^--beam at 20 Gev/c incident momentum. Deviations of the order of 0.5 cm are found in the down-stream chambers.
The results are summarized in table 3.

Method.

The projected multiple scattering angle of a particle with momentum p (Gev/c), velocity β (in units of c) and charge 1 (in units of e) after having traversed a length x in a material with radiation length x_0, is taken to be Gaussian distributed around zero with r.m.s. value

$$\theta = \frac{0.015}{p \cdot \beta}\sqrt{\frac{x}{x_0}}\,(1+\varepsilon) \qquad \text{radians} \qquad (1)$$

(the assumption of a Gaussian distribution is not correct, the formula is only correct to within 20% if x is not large compared to x_0) For ε we have chosen a value of 0.1. See refs.1 and 2.
If a unit, for instance a chamber, consists of N different materials, each of thickness x_i and radiation length x_{0_i}, the r.m.s. of the total projected scattering angle is given by

$$\theta = \frac{0.015}{p \cdot \beta}\sqrt{\sum_{i=1}^{N}\frac{x_i}{x_{0_i}}}\,(1+\varepsilon) \qquad \text{radians} \qquad (2)$$

The modification of the direction of a track is done as follows:
Let the track have original diredtion $\underline{A}$ ($|\underline{A}|=1$). A plane is generated perpendicular to $\underline{A}$. Two (uncorrelated) projected scattering angles θ_1 and θ_2 are generated according to (2) and these are used to give the track its new direction by generating two perpendicular vectors $\underline{du}$ and $\underline{dv}$ in the plane mentioned above with magnitudes θ_1 and θ_2 respectively. The new direction $\underline{A'}$ is given by

$$\underline{A'} = \underline{A} + \underline{du} + \underline{dv} \qquad (3)$$

as shown in fig.1.

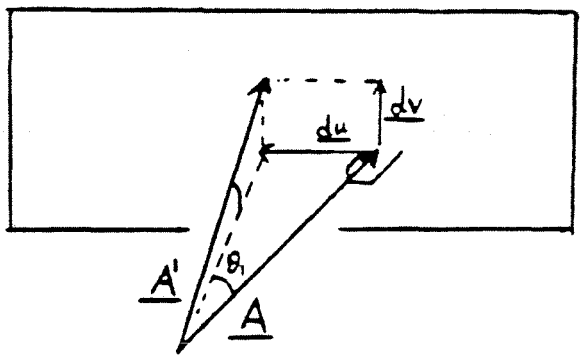

Fig 1.Modification of track direction.

Each time a scatterer is passed,the direction is changed according to (3) before the tracking continues.
For each scatterer the scattering is assumed to take place in a single scattering plane in the middle of the scatterer.This may seem to be a crude approximation,but dividing for example a Čerenkov into several scatterers didn't give significantly different results.
With Čerenkov fillings as in table 1,we arrive at the values of $\sum \frac{x_i}{x_{0_i}}$ for the different units as given in table 2,where also the used z-positions of the scattering planes can be found.In the table L means left arm (CH5) and R means right arm (CH6).
In the chambers mylar windows and planes,tungsten wires and magic gas are taken into account.The wires are assumed to be smeared out to thin foils.
In the Čerenkovs gas,mylar windows and plexiglass mirrors are taken into account.
The target is treated specially for each event.The distance traversed in hydrogen and mylar walls and the intersection with the wall are calculated for each track in a straight line approximation.The scattering plane for hydrogen scattering is taken to be half way (in z) between the vertex and target wall intersection,whereas the scattering plane for mylar scattering is taken to be z of the intersection point.
For 300 accepted events the distances traversed in target hydrogen for the two arms are histogrammed in figs.2 and 3.The acceptance criterion was: π in the left arm,all chamber planes,H1H2 and both prompts hit.(Parameters as for june run.)
It should be noted that the values of $\sum \frac{x}{x_0}$ in table 2 will be increased by the fact that the tracks are not parallell to the z-axes.This is

Results.

Each track is tracked twice - with and without generation of multiple scattering. For accepted events the differences between x-hits in the chambers with and without multiple scattering, Δx, are histogrammed. The r.m.s. values of these distributions are given in table 3. Statistics are 300 accepted events. The Δx distributions in CH5 and CH6 are shown in figs. 4 and 5 respectively. Since the pattern recognition and track fitting programs condense the straight line information to a point and a direction in a reference plane at z=400 cm, it is of interest to see how these numbers are influenced by multiple scattering. This is shown in fig.s 6 and 7 where respectively the Δx and $\Delta dx/dz$ distributions in the reference plane are shown.

References.

1. Particle Properties, April 1971, p.47.
2. W.H. Barkas and A.H. Rosenfeld, UCRL-8030 Rev. (1961) 11.

Table 1. Čerenkov fillings and radiation lengths(cm).

Cerenkov	1	2	3	4
Gas	N_2	Freon12	Freon12	CO_2
Rad. length (cm)	30400.	4810.	4810.	20210.

Table 2. z-positions and $\sum \frac{x}{X_0}$ for the scatterers in the two arms.

Arm	Scatterer	Z	$\sum \frac{x}{X_0}$
L,R	Target hyd.	Vertex dep.	Vertex dep.
L,R	Target walls	Vertex dep.	Vertex dep.
L,R	CH1	-36.3	4.3×10^{-3}
L,R	CH2	-0.2	3.1×10^{-3}
L,R	CH3	114.5	5.4×10^{-3}
L,R	H1H2	143.0	46.6×10^{-3}
L	Č1	500.0	28.2×10^{-3}
L	CH4	694.4	4.3×10^{-3}
L	Č2	900.0	89.6×10^{-3}
R	Č3	250.0	46.0×10^{-3}
R	Č4	550.0	27.5×10^{-3}

Table 3. R.m.s.of Δx distributions in the chambers(mm)

Chamber	CH1	CH2	CH3	CH4	CH5	CH6
R.m.s.of Δx distrib.(mm)	0.16	0.24	0.60	2.70	4.82	4.34

HBOOK ID = 401

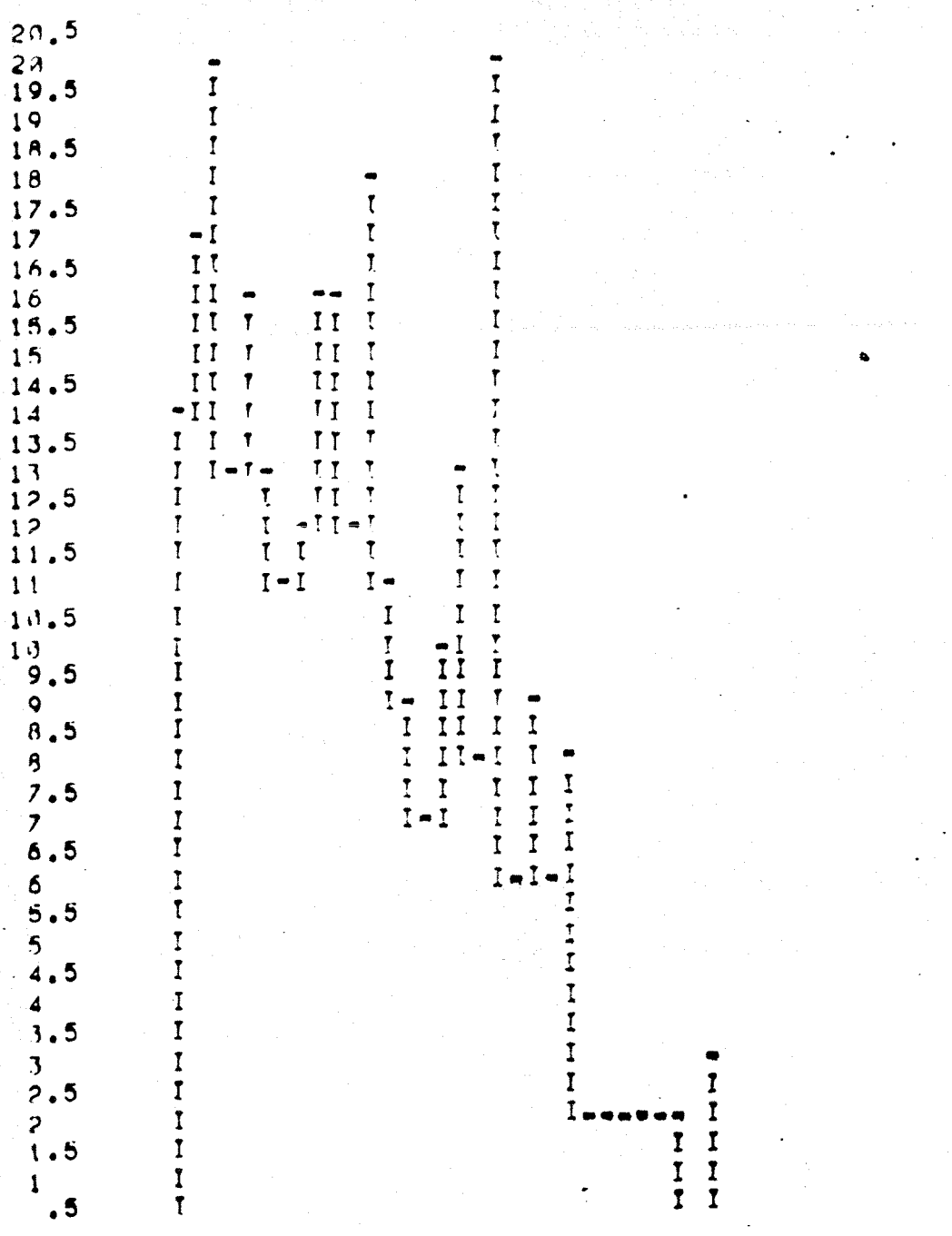


```
CHANNELS  10   0         1         2         3         4
           1   123456789012345678901234567890123456789012345678901234567890123

CONTENTS  10   1121111111111  11 2
           1.  47036312662819703806968222222 3

LOW EDGE  10             1111111122222222333333334444444445
           1.   123467890234568901245078012346789023456890
           0   0246802468024680246802468024680246802468024
```

* ENTRIES = 3.00 * ALL CHANNELS = .3000E+03
* BIN WID = .1200E+01 * MEAN VALUE = .1323E+02 cm
* SKEWNESS= .1136E+02 * KURTOSIS = .1766E+03

Fig.2.Distance traversed in target hydrogen,left arm.(cm)

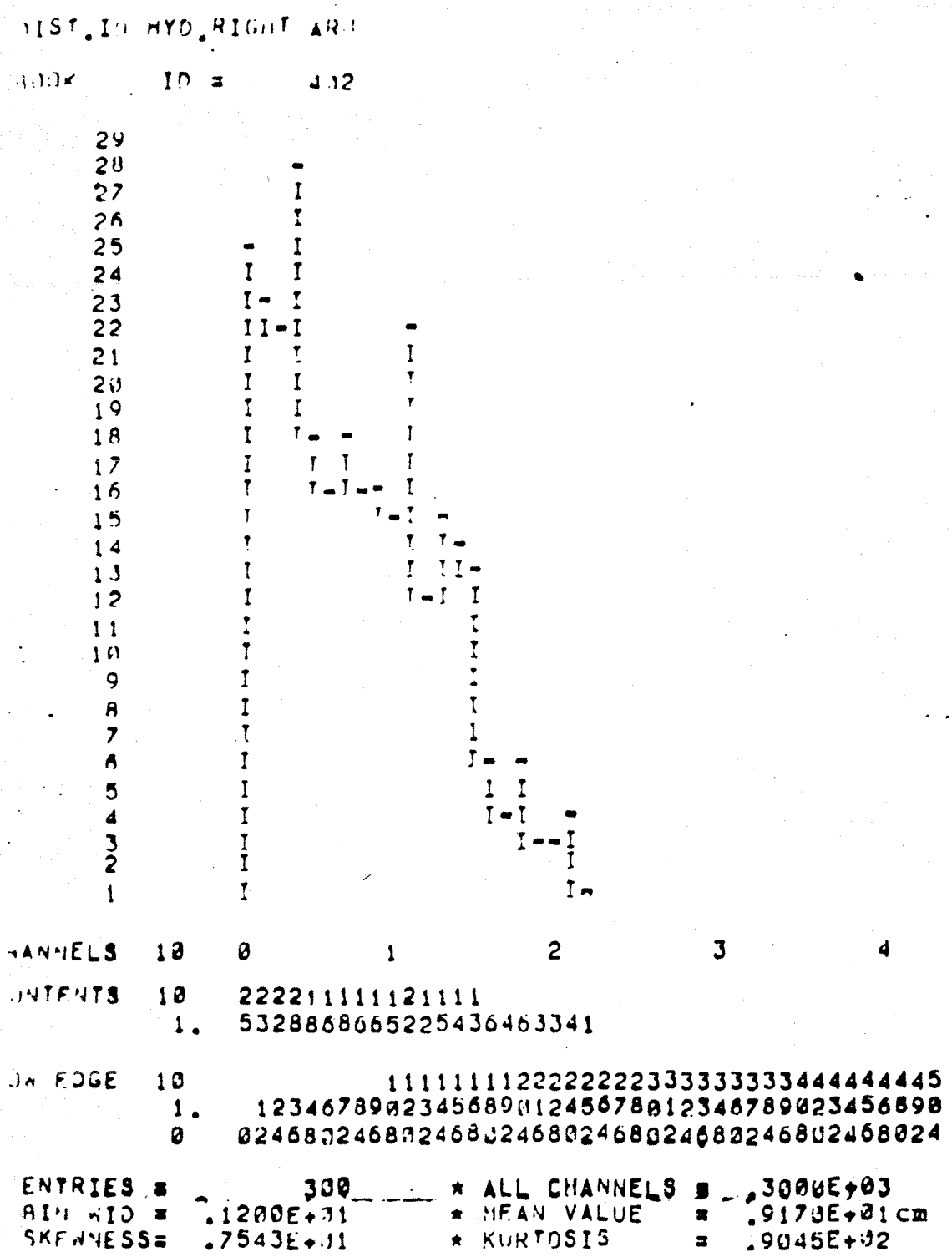

Fig.3.Distance traversed in target hydrogen,right arm.(cm)

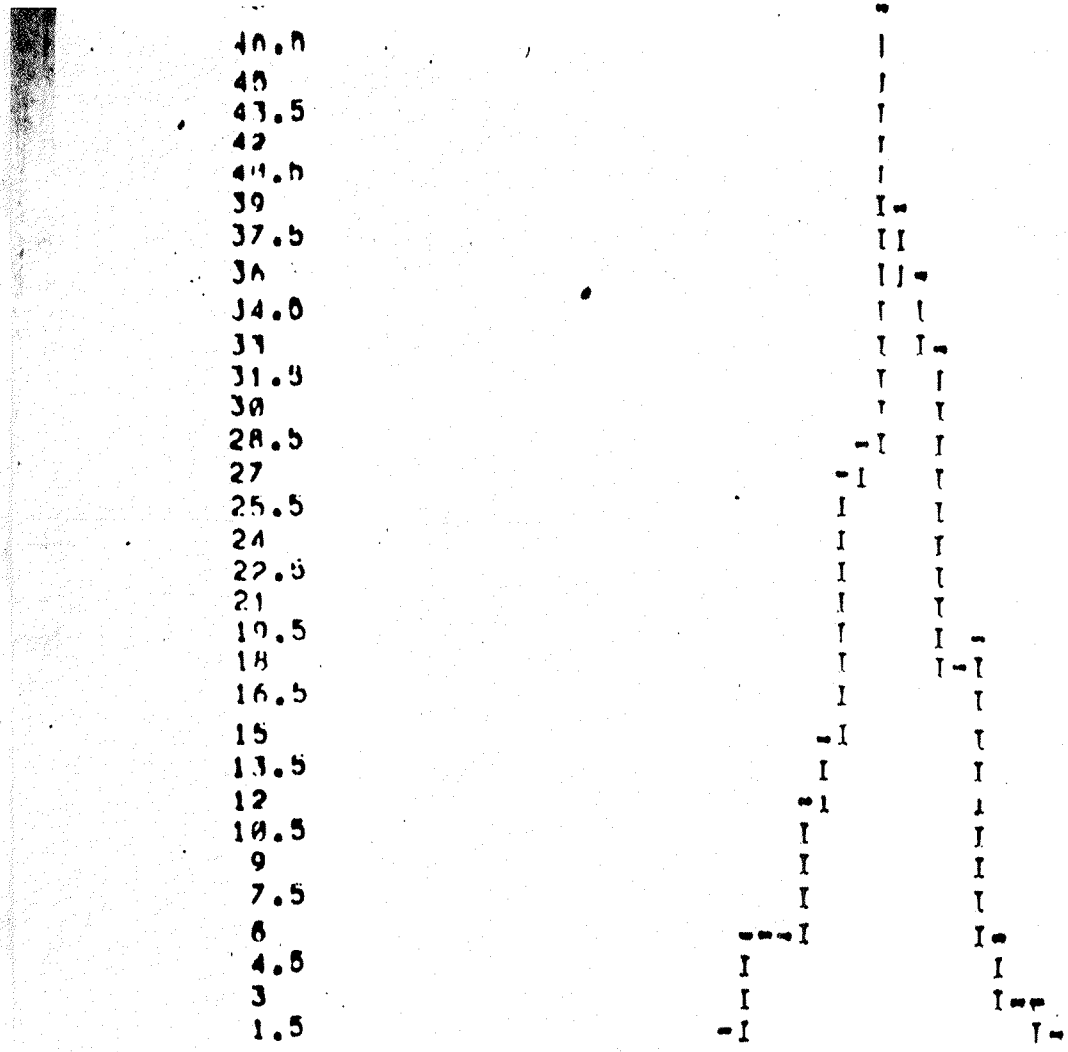

Fig.4.
Δ x-distribution in CH5 (cm)

```
CHANNELS  10    0         1         2         3         4         5
           1    12345678901234567890123456789012345678901234567890

CONTENTS  10                        1122433311
           1.                  1566157879627962 21

LOW EDGE        ----------------------
           1.   433333322222211111                 11111122222233333
           0    08653208754209764219864310134689124679024578023568
      - ---0  -0482604826048260482604826062840628406284062840628406284

* ENTRIES =         300      * ALL CHANNELS =  .3000E+03     * UNDERFLOW = 0.              * OVERFLOW = 0.
* BIN WID =  .1000E+00      * MEAN VALUE   =  .6048E-02     * R . M . S =  .4823E+00 cm   * ABNOR CHA= 0.
```

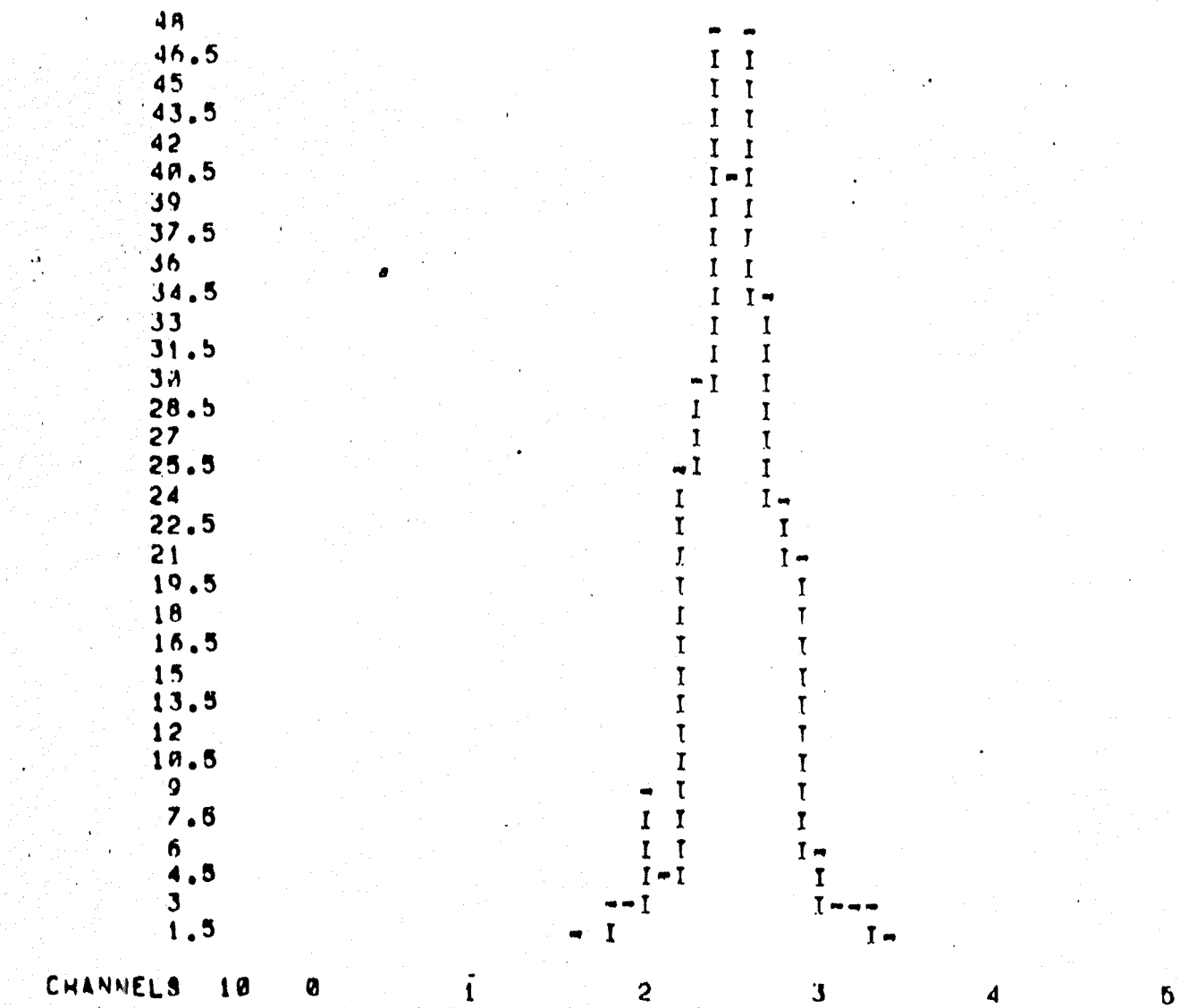


```
CHANNELS  10    0         1         2         3         4         5
           1    123456789012345678901234567890123456789012345678900

CONTENTS  10                        23444322
          1.                  1 22945070743163321

LOW EDGE        ------------------------
          1.    43333332222221111111                  11111122222233333
          0     00653208754209764219864310134689124679024570023568
          0     04826048260482604826048260628406284062840628406284

* ENTRIES =        300      * ALL CHANNELS =  .1000E+03      * UNDERFLOW = 1.          * OVERFLOW
* BIN WID =  .1600E+00      * MEAN VALUE   =  .3411E-01      * R  M  S =  .4332E+00 CM  * ABOVE CHA
```

Fig.5.
Δx-distribution in CH6 (cm).

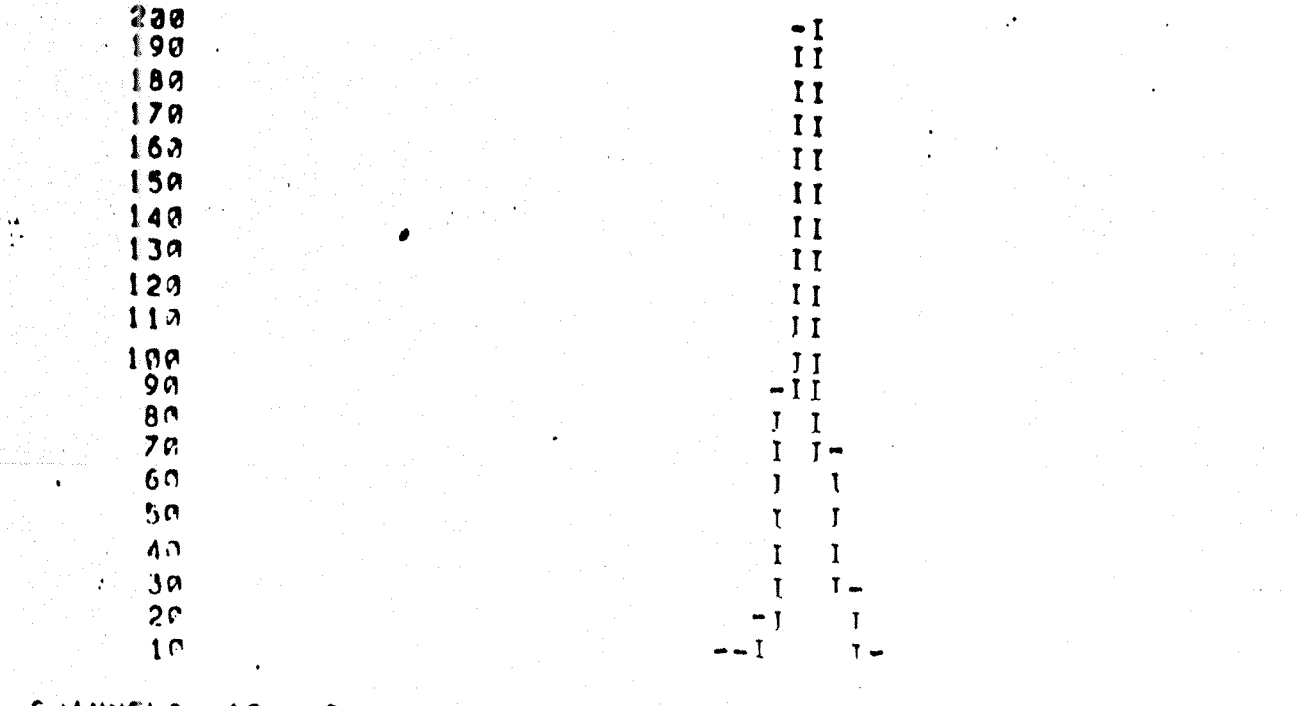

```
CHANNELS  10    0         1         2         3         4         5
           1    123456789012345678901234567890123456789012345678900

CONTENTS 100                          12
          10                        189062
           1.                     235851826

LOW EDGE        --------------------------
           1.   43333332222221111111                  11111122222233333
           0    08653208754209764219864310134689124679024578023568
           0    04826048260482604826048260628406284062840628406284
```

```
* ENTRIES =        600      * ALL CHANNELS =   .6000E+03      * UNDERFLOW = 0.                * OVERFLOW =
* BIN WID =  .1000E+00      * MEAN VALUE   =  -.4571E-02      * R . M . S =   .1816E+00 cm   * ABNOR CHA=
* SKEWNESS=  .4037E-03      * KURTOSIS     =  -.2871E+01
```

Fig.6. Δx-distribution in reference plane at z=400 cm. (cm)

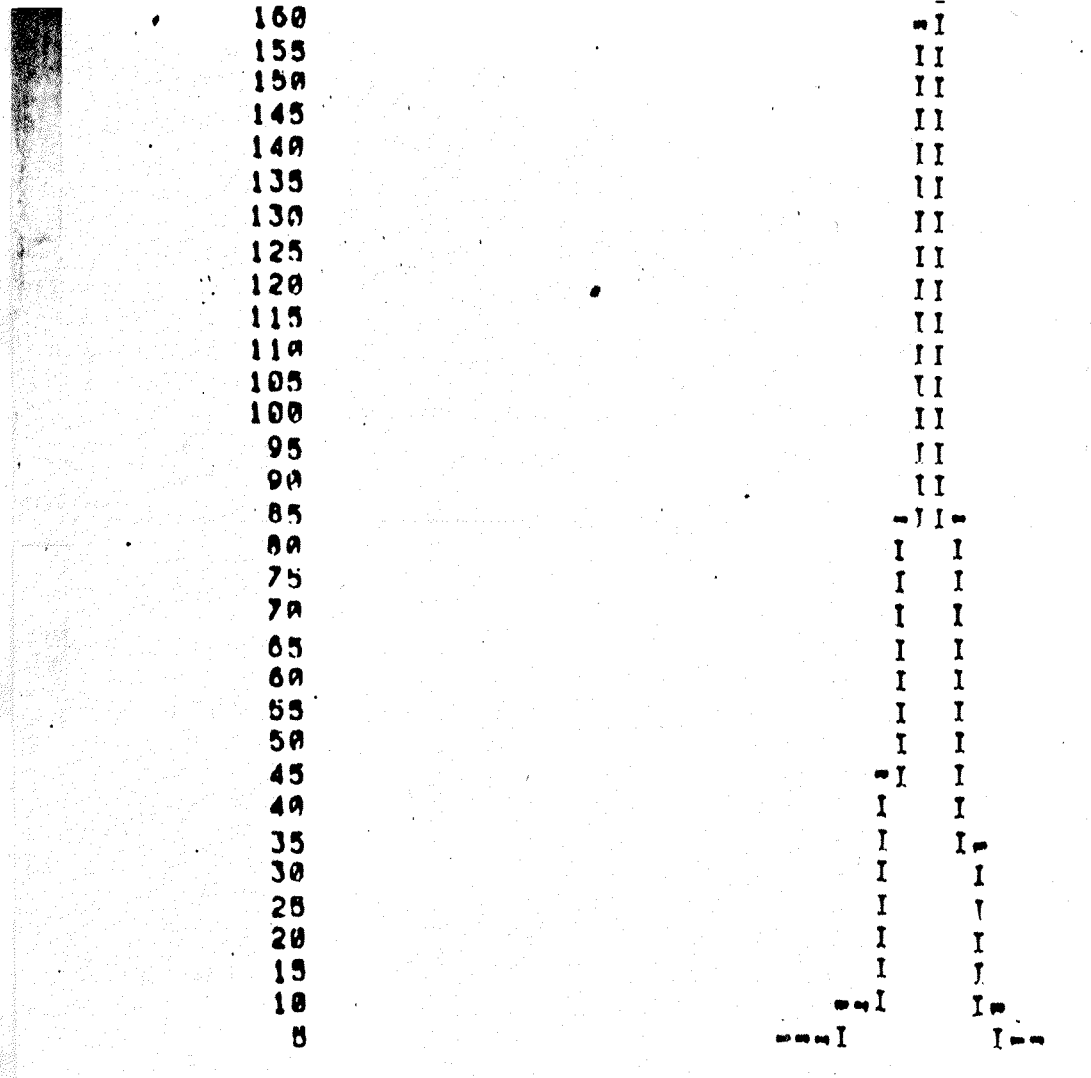

```
     160                               -I
     155                               II
     150                               II
     145                               II
     140                               II
     135                               II
     130                               II
     125                               II
     120                               II
     115                               II
     110                               II
     105                               II
     100                               II
      95                               II
      90                               II
      85                              -II-
      80                              I  I
      75                              I  I
      70                              I  I
      65                              I  I
      60                              I  I
      55                              I  I
      50                              I  I
      45                             -I  I
      40                             I   I
      35                             I   I-
      30                             I    I
      25                             I    I
      20                             I    I
      15                             I    I
      10                           --I    I-
       5                        ---I       I--

CHANNELS  10   0        1         2         3         4         5
           1   12345678901234567890123456789012345678901234567890

CONTENTS 100                           11
          10                         485783
           1.                   11186139213743

LOW EDGE       -------------------------
*10**  3   1.  09988877666554443322211     1122233444556667788899
           0   06284062840628406284062840482604826048260482604826

* ENTRIES =          600       * ALL CHANNELS =  .6000E+03      * UNDERFLOW =  0.               * OVERFLOW =
* BIN WID =  .4000E-03         * MEAN VALUE   = -.2150E-04      * R . M . S =   .6239E-03       * ABNOR CHA=
```

Fig.7.
Δ dx/dz-distribution in referenc
plane at z=400 cm.

LIST OF REFERENCES

[1] H. Högaasen, Lectures on theoretical elementary particle physics given at the University of Oslo (unpublished).

[2] J.J.J. Kokkedee, The Quark Model, W.A. Benjamin inc. publishers, New York (1969).

[3] M. Gell-Mann Phys. Lett. 8, 3 (1964) 214.

[4] G. Zweig CERN TH 401, 412 (1964).

[5] H. Harari, Summer student lectures, CERN (1976; unpublished).

[6] PLUTO Collaboration DESY Preprint, DESY 78/21 (1978).

[7] R. Mohapatra et al. Phys. Rev. D13, 6 (1976) 1733.

[8] D.H. Perkins, Introduction to high energy physics, Addison-Wesley (1972).

[9] W.R. Frazer, Elementary particles, p. 128, 129, Prentice - Hall Inc., New Jersey (1966).

[10] M.L. Perl, High Energy Hadron Physics, chapter 19,20, John Wiley & Sons, Inc. (1974).

[11] F.J. Gilman Phys. Rep. 4C, 3 (1972).

[12] J.I. Friedman & H.W. Kendall Ann. Rev. of Nucl. Sci. 22 (1972).

[13] G. Miller et al. Phys. Rev. D5, 3 (1972) 528.

[14] F.E. Close Proceedings of the 1976 CERN School of Physics CERN 76-20 (1976).

[15] J. Steinberger Proceedings of the 1976 CERN of Physics CERN 76-20 (1976).

[16] M. Gourdin Proceedings of the 1972 CERN School of Physics CERN 72-17 (1972).

[17] J.D. Bjorken & E.A. Paschos Phys. Rev. 185, 5 (1969) 1975.

[18] H. Deden et al. Nucl. Phys. B85 (1975) 269.

[19] O. Nachtmann
Max-Planck-Institut Preprint, MPI-PAE/PTh 50/78 (1978).

[20] A.W. Hendry & D.B. Lichtenberg
Rep. on Progr. in Phys. 41, 11 (1978).

[21] D. Sivers, S. Brodsky, R. Blankenbecler
Phys. Rep. 23C, 1 (1976).

[22] M. Banner et al.
Phys. Lett. 41B, 4 (1972) 547.

[23] S. Brodsky & G. Farrar
Phys. Rev. D11, 5 (1975) 1309.

[24] J.F. Gunion
University of California Preprint.
D. Jones & J.F. Gunion
SLAC Preprint SLAC-PUB-2157 (1978).

[25] A. Angelis et al.
Phys. Lett. 79B (1978) 505.

[26] J.F. Gunion, S. Brodsky, R. Blankenbecler
Phys. Rev. D8 (1973) 287.

[27] R. Blankenbecler, S. Brodsky, J.F. Gunion
SLAC Preprint SLAC-PUB-2057 (1977).

[28] R.D.Field & R.P.Feynman
Phys. Rev. D15, 9 (1977) 2590.

[29] R.P. Feynmann, R.D. Field, G.C. Fox
Nucl. Phys. B128, 1 (1977).

[30] R.D. Field
Phys. Rev. Lett. 40, 15 (1978) 997.

[31] E. Fischbach & G.W. Look
Phys. Rev. D15, 9 (1977) 2576.

[32] R. Cutler & D. Sivers
Phys. Rev. D16, 3 (1977) 679.

[33] G.C. Fox
Caltech Preprint CALT-68-643 (1978).

[34] G. Giacomelli
Phys. Rep. 23C, 2 (1976).

[35] A. Berglund et al.
CERN Preprint, 25 November 1978.

[36] C. Baglin et al.
Nucl. Phys. B98 (1975) 365.

[37] A. de Bellefon et al.
Paper submitted to the XIX International Conference on
High Energy Physics, Tokyo, August 1978.

[38] B. Schrempp & F. Schrempp
Phys. Lett. 55B (1975) 303.

[39] K.A. Jenkins et al.
Argonne National Laboratory Preprint ANL-HEP-PR-77-83 (1977).

[40] S.Brodsky & G. Farrar
Phys. Rev. Lett. 31, 18 (1973) 1153 .

[41] D.D. Coon et al.
SLAC Preprint SLAC-PUB-1483 (1974).

[42] A. Lundby
Invited paper at the Fifth International Conference on High-Energy Collisions, Stony Brook, NY, USA, 23-24 August 1973
CERN, 28 September 1973.

[43] P.J. Carlson & E. Johansson
Paper presented at the 3rd European Symposium on Antinucleon-Nucleon Interactions, Stockholm July 9-13, 1976.
University of Stockholm Preprint, June 1976.

[44] R.P. Feynman, R.C. Field, G. Fox
Phys. Rev. D18, 9 (1978) 3320.

[45] T. Buran et al.
CERN/SPSC 74-28 (1974).

[46] CERN SPS Experimenters' Handbook 1978 (1978).

[47] J.V. Allaby & C. Bovet
CERN/Lab. II/EA/74-5 (1974).

[48] M. Yvert
ELAS 100, WA7 Internal Report (1977).

[49] M. Yvert, Performance of H1b at -20 GeV,
WA7 Internal Note (31.08.78).

[50] D. Imrie
ELAS 111, WA7 Internal Report (1978).

[51] M. Yvert, Some corrections to get the cross section at -20 GeV,
WA7 Internal Note (04.01.79).

[52] P.J. Carlson
ELAS 97, WA7 Internal Report (1977).

[53] K.E. Johansson
WA7 Internal Note (02.01.78).

[54] F.F. Heyman
ELAS 44, WA7 Internal Report (1975).

[55] M. Poulet & A. Santroni
LAPP Preprint, LAPP 77-02 (1977).

[56] J. Joosten et al.
ELAS 79, WA7 Internal Report (1976).

[57] B. Bracher et al.
ELAS 105, WA7 Internal Report (1977).

[58] E. Johansson
ELAS 123, WA7 Internal Report (1979).

[59] H. Klein & J. Zoll, PATCHY Reference Manual
CERN (1977).

[60] CERN PROGRAM LIBRARY Write-up (1978).

[61] SUMX USER'S MANUAL (1973).

[62] R. Böck & J. Myrheim
ELAS 95, WA7 Internal Report (1976).

[63] F. Verkerk & T.R. Willits
ELAS 93, WA7 Internal Report (1979)

[64] S. Sharrock
ELAS 57, WA7 Internal Report (1975).

[65] R. Böck et al.
ELAS 115, WA7 Internal Report (1978).

[66] B. Schistad
Thesis, University of Oslo (1978).

[67] H. Wind
Nucl. Instr. & Meth. 115 (1974) 431.

[68] R. Böck
ELAS 77, WA7 Internal Report (1976) with Addendum (1978).

[69] J. Myrheim & L. Bugge
Nucl. Instr. & Meth. 160 (1979) 43.

[70] B. Rossi, High Energy Particles,
Prentice-Hall, Inc. New York (1952), chapter 2.

[71] Review of Particle Properties
Rev. of Mod. Phys., 48, 2 (April 1976).

[72] R. Barate et al.
CERN/SPSC/76-3 (1976).

[73] D.P. Owen et al.
Phys. Rev. 181 (1969) 1794.

ERRATUM

HIGH ENERGY HADRONIC REACTIONS AT LARGE TRANSVERSE MOMENTA AND THE CERN SPS EXPERIMENT WA7
Lars Bugge,Thesis,University of Oslo,1979.

The subdivision of p.139 starting with "In order to establish..." and ending with "$\cos\theta_{CM}$=0.55." should be replaced by:

"In order to establish the energy dependence of the cross sections, they are integrated over a range of t to reduce the uncertainty. According to the dimensional counting rules (see section 3.3.2),the fixed angle meson-proton elastic cross sections have the structure

$$\frac{d\sigma}{dt} = s^{-8} f(\cos\theta_{CM})$$

The integration gives

$$\int_{t_1}^{t_2} \frac{d\sigma}{dt} dt = s^{-8} \int_{\cos\theta_1}^{\cos\theta_2} f(\cos\theta_{CM}) 2p_{CM}^2 d(\cos\theta_{CM}) = s^{-7} G(\theta_1,\theta_2),$$

where G is a constant given by the limits of integration.
I.e. the integrated cross sections should show an s^{-7} dependence, provided the region of integration is contained in the wide angle area where dimensional counting is supposed to work.We have chosen a region of integration from $\cos\theta_{CM}$=0.20 to $\cos\theta_{CM}$=0.55."

The subdivision starting at the bottom of page 139 with "Assuming an s^{-n}..." and ending on top of page 142 with "...is not." should be substituted by:
"Assuming an s^{-n} energy dependence of the integrated cross sections, we arrive at n=7.0±0.6 for π^+ and n=8.0±0.7 for π^-.The π^+result is clearly consistent with the dimensional counting rule prediction of s^{-7},whereas the π^- result shows a 1.5 standard deviations discrepancy.